FEMTOSECOND TIME-RESOLVED SPECTROSCOPY STUDY OF EXCITED STATE DYNAMICS: HETEROCYCLIC RINGS AND HETEROCYCLIC DERIVATIVES

by

HUI YU

(Under the Direction of Susanne Ullrich)

ABSTRACT

The ultraviolet photoresistance in biomolecules have been researched extensively in recent years. A bottom-up approach has been applied and the molecular dynamics of heterocyclic rings have raised interest. The presented work here investigates the UV excited state dynamics of five-membered heterocyclic rings – imidazole, pyrazole and pyrrole, which are commonly seen as subunits in larger biomolecules. Two nucleo bases that are heterocyclic pyrimidine derivatives – uracil and thymine, which are researched less extensively than adenine, are also studied in this work. Time-resolved spectroscopic techniques are applied, including time-resolved photoelectron spectroscopy, time-resolved total kinetic energy release and time-resolved ion yield, all of which are with femtosecond timing resolution which help understanding the ultrafast photoprotection mechanisms. This work can also extend to medical physics such as laser treatment of diseases in the future, as the heterocyclic molecules investigated here are subunits of various corresponding biomolecules.

INDEX WORDS: Femtosecond, Time-resolved, Excited state, Heterocycles, DNA bases

FEMTOSECOND TIME-RESOLVED SPECTROSCOPY STUDY OF EXCITED STATE DYNAMICS: HETEROCYCLIC RINGS AND HETEROCYCLIC DERIVATIVES

by

HUI YU

BA, Nanjing University, China, 2008

A Dissertation Submitted to the Graduate Faculty of The University of Georgia in Partial Fulfillment of the Requirements for the Degree

DOCTOR OF PHYLOSOPHY

ATHENS, GEORGIA

2015

FEMTOSECOND TIME-RESOLVED SPECTROSCOPY STUDY OF EXCITED STATE DYNAMICS: HETEROCYCLIC RINGS AND HETEROCYCLIC DERIVATIVES

by

HUI YU

Major Professor:	Susanne Ullrich
Committee:	Williams Dennis
	Heinz-Bernd Schuttler

Electronic Version Approved:

Suzanne Barbour
Dean of the Graduate School
The University of Georgia
August 2015

ACKNOWLEDGEMENTS

First and Foremost, my gratitude goes to my advisor Dr Susanne Ullrich, whose patient instruction and constant encouragement is priceless in my PhD studies. I would also like to thank a senior member in our group, Dr Nicholas L. Evans, for teaching me experimental techniques and helping me understand theoretical knowledge together with Dr Ullrich. I would also like to express my gratitude to other group members, Mr Timothy J. Godfrey and Mr Michael S. Biddle, for their help in daily experimental operations, and William M. Porter, for his instruction on the experimental ideas of the lab.

My thanks also go to Dr Vasilios G. Stavros and his group members Dr David J. Hadden and Dr Craig A. Williams, for their instruction and help during my two-week exchange in the UK. I would also like to thank Dr Mario Barbatti and Dr Igor Pugliesi, for their valuable discussion and theoretical models to analyze our experimental results. I also thank Mr Bob Letiecq from Coherent Inc., for servicing and showing me how to tune our laser apparatus, and Mr Lewis Fortner and other co-workers at the UGA instrument shop, for their help with design, construction and maintenance of our vacuum system.

I would also like to express my gratitude to my parents, who supported and encouraged my PhD study. I would also like to thank Dr William Dennis, Dr M. Howard Lee and Dr Steven P. Lewis, for teaching me graduate level classes. I also thank my departmental colleagues Dr Luning Wang, Dr Joonsang Lee and Mr Yizhuo He, my roommates and other friends, and the dinning commons at the University of Georgia, for their help in my daily life.

LIST OF ABBREVIATIONS

2D – two dimensional

BE – Binding Energy

CI – Conical Intersection

CW- Continuous Wave

DNA – Deoxyribonucleic Acid

FHG – Fourth Harmonic Generation

FWHM – Full Width at Half Maximum

IC – Internal Conversion

IP – Ionization Potential

IRF – Instrument Response Function

ISC – Intersystem Crossing

IVR – Intromolecular Vibrational Energy Redistribution

OPA – Optical Parametric Amplification

REMPI – Resonance Enhanced Multiphoton Ionization

SFG – Sum Frequency Generation

SHG – Second Harmonic Generation

TOF – Time of Flight

TRIY – Time-Resolved Ion Yield

TRPES – Time-Resolved Photoelectron Spectroscopy

TR-TKER – Time-Resolved Total Kinetic Energy Release

UV – ultraviolet

TABLE OF CONTENTS

Page

LIST OF TABLES

Page

LIST OF FIGURES

Page

CHAPTER 1

INTRODUCTION AND LITERATURE REVIEW

1.1 Motivation

1.1.1 UV absorption

Light can be absorbed in the form of photon energies, to promote a molecule from state E_1 to state E_2, fulfilling the relation

$$h\nu = E_2 - E_1$$

[1 – Klessinger] where ν is the frequency of the light being absorbed, whose wavelength is given by

$$\lambda = \frac{c}{\nu}$$

where c is the speed of light. A photon can be absorbed only if its energy corresponds to, or higher than, the energy difference between the two stationary electronic states E_2 and E_1.

Most biomolecules undergo a sharp increase in absorbance when wavelengths decrease from vis to the UV region. (Plotted in Fig. 1.1 is the absorption spectrum of imidazole in the UV-vis region, which is a typical case of heterocyclic molecules. [2 – Barbatti] Therefore excited state dynamics of these molecules can be investigated after being excited by a UV pump pulse.

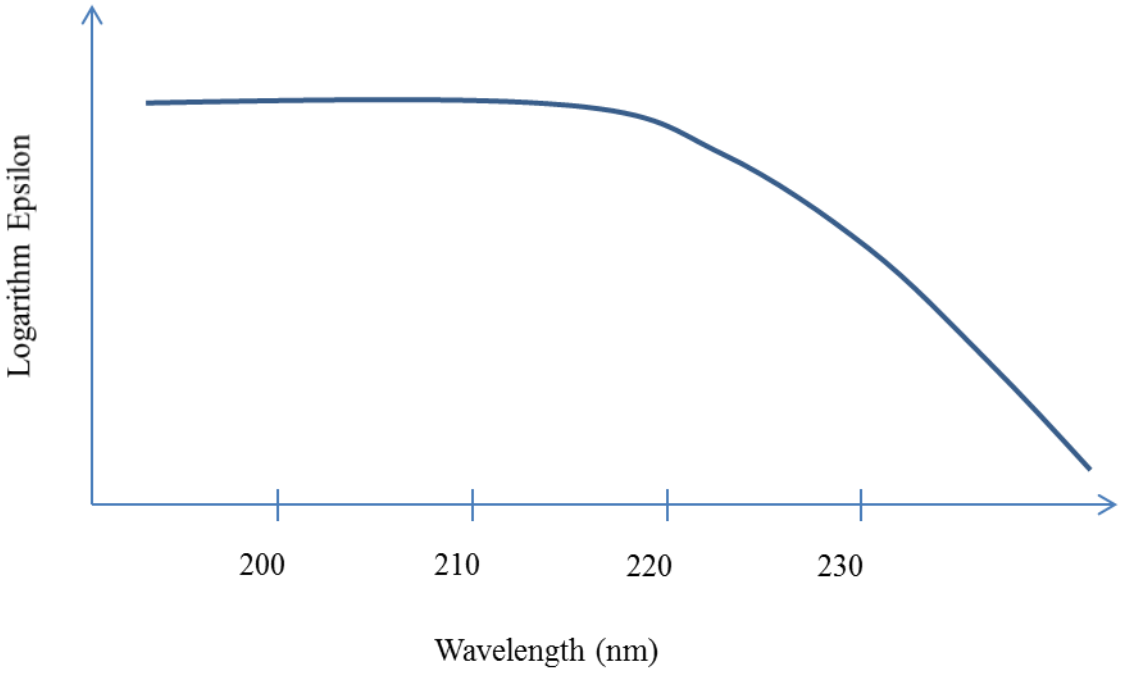

Figure 1.1 UV absorption spectrum of imidazole.

1.1.2 Photostability

Biomolecules and chemicals that are exposed to UV radiation may absorb photon energies and be excited due to high absorption in the UV/vis wavelength region. To convert dangerous electronic excitation energy to less-dangerous vibration energy, photoprotection mechanism has been introduced, in this case excited state biomolecules, especially DNA bases, will relax to the ground state and deactivate on ultrafast timescales, usually at fs to ps level. . [3 – 5 – Crespo-Hernandez, Bisgaard, Evans] Therefore, investigation on the excited state dynamics of certain biomolecules and their subunits, and studies on how small changes to the electronic structure affect the shape of the potential energy surfaces, are important in understanding photostability.

1.1.3 Heterocyclic rings and heterocyclic derivatives – DNA bases

The molecules investigated in this thesis are all carbon-nitrogen heterocyclic molecules. Imidazole, pyrazole and pyrrole are 5-membered heterocyclic rings, and are major subunits in various large biomolecules, including adenine, histidine, tryptophan, porphyrin and chlorophyll; whereas uracil and thymine are DNA bases that are derivatives of 6-membered pyrimidine. (Fig. 1.2)

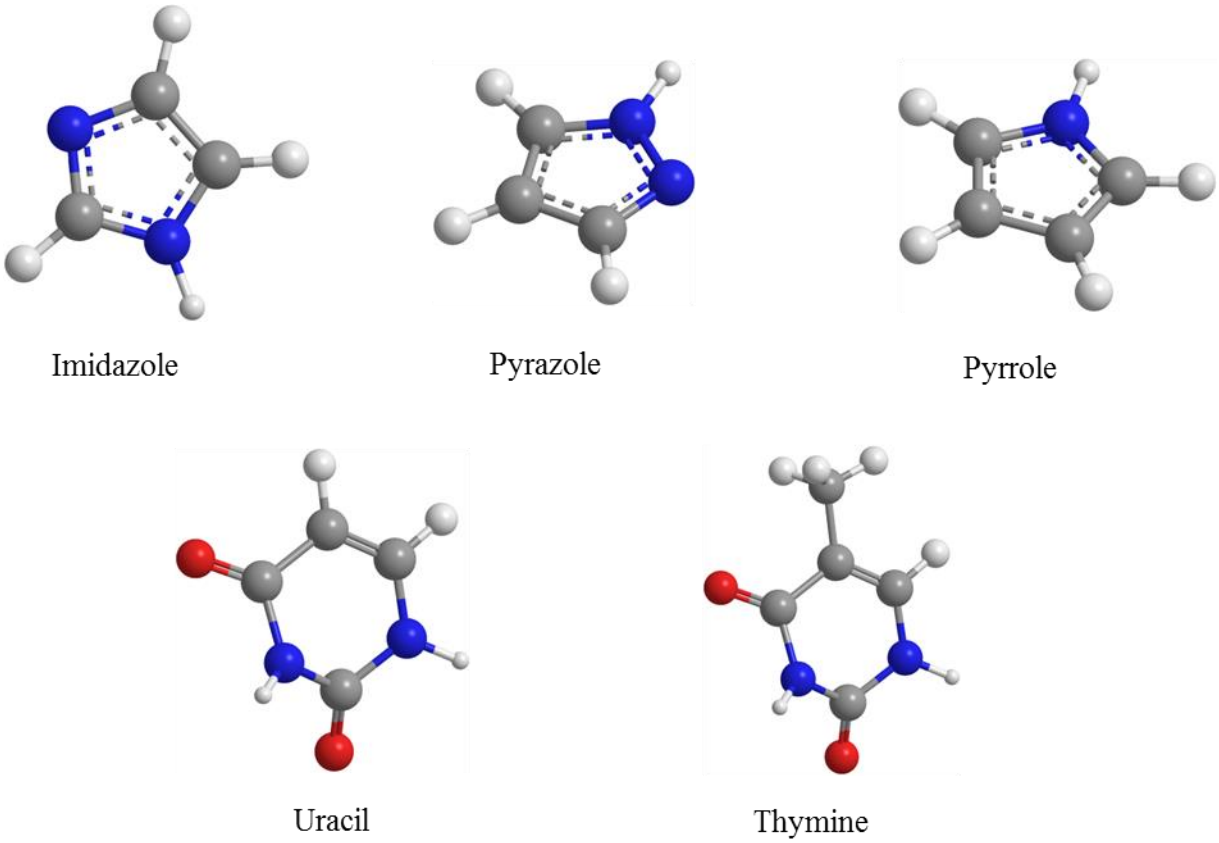

Figure 1.2 Molecular structure of imidazole, pyrazole, pyrrole, uracil and thymine. Carbon, nitrogen, oxygen and hydrogen atoms are indicated as gray, blue, red and smaller white balls, respectively.

1.2 Excited states

Excited states lie higher in energy than molecular ground state, the type of which are defined by the electron orbitals involved in the electronic transitions in organic compounds. For instance, promotion of an electron from a π-bonding orbital to an antibonding σ* orbital is defined as a $\pi - \sigma^*$ transition, and the molecule is denoted as being excited to a $\pi\sigma^*$ state, [6 – Telle] as indicated in Fig. 1.3.

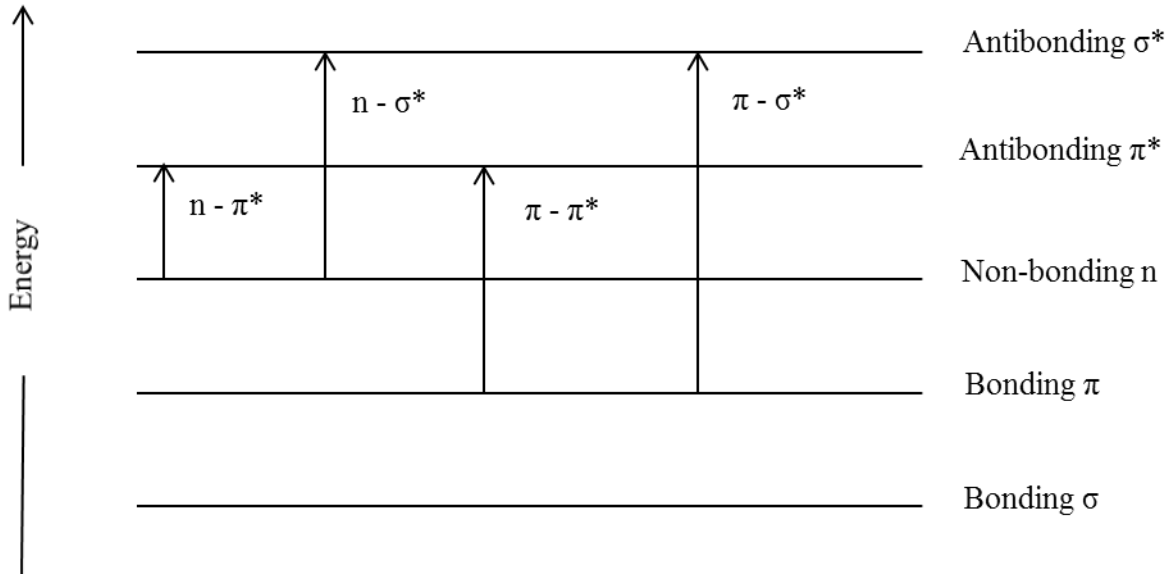

Figure 1.3 List of possible electronic transitions in heterocyclic molecules.

Depending on whether electron spins are still paired after excitation, singlet excited state and triplet excited state are differentiated, the latter of which requires an additional "forbidden" spin transition, thus less probable to be excited after absorption of a photon, and singlet states are the

focus of this work. Electronically excited states are less stable and will relax to states with lower energy levels, either by emitting photons or non-radiatively through Conical Intersections (CI) (section 1.3.3). All types of electronic transitions that are studied in this thesis, together with fluorescence and phosphorescence transitions, are listed in the Jablonski diagram (Fig. 1.4) [7 – Jablonski], which will be further discussed in the following sections.

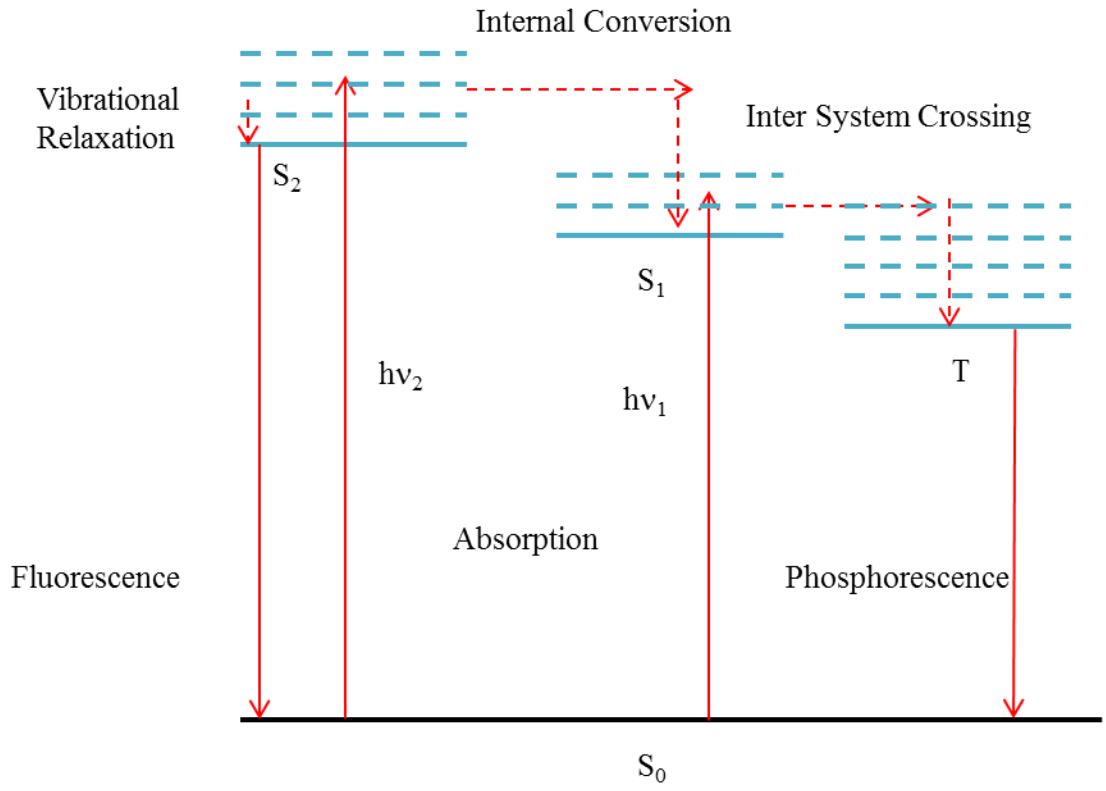

Figure 1.4 A schematic draw of the Jablonski diagram. Radiative transitions are indicated in solid arrows, and non-radiative transitions are indicated in dashed arrows.

1.2.1 Radiative transitions

Radiative transitions include absorption and emission of energies. When a ground state molecule absorbs photon energies that are higher than excitation energy, the energetically excited states can be populated. In contrast, excited state molecules can emit photons to go back to the ground state, through fluorescence or phosphorescence transitions. (Fig. 1.4) As indicated in the equation below,

$$h\nu = E_2 - E_1$$

in which E_1 is the ground state potential and E_2 is the excited state potential, and ν is the frequency of the photon absorbed or emitted, with wavelength

$$\lambda = \frac{c}{\nu}$$

Fluorescence transition is the population transfer from a singlet excited state to the ground state, with energy conserved by emission of a photon with corresponding frequency; the spin multiplicity remains the same. [8 – Stokes] Phosphorescence transition is a similar process in which population transfers from two electronic states with different spin multiplicity, typically from a triplet excited state to the ground state. The timescale of fluorescence and phosphorescence transitions typically range from 10^{-12} to 10^{-6} s and 10^{-6} to 10^{-1} s in organic compounds, respectively, [9 – Atkins] and the photon emitted is usually red-shifted from the photon absorbed due to energy loss through internal conversion (IC) and intro-molecular vibrational energy redistribution (IVR) processes. [10 – Kinsey]

1.2.2 Franck-Condon principle

After absorption or emission of a photon, vibronic energy levels may change simultaneously with electronic energy levels. The Franck-Condon principle is used to explain explaining the intensity of vibronic transitions, which states that a change in vibronic energy level during an electronic transition is more likely to happen if the two vibrational wave functions overlap more significantly. [11 – Franck] The resulting state is the Franck-Condon state and the transition involved is "vertical" along the nuclear coordinate. (Fig. 1.5)

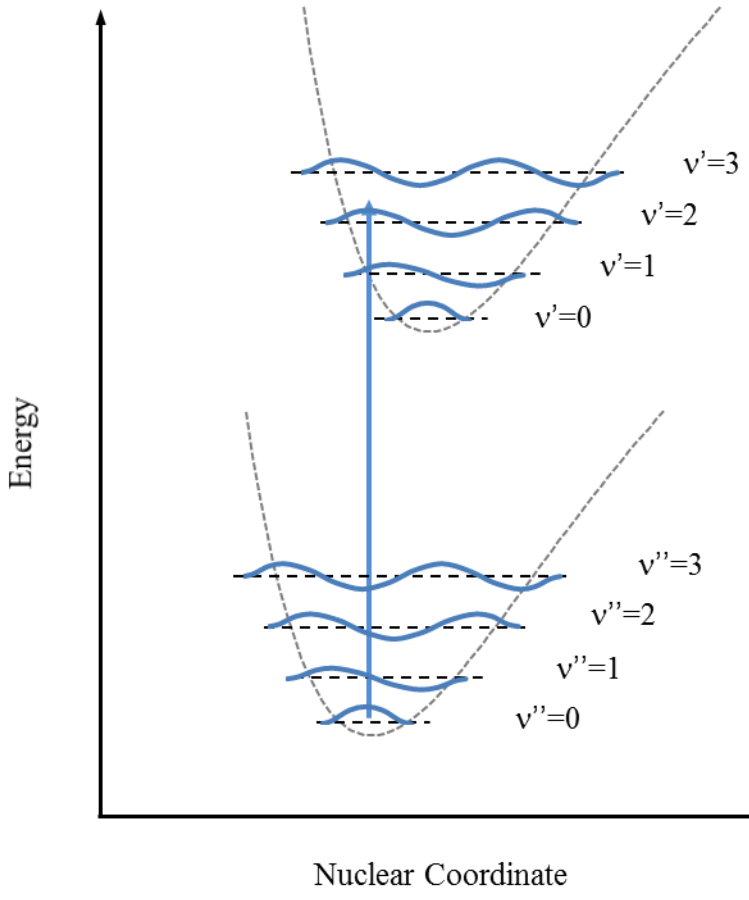

Figure 1.5 Franck-Condon principle diagram, with "vertical" excitation shown by the arrow.

After absorption of a photon from the zeroth vibrational level of the electronic ground state, the corresponding Franck-Condon state is vibronically excited. The relaxation from higher vibrational states to the lowest vibrational state, or IVR, happens immediately after excitation, where vibrational energy is redistributed to other vibrational degrees of freedom. [12 – Boyall]

1.2.3 Non-radiative transitions

Non-radiative transitions, or radiationless decay, include internal conversion (IC) [13 – Loveland] and intersystem crossing (ISC), both of which are not associated with absorption or emission of photons. [14 – Bixon] IC is the process of de-activation from a higher to a lower electronic state with spin state remaining the same, such as $S_2 - S_1$ and $T_2 - T_1$ transition, whereas the spin changes in ISC, for example $S_1 - T_1$ (Fig. 4). Time-scales of internal conversion are typically in the fs to ps range, [3 – Crespo-Hernandez, 15 – Barbatti, 16 – Barbatti, 17 – Middleton, 18 – Barbatti, 19 – Mai] which can be verified by the appearance times of photoproducts generated from different relaxation coordinates, and the decay dynamics in photoionization experiments.

1.3 Relaxation

1.3.1 Relaxation coordinates

Following UV excitation, heterocyclic molecules in their excited states will eventually relax to their ground state, along several possible coordinates, most notably (1) the bond dissociation coordinate, by which a bond between two adjacent atoms elongates and breaks apart into two photofragments; (2) the ring deformation coordinate for molecules with ring structure, by which the initially in-plane ring structure is deformed and out-of plane angle is increased when extra

energy from excitation is absorbed; and (3) the in-plane ring opening coordinate, by which the one of the C-N bond of the heterocyclic ring breaks and the a bi-radical chain is generated.

In cases of carbon nitrogen heterocyclic molecules, the easiest bond to break is the N-H bond, (Fig. 1.6) which has been verified through isotopic studies [20 – Cronin] and bond intensity thermochemistry studies. [21 – da Silva]

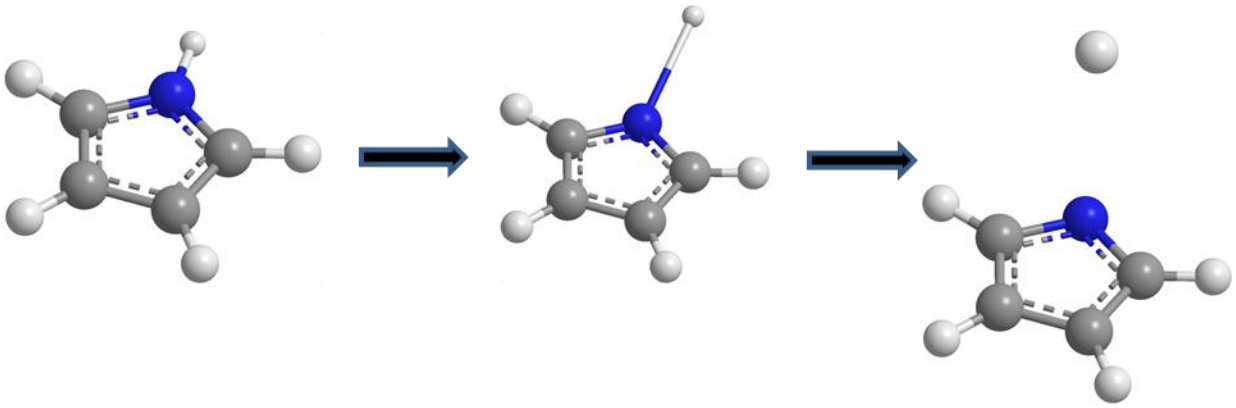

Figure 1.6 Schematic picture of an N-H dissociation process in pyrrole. The colors of the atoms are the same as introduced in Fig. 1.2.

The N-H bond is usually dissociated following excitation to the $\pi\sigma^*$ state, which at the same time is the lowest singlet excited state of imidazole and pyrrole investigated in this thesis. [22 – Ashfold, 23 – Ashfold] Thus the detection of H atoms coming off from excited state parent molecules provides timing and energetic information in understanding $\pi\sigma^*$ state dynamics. [20 – Cronin, 24 – Cronin, 25 – Hadden, 26 – Roberts]

On the other hand, in all molecules studied in this thesis, the ring deformation relaxation pathway can only start after excitation to $\pi\pi^*$ states, and is followed by ring-opening and bond breaking to form photofragments larger than the single atom(s) produced by bond dissociation

pathway. [15 – Barbatti, 16 – Barbatti, 18 – Barbatti, 19 – Mai, 27 – Vazdar, 28 – Ismail, 29 – Zhang, 30 – Nachtigallova, 31 – Hudock] Therefore ππ* state dynamics can be studied through reactions along this coordinate.

1.3.2 Conical Intersections

According to Born-Oppenheimer approximation, the motion of atomic nuclei and electrons in a molecule can be separated, [32 – Wu] and the wavefunction of a molecule can break into its electronic and nuclear components

$$\psi_{total} = \psi_{electronic} \times \psi_{nuclear}$$

In a system with 2 degrees of freedom, potential energy surface is widely used, with x and y axes assigned to atomic distances or bond angles, and z axis assigned to energy levels. By introducing the concept of potential energy surface, minimal or maximum energy point of a certain state can be located more precisely.

A CI of two potential energy surfaces lies where the two potential energy surfaces are degenerate (intersect) and the non-adiabatic couplings between these two states are non-vanishing. In the vicinity of conical intersections, the Born–Oppenheimer approximation breaks down, allowing non-adiabatic processes to take place. The location and characterization of conical intersections are therefore essential of the understanding to a wide range of reactions, such as photo-reactions, explosion and combustion reactions, etc. [1, 33 – Klessinger, Yarkony]

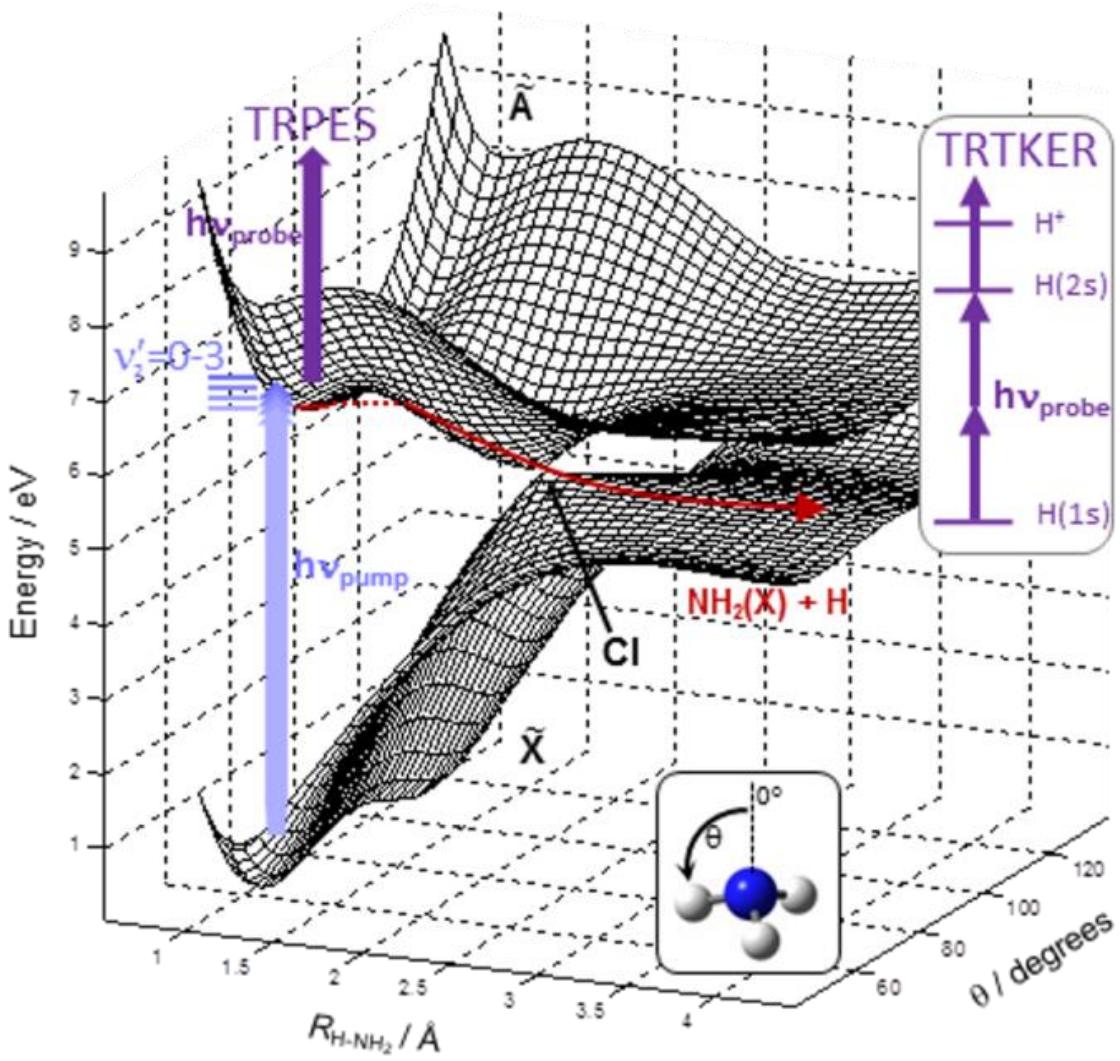

Figure 1.7 Schematic picture of potential energy surfaces and CI. $\tilde{X}$ stands for electronic ground state and $\tilde{A}$ stands for electronic excited state. The two potential energy surfaces intersect at a CI. [34 – Yu][1]

[1] H. Yu, N. L. Evans, A. S. Chatterley, G. M. Roberts, V. G. Stavros, and S. Ullrich, J. Phys. Chem. A, 2014, 118, 9438-9444.

Reprinted here with permission of the publisher.

When excited state molecules relax to CIs with the ground state, a portion of them undergoes photofragmentation process, as indicated in Fig. 1.7, while other molecules relax back to the ground state. As photoproducts are usually ionized rapidly in our pump-probe experiments, the time that certain photofragments are detected following initial excitation of the monomer is considered equal to the time to relax to the corresponding CI, or the lifetime of that certain excited state. Photoelectrons coming off during the ionization process are also direct measures of excited state lifetimes. Therefore monitoring the appearance times of all photoproducts and the lifetimes of photoelectrons give insight into all possible relaxation pathways and their lifetimes, following excitation at a specific wavelength.

1.4 Ionization

The minimum energy required to remove an electron from a neutral molecule is the adiabatic ionization potential (IP). It reflects the energy difference between the vibrational ground state of the neutral ground state and that of the ionic state. Vertical IP, on the other hand, is the energy required to ionize a molecule from its vibrational ground neutral state to a vibrational excited state of the ion that has the same geometry according to the Franck-Condon principle (section 1.2.2), and can be represented by a vertical line along the energy axis.

1.4.1 Resonance Enhanced Multiphoton Ionization (REMPI) of Hydrogen

A special case of ionization concerns the hydrogen atom. An excited intermediate state of hydrogen resonance can be accessed by two photons of 243.15 nm, and an additional photon at 243.15 nm follows to ionize the molecule. The selection rule states that molecular vibrational peaks will only be observed when the electric dipole is perpendicular to the surface, so that two

photons at 243.15 nm are needed to excite hydrogen atom to its 2s state before been ionized. Therefore in all our $\pi\sigma^*$ state dynamic studies with hydrogen elimination, the probe wavelengths are kept at 243.15 nm.

1.4.2 Pump-probe mechanism

To investigate the excited state dynamics of molecules, the pump-probe mechanism is introduced, in which a probe pulse is applied at a time delay to the pump pulse. Apart from the ion signals from the one-color only pulses from either the pump or the probe, two-color signals that are time-dependent are also recorded, and can be separated from one-color signals by subtracting them from the total signal. Excited state lifetimes can be measured by tracking the ion and electron intensities as a function of relaxation time. The appearance times of the photoproducts are also extracted after proceeding to the CI of excited state and ground state, providing another way of measuring lifetimes of the excited states.

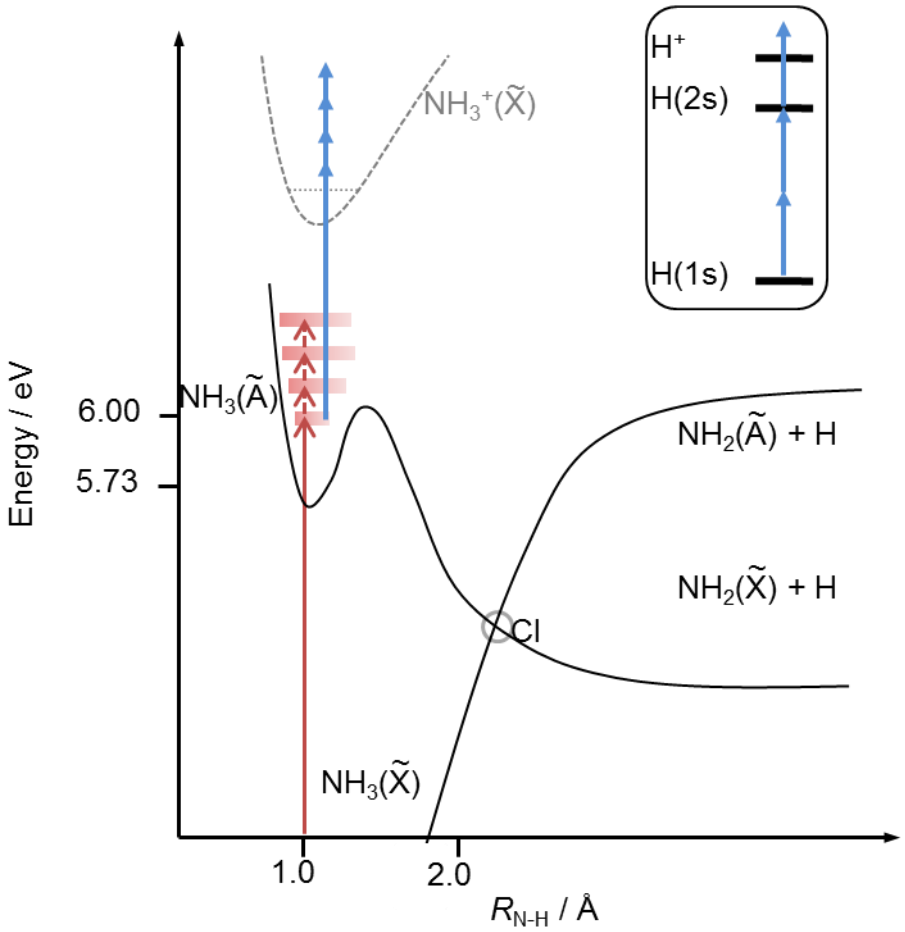

Figure 1.8 Pump-probe mechanism of NH_3 and the REMPI of hydrogen photoproduct. Red arrows are photons from the pump pulse, and the blue arrows are photons from the probe pulse. [35 – Evans][2]

Under most circumstances the relaxation dynamics of interest are in the pump-probe direction only (i.e. pump beam comes first and probe beam is delayed); thus, the detection in the reverse direction needs to be avoided. Therefore the wavelengths of the pump and probe beams are typically well separated to allow a significant difference in absorption of the ground state

[2] N. L. Evans, H. Yu, G. M. Roberts, V. G. Stavros, and S. Ullrich, Phys. Chem. Chem. Phys., 2012, 14, 10401. Reprinted here with permission of the publisher.

molecule. However, in some special cases such as hydrogen ion detection, the probe wavelength has to be fixed at 243.15 nm for REMPI, and if the pump wavelength is close to 240 nm and probe-pump signal cannot be avoided, reverse dynamics have to be considered when describing the signal.

1.4.3 Dissociative ionization

When the intensity of the pump pulse is high enough that two or more photons take part in the excitation, with excitation energy greater than the vertical IP of the molecule, the ionic state can be directly accessed. If the pump pulse can provide further energy to overcome the bond dissociation potential of the molecule in the ionic state, fragments will be generated. This process is 1-color multiphoton ionization, which is not time-dependent, and is typically subtracted from the total signal and does not interfere with the analysis of excited state dynamics. However, when the probe and pump pulse intersect within their pulse durations, one or more photons from the probe pulse may provide energy to overcome bond dissociation potential of the ionic state parent and generate fragments. This time-dependent process is the dissociative ionization, which coexists with excited state fragmentation and requires further separation in data analysis, which will be discussed in section 1.6.

1.5 Spectroscopic techniques

Time-Resolved Photoelectron Spectroscopy (TRPES), Time-Resolved Total Kinetic Energy Release (TR-TKER) and Time-Resolved Ion Yield (TRIY) have been employed to study the excited state dynamics of molecules of interest.

1.5.1 TRPES

In TRPES the excited state molecules are ionized by one or multi photons from the probe pulse, typically at UV wavelength, and an energy spectrum of the departing electrons can be detected. [36 – Newmark] From energy conservation, the ejection of a photoelectron from a molecule, due to irradiation by light of a specific wavelength, must lead to quantized electron energies corresponding to the energy states of the molecular ion. [37 – Muller-Dethlefts] He(I) PES was introduced by Turner and co-workers to investigate molecules [38, 39 – Aljoboury, Turner] by obtaining the valence orbitals of molecular species and vibronic states in the molecular ion, and Zero Kinetic Energy PES has been studied by MullerDethlefs and co-workers. [37 – Muller-Dethlefs]

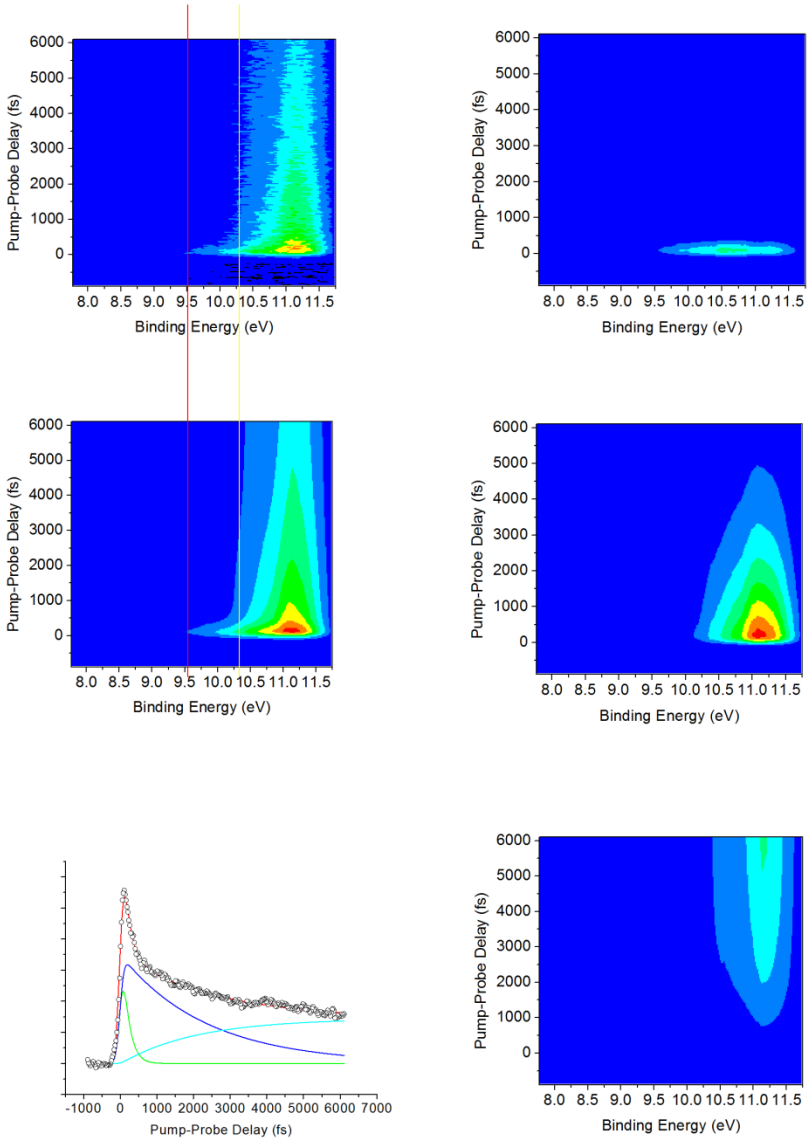

Figure 1.9 TRPES of uracil after 260 nm excitation, produced by the preliminary work in Chapter 7. The red and yellow cursors on the left correspond to IP1 and IP2, respectively.

An example of TRPES spectrum is shown in Fig. 1.9. As electron energies can be recorded, TRPES is used to extensively investigate excited state dynamics before CIs, especially the non-radiative transitions that are accompanied by electron energy changes. Ionization correlations can also be investigated through TRPES.

1.5.2 TR-TKER

Total kinetic energy release measurement, as a convenient method to determine kinetic energy of photoproducts after dissociation, has been performed with various techniques, including Photofragment Translation Spectroscopy (PTS) [40, 41 – Cronin 2004, 2006] and Velocity Map Imaging (VMI) [42 – 44 – Wei 2003, Hadden 2011, Roberts 2012].

The maximum KE available for hydrogen atoms coming off from an N-H dissociation process is

$$KE_{max} = h\nu_{phot} - D_0(N-H) - E_{int}$$

In which D_0(N-H) is the adiabatic bond dissociation energy and E_{int} is the internal energy (both electronic and vibrational) of the co-fragment, which can be neglected according to momentum conservation.

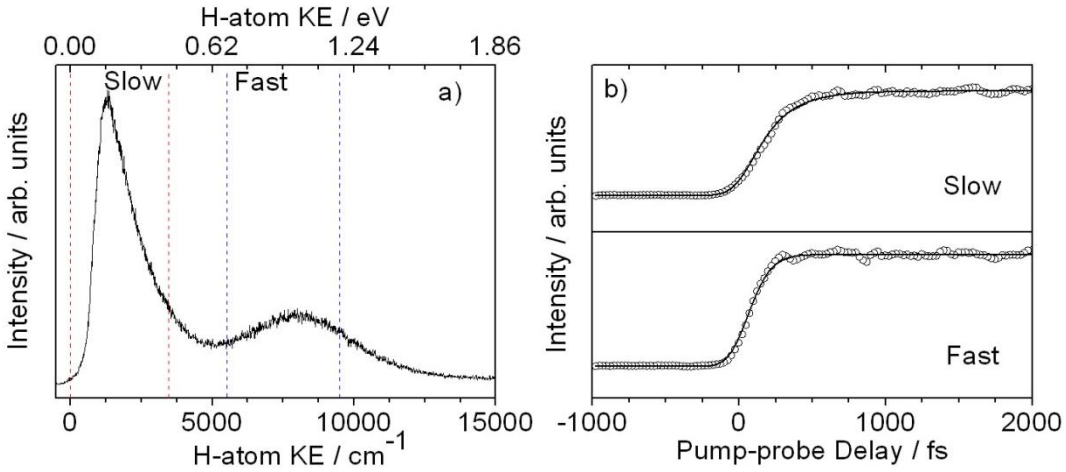

Figure 1.10 H-atom KE spectra of imidazole after 200 nm excitation, obtained by this study, referring to Chapter 3. [45 – Yu]

An example of TR-TKER spectrum is shown in Fig. 1.10. Due to its ability to separate hydrogen atoms with different KEs, the TR-TKER technique is employed specifically when more than one hydrogen dissociation channels exists. Relaxation pathways that lead to hydrogen elimination can then be studied separately, and their time-scales can be extracted.

1.5.3 TRIY

Time-Resolved Ion Yield measurements have been widely used to study fragmentation processes. High harmonic generation with 100 attosecond resolution, [46 – Haessler] and angle resolved strong-field ionization by selective excitation [47 – Kotur] have been employed to

record photoion signals. When ionization potential is reached and electrons are ejected, positive ions are repelled to the photoion detector, and both ionic state fragments and excited state fragments can be collected, depending on the number of photons included in ionization. Thus the fragmentation channels can be monitored.

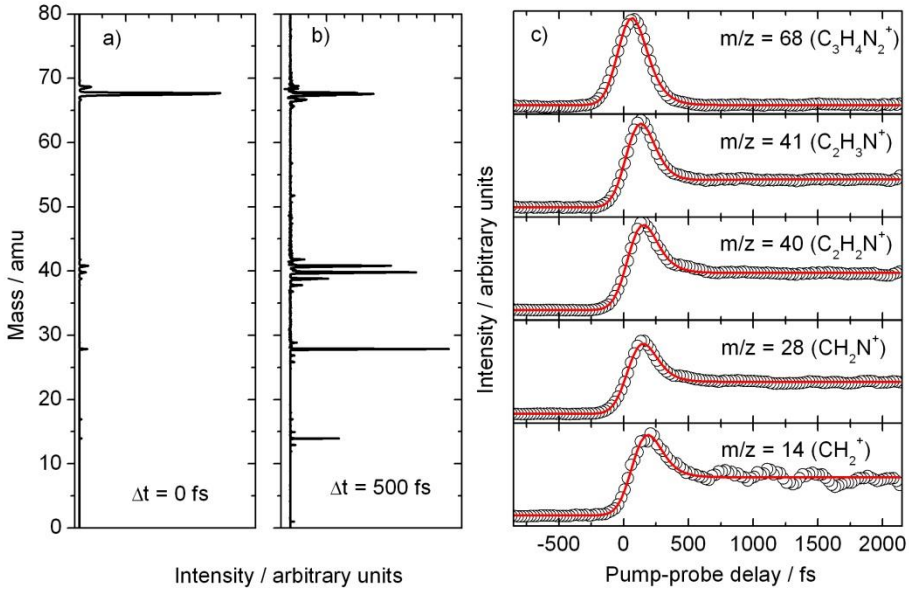

Figure 1.11 TRIY of pyrazole following 200 nm excitation, obtained by this study, referring to Chapter 5.

An example of TRIY spectrum is shown in Fig. 1.11. TRIY spectra were recorded mainly to investigate competing relaxation dynamics from different excited states. As different photofragments can be generated from specific relaxation coordinates, the time-resolved

information of all fragments, and their signal intensity relative to each other, provide important information on corresponding relaxation coordinates.

1.6 Functions used to fit time-resolved data

The time-resolved data obtained by pump-probe spectroscopy is fit with multiple functions, and time constants extracted from the fits are used to interpret excited state dynamics. Due to the ~130 fs pulse duration of our laser system, all functions used are convoluted with a Gaussian FWHM, which is measured by the calibration scans on the same days and is related to the pulse duration by

$$FWHM = G = 2\sqrt{2ln2} * w = \sqrt{2} * p.d.$$

where G is the Gaussian IRF, and w is the width in a standard Gaussian function

$$f(x) = aexp[-\frac{(x - x_c)^2}{2w^2}]$$

All transients obtained in the time-resolved experiment are fit with three main types of functions, simulated curves of which are shown in Fig. 1.12. The user defined Gaussian function

$$y = y_0 + A * exp[-\frac{2.77 * (x - x_0)^2}{G^2}]$$

is used to describe the signal that is directly associated with the laser pulse, often the timing calibration signal which has negligible lifetime. The parameter x_0 is considered center of the Gaussian, and can be measured by calibration studies.

For time-dependent signals that rise in τ after the pump-probe overlap, a user defined exponential rise function convoluted with the Gaussian IRF is used to describe the transient:

$$y = y_0 + A * \{1 + erf\frac{x - x_0}{G/1.665} - exp\frac{(G/1.665)^2 - 4\tau(x - x_0)}{4\tau^2} * [1$$

$$- erf\frac{(G/1.665)^2 - 2\tau(x - x_0)}{2\tau * (G/1.665)}]\}$$

in which erf is the error function that does Gaussian convolution to the step rise.

To describe signals that decay after excitation, a user defined exponential decay function convoluted with the Gaussian IRF is employed

$$y = y_0 + A * exp\frac{(G/1.665)^2 - 4 * dec * (x - x_0)}{4 * dec^2} * [1$$

$$- erf\frac{(G/1.665)^2 - 2 * dec * (x - x_0)}{2 * dec * (G/1.665)}]$$

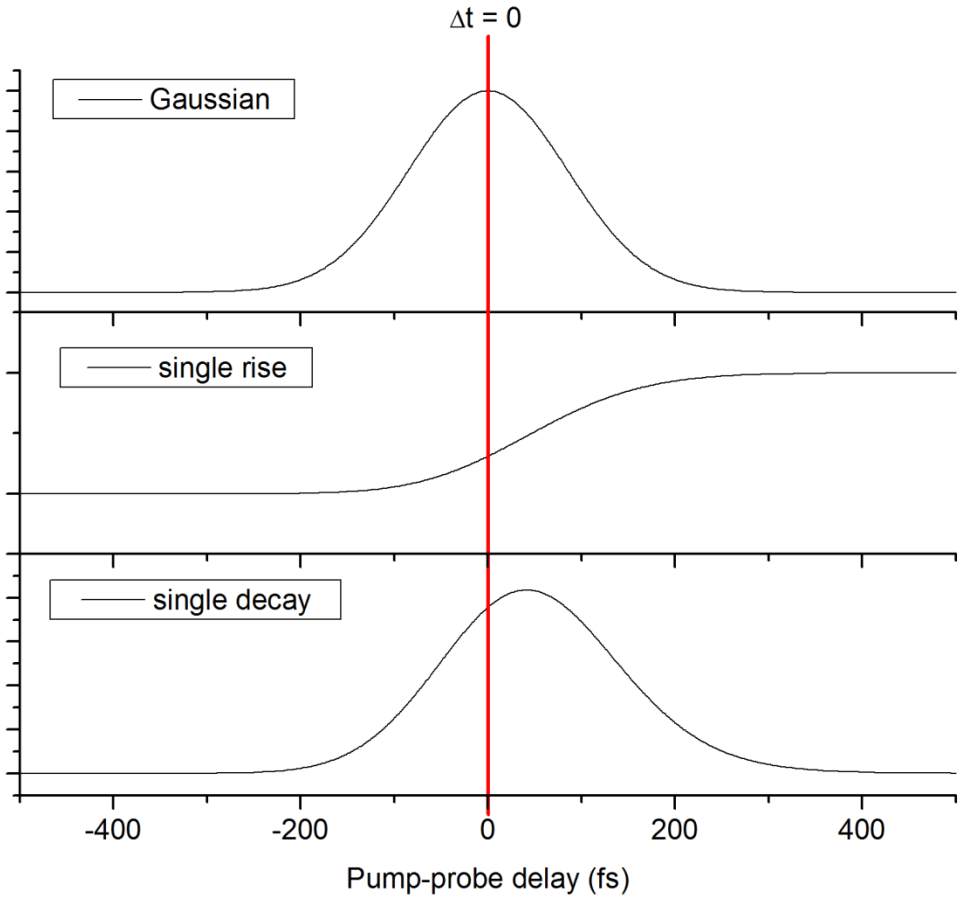

Figure 1.12 Simulation of user defined functions in Origin 8.0. G is set at 200 fs, while τ and dec in the rise and decay functions are both set to 50 fs.

For more complicated relaxation pathways on which signals rise and decay, or proceed along the probe-pump direction, a combination of the above mentioned fitting functions is used to describe the transient, and reversed functions are employed.

1.7 Outlook of thesis

Chapter 2 introduces the experimental apparatus and user designs, including the laser system, molecular beam preparation and detectors. Chapter 3 presents a TRIY and TR-TKER study of

imidazole. [45 –Yu] Chapter 4 presents a TRPES study of imidazole, collaborated with the Barbatti group. [48 – Crespo-Otero] Chapter 5 presents a TRIY study of pyrazole, collaborated with the Stavros group. [49 – Williams] Chapter 6 presents a TRIY and TR-TKER study of pyrrole. Chapter 7 presents a TRPES and TRIY study of uracil and thymine.

1.8 References

[1] M. Klessinger and J. Michl, "Excited states and photochemistry of organic molecules", *VCH*, 1995.

[2] M. Barbatti, A. J. A. Aquino, and H. Lischka, *Phys. Chem. Chem. Phys.*, 2010, 12, 4959-4967.

[3] C. E. Crespo-Hernandez, B. Cohen, P. M. Hare, and B. Kohler, *chem. Rev.* 2004, 104, 1997-2019.

[4] C. Z. Bisgaard, H. Satzger, S. Ullrich, and A. Stolow, *ChemPhysChem*, 2009, 10, 101-110.

[5] N. L. Evans, and S. Ullrich, *J. Phys. Chem. A*, 2010, 114, 11225.

[6] H.H. Telle, A. G. Urena, and R.J. Donovan, "Laser Chemistry: Spectroscopy, Dynamics & Applications", *John Wiley*, 2007.

[7] A. Jabłoński, "Efficiency of Anti-Stokes Fluorescence in Dyes", *Nature*, 1933, 131, 839-840.

[8] G. G. Stokes, *Phil. Trans.*, 1852, 146, 463.

[9] P. Atkins and J. de Paula, *Physical Chemistry*, 7th Edition, Oxford University Press, 2002.

[10] J. L. Kinsey, *Annu. Rev. Phys. Chem.*, 1977, 28, 349.

[11] J. Franck, "Elementary processes of photochemical reactions", *Transactions of the Faraday Society*, 1926, 21, 536-542.

[12] D. Boyall and K. L. Reid, *Chem. Soc. Rev.*, 1997, 26, 223.

[13] W. D. Loveland, "Modern Nuclear Chemistry", *Wiley*, 2005, p. 232.

[14] M. Bixon and J. Jortner, *J. Chem. Phys.*, 1967, 48, 715.

[15] M. Barbatti, H. Lischka, S. Salzmann, and C. M. Marian, *J. Chem. Phys.*, 2009, 130, 034305.

[16] M. Barbatti, J. Pittner, M. Pederzoli, U. Werner, R. Mitric, V. Bonacic-Koutecky, and H. Lischka, *Chem. Phys.*, 2010, 375, 26-34.

[17] C. T. Middleton, K. de La Harpe, C. Su, Y. K. Law, C. E. Crespo-Hernandez, and B. Kohler, *Annu. Rev. Phys. Chem.*, 2009, 60, 217-239.

[18] M. Barbatti, A. J. A. Aquino, J. J. Szymczak, D. Nachtigallova, P. Hobza, and H. Lischka, *PNAS*, 2010, 107, 21453-21458.

[19] S. Mai, P. Marquetand, M. Richter, J. Gonzalez-Vazquez, and L. Gonzalez, C*hemPhysChem*, 2013, 14, 2920-2931.

[20] B. Cronin, A. L. Devine, M. G. D. Nix, and M. N. R. Ashfold, *Phys. Chem. Chem. Phys.*, 2006, 8, 3440-3445.

[21] G. da Silva, E. E. Moore, and J. W. Bozzelli, *J. Phys. Chem. A*, 2006, 110, 13979-13988.

[22] M. N. R. Ashfold, B. Cronin, A. L. Devine, and M. G. D. Nix, *Science*, 2006, 312, 1637-1640.

[23] M. N. R. Ashfold, G. A. King, D. Murdock, M. G. D. Nix, T. A. A. Oliver, and A. G. Sage, *Phys. Chem. Chem. Phys.*, 2010, 12, 1218-1238.

[24] B. Cronin, M. G. D. Nix, R. H. Qadiri, and M. N. R. Ashfold, *Phys. Chem. Chem. Phys.*, 2004, 6, 5031-5041.

[25] D. J. Hadden, K. L. Wells, G. M. Roberts, L. T. Bergendahl, M. J. Paterson, and V. G. Stavros, *Phys. Chem. Chem. Phys.*, 2011, 13, 10342-10349.

[26] G. M. Roberts, C. A. Williams, H. Yu, A. S. Chatterley, J. D. Young, S. Ullrich, and V. G. Stavros, *Faraday Discuss.*, 2013, 163, 95-116.

[27] M. Vazdar, M. Eckert-Maksic, M. Barbatti and H. Lischka, *Mol. Phys.*, 2009, 107, 845-854.

[28] N. Ismail, L. Blancafort, M. Olivucci, B. Kohler, and M. A. Robb, *J. Am. Chem. Soc.*, 2002, 124, 6818-6819.

[29] X. Zhang and J. M. Herbert, *J. Phys. Chem. B*, 2014, 118, 7806-7817.

[30] D. Nachtigallova, A. J. A. Aquino, J. J. Szymczak, M. Barbatti, P. Hobza, and H. Lischka, *J. Phys. Chem. A*, 2011, 115, 5247-5255.

[31] H. R. Hudock, B. G. Levine, A. L. Thompson, H. Satzger, D. Townsend, N. Gador, S. Ullrich, A. Stolow, and T. J. Martinez, *J. Phys. Chem. A*, 2007, 111, 8500-8508.

[32] G. R. Wu, P. Hockett, and A. Stolow, *Phys. Chem. Chem. Phys.*, 2011, 13, 18447.

[33] D. R. Yarkony, Conical Intersections: Electronic Structure, Dynamics & Spectroscopy *World Scientific, Singapore*, 2004.

[34] H. Yu, N. L. Evans, A. S. Chatterley, G. M. Roberts, V. G. Stavros, and S. Ullrich, J. Phys. Chem. A, 2014, 118, 9438-9444.

[35] N. L. Evans, H. Yu, G. M. Roberts, V. G. Stavros, and S. Ullrich, *Phys. Chem. Chem. Phys.*, 2012, 14, 10401.

[36] D. M. Neumark, *Annu. Rev. Phys. Chem.*, 2001, 52, 255-277.

[37] K. Muller-Dethlefts and E. W. Schlag, *Annu. Rev. Phys. Chem.*, 1991, 42, 109-136.

[38] M. I. Al Joboury and D. W. Turner, *J. Chem. Soc.*, 1963, 37, 5141.

[39] D. W. Turner, C. Baker, A. D. Baker, and C. R. Brundle, "Molecular Photoelectron Spectroscopy", *London: Wiley*, 1970.

[40] B. Cronin, M. G. D. Nix, R. H. Qadiri, and M. N. R. Ashfold, *Phys. Chem. Chem. Phys.*, 2004, 6, 5031.

[41] B. Cronin, A. L. Devine, M. G. D. Nix, and M. N. R. Ashfold, *Phys. Chem. Chem. Phys.*, 2006, 8, 3440.

[42] J. Wei, A. Kuczmann, J. Riedel, F. Renth, and F. Temps, Phys. Chem. Chem. Phys., 2003, 5, 315-320.

[43] D. J. Hadden, K. L. Wells, G. M. Roberts, L. T. Bergendahl, M. J. Paterson, and V. G. Stavros, *Phys. Chem. Chem. Phys.*, 2011, **13**, 10342.

[44] G. M. Roberts, C. A. Williams, H. Yu, A. S. Chatterley, J. D. Young, S. Ullrich, and V. G. Stavros, *Faraday Discuss.*, 2013, 163, 95-116.

[45] H. Yu, N. L. Evans, V. G. Stavros, and S. Ullrich, *Phys. Chem. Chem. Phys.*, 2012, 14, 6266-6272.

[46] S. Haessler, J. Caillat, W. Boutu, C. Giovanetti-Teixeira, T. Ruchon, T. Auguste, Z. Diveki, P. Breger, A. Maquet, B. Carre, R Taieb, and P. Salieres, *Nat. Phys.*, 2010, 6, 200-206.

[47] M. Kotur, T. C. Weinacht, C. Zhou, and S. Matsika, *IEEE Journal of Selected Topics in Quantum Electronics*, 2012, 18, 187-194.

[48] R. Crespo-Otero, M. Barbatti, H. Yu, N. L. Evans, and S. Ullrich, *ChemPhysChem.*, 2011, 12, 3365-3375.

[49] C. A. Williams, G. M. Roberts, H. Yu, N. L. Evans, S. Ullrich, and V. G. Stavros, *J. Phys. Chem. A*, 2012, 116, 2600-2609.

CHAPTER 2

EXPERIMENTAL

The experimental setup in this thesis consists of a fs pulsed laser system with UV conversion and wavelength tuning capabilities, a gaseous molecular beam source generated under vacuum, a magnetic bottle energy spectrometer, and a TOF mass spectrometer.

2.1 Pulsed laser

The laser system that is used for the experiments made up of a Verdi G5 pump laser, a MIRA-900 oscillator, a Legend-Elite HE pulse stretcher and amplifier pair, two optical parametric amplifiers (TOPAS-C and OPerA), all of which are commercially available from Coherent Inc., as shown in Fig. 2.1. A custom built fourth harmonic generator is also shown at bottom right.

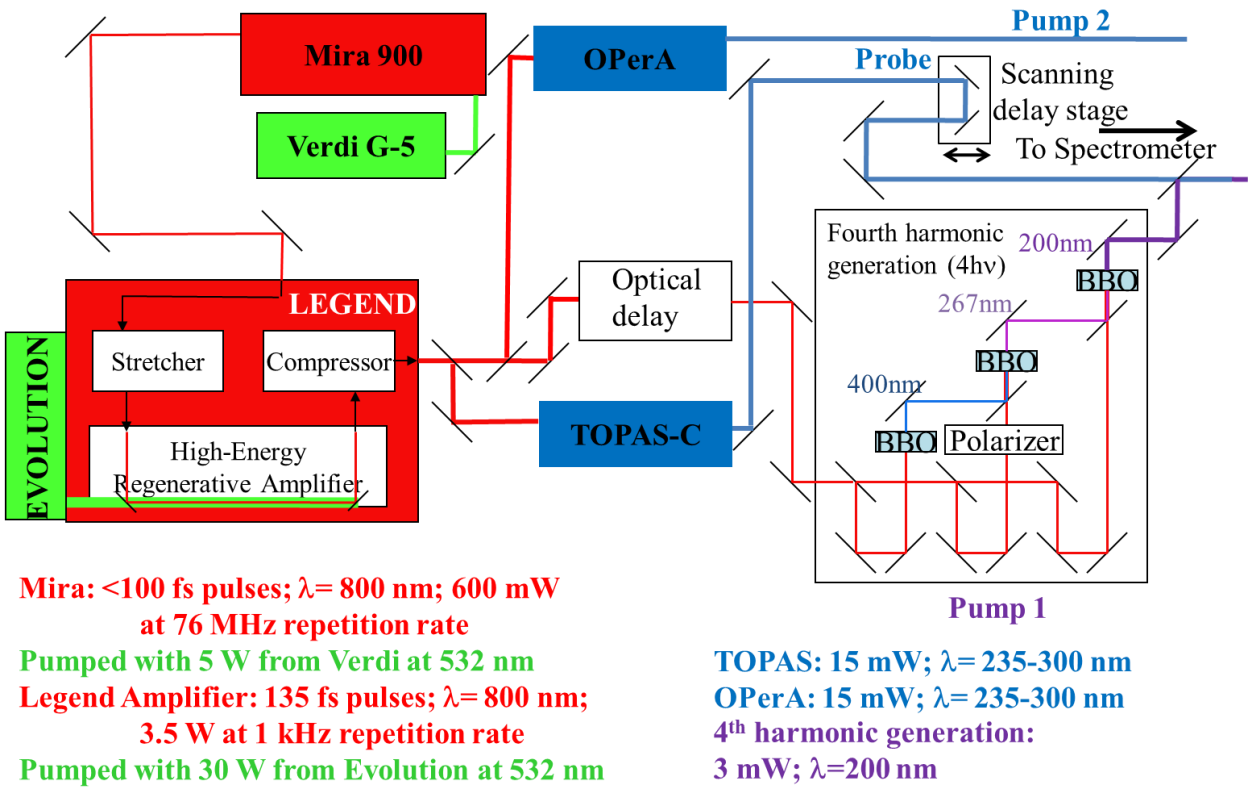

Figure 2.1 Optical paths of the laser used in the experiment. Arrows are drawn with the same color as the corresponding laser beam.

The Verdi G-5 pump laser is based on Optically Pumped Semiconductor Laser (OPSL) technology and provides 5 W of CW output at 532 nm. It is composed of a III-V semiconductor chip as the gain medium, and uses a diode laser as the pump source.

The Verdi output is sent into MIRA-900, a modelocked Ti:Sapphire oscillator. The Ti:Sapphire laser was first constructed in 1982, [1 – Moulton] with Ti^{3+} ions embedded in the sapphire (Al_2O_3) host material replacing an Al^{3+} ions, and has become widely used due to its wide tuning range. [2 – Telle] The oscillator output is up to 600 mW, and the laser pulse has <100 fs duration and 11 nm bandwidth centered at 800 nm.

Chirped pulse amplification (CPA) is provided to the oscillator output. The initial fs pulse is stretched in time, followed by amplification of the pulse, and then recompressed to its original pulse duration. [2 – Telle] (Fig. 2.2) Power is amplified to 3.3 W in the output beam, with 130 fs duration and 1 kHz repetition rate.

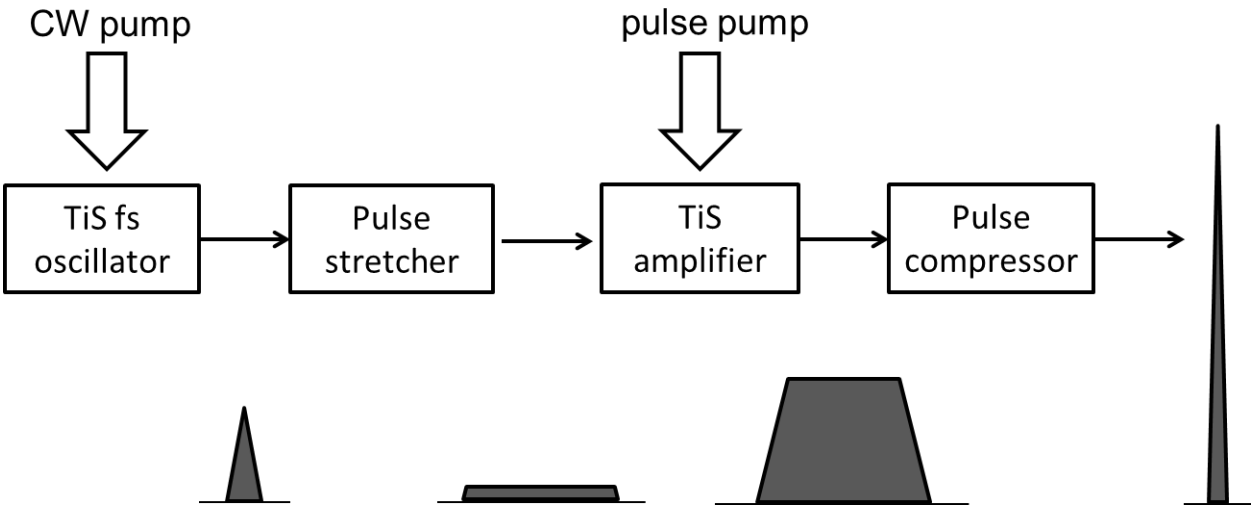

Figure 2.2 Schematic picture explaining pulse amplification.

2.2 SHG and SFG

The photon energy required to excited and ionize the investigated molecules are significantly higher than the <2 eV from the amplifier output (1 kHz, 800 nm, 130 fs, 3.3 mJ/pulse), therefore it is split to produce UV pump and probe pulses at different wavelengths in subsequent frequency conversion steps. UV pulses with wavelengths fixed at the third (267 nm) or fourth harmonic (200 nm) of the amplifier fundamental are produced in Type-I BBO crystals in a custom-built setup employing SHG and SFG.

The SFG is a process of producing light whose frequency is the sum of the two incident beams. [3 – Paschotta]

The polarization of medium changes with the interacting electric field from the laser pulse, [2 – Telle]

$$\boldsymbol{P} = \varepsilon_0(\chi \boldsymbol{E} + \chi^2 \boldsymbol{E}^2 + \cdots)$$

in which χ is the electric susceptibility of the material and ε_0 is permittivity of free space. Waves are represented in the form of

$$\boldsymbol{E} = \boldsymbol{E_0}\sin(\omega t)$$

To achieve phase matching condition after frequency conversion steps, relation

$$\omega_f = \omega_1 + \omega_2$$

needs to be met, and crystals need to be cut at the same angle as the laser polarizations for phase matching, which are the Type-I BBO crystals used in our setup. The SHG process is a special case of SFG, with

$$\omega_1 = \omega_2$$

in equation above [4 – Franken] and

$$\omega_f = 2\,\omega_1$$

UV pulses with tunable wavelengths are prepared by Optical Parametric Amplifier (OPerA) and Traveling-wave Optical Parametric Amplifier of a White-light Continuum (Light Conversion, TOPAS-C).

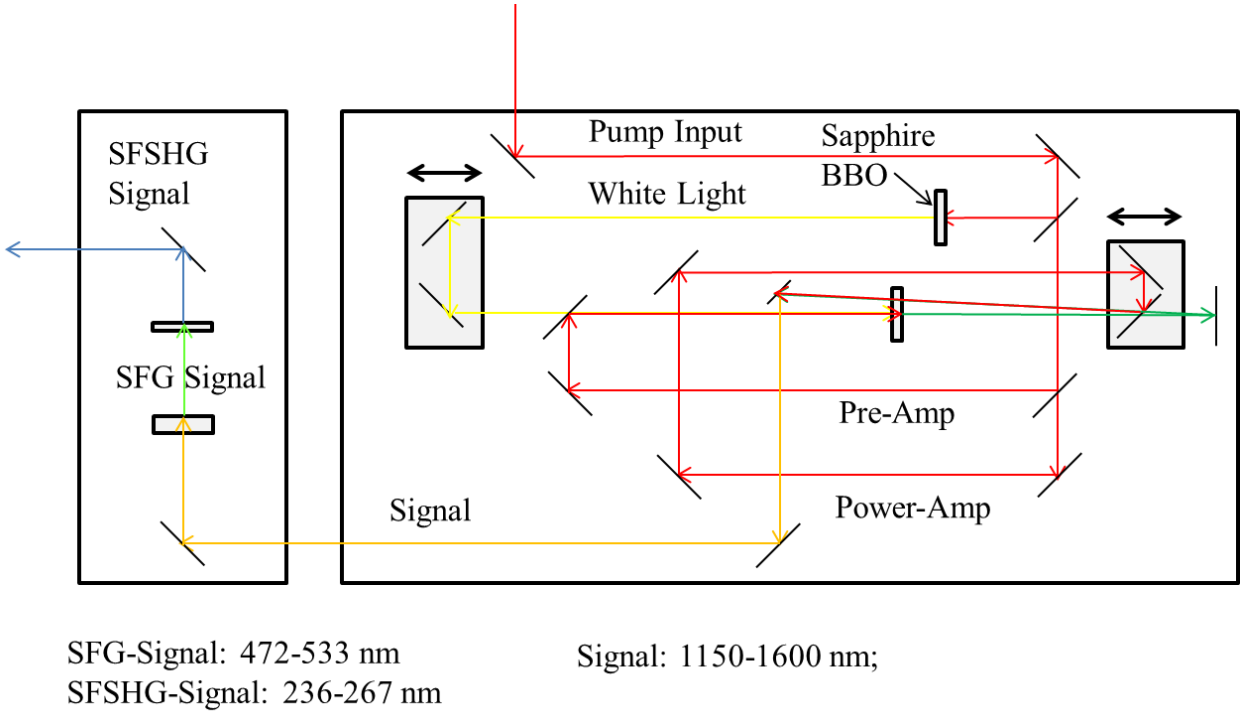

Figure 2.3 SFSHG signal path from OPerA.

The SFSHG signal path from OPerA is shown in Fig. 2.3, as an illustration to the OPA working mechanism. A small fraction of the pump input is focused into a sapphire window to generate a white light continuum through a non-linear process. Another portion of the pump input, which serves as the pre-amplifier path, is focused and recombined with the white light in a non-centrosymmetric crystal which allows type-II phase matching (the two input pulses are perpendicularly polarized). This mixing process is called Optical Parametric Amplification. [5 – OperA menu] The timing overlap of the white light and the pre-amp path is controlled by a delay stage along the white light path. Two output beams with different wavelengths can be obtained by adjusting the OPA crystal angle. During an OPA process, the shortest wavelength beam is called the “pump”, and the output beams are called the “signal” and the “idler”, with a relationship

$$w_{pump} = w_{signal} + w_{idler}$$

The remaining pump light, as the power amplifier, is overlapped with the signal and idler at the OPA crystal again. The timing of the power-amp path is controlled by another delay stage. Several output options can be obtained from the OPA "signal" by inserting crystals into the beam path in the smaller box on the left (Fig. 2.3), including: (1) the signal itself; (2) the second harmonic generation (SHG) from the signal; (3) the fourth harmonic generation (FHG) from the signal; (4) sum-frequency generation (SFG) by mixing the signal and the power-amp beam; (5) and the second harmonic of the SFG-signal, which is defined as SFSHG. These five options are also available for the OPA "idler". As a result, a wide wavelength tuning range from 235 nm to 2630 nm is made possible, and a specific output wavelength can be selected by choosing one of the above mentioned options. In our work, SFSHG of the signal and the idler are selected, which are in the UV-vis range (235 nm – 295 nm).

2.3 Laser power, alignment and focusing

A computer controlled motorized optical delay line (Newport ILS150PP with ESP 300 controller) is used to time-delay the pump and probe pulses relative to each other. The two beams are spatially overlapped at the interaction region with the molecular beam. They are either subsequently combined at a dichroic beamsplitter and focused (f = 50 cm) collinearly, or focused separately (f = 50 cm) and combined at an angle, before being sent into the interaction region of the spectrometer through a UV fused silica window, as shown in Fig. 2.4. In a few circumstances (Chapter 6) when REMPI of hydrogen is needed and the probe power is not high enough, a focusing lens with f = 30 cm is chosen for the probe path.

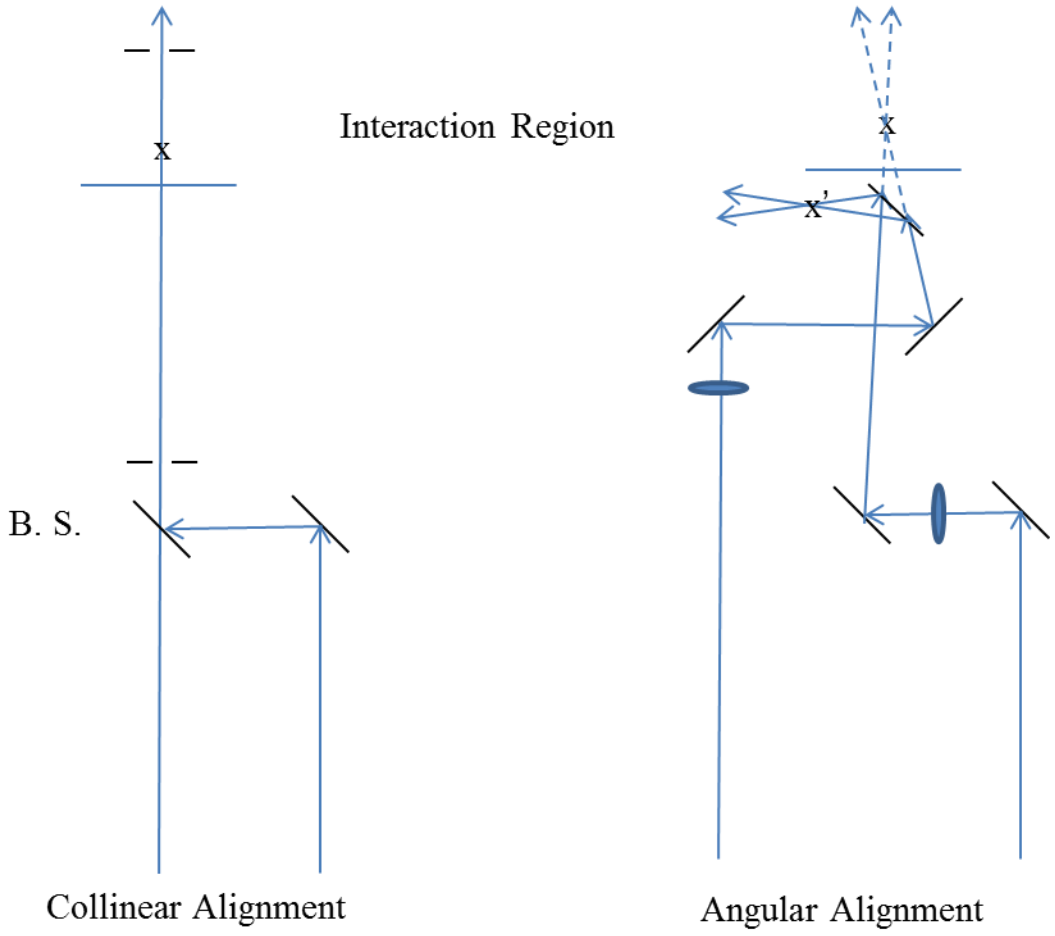

Figure 2.4 The two overlapping strategies. "X" indicates the point where laser interaction with the molecular beam is expected to happen.

Collinear overlap is used when the wavelengths of the pump and probe beams differ significantly (>30 nm), so that the reflection and transmission rate of the dichroic beam splitter are both large. When the two beams are very close in wavelength and the dichroic beam splitter cannot function properly, the angular overlap needs to be applied. The laser power loss before entering the interaction region is minimized in the angular setup, although it is more difficult to determine the interaction point.

As the interaction takes place under vacuum, laser position at the interaction point cannot be directly observed. Collinear overlap is optimized by setting up two irises, one before and one after the vacuum spectrometer, to ensure that the two beams are collinear along a long enough path so that they overlap spatially at the interaction point X. Angular overlap is adjusted in a different way. A portable mirror is placed temporarily into the beams before they enter the interaction region. A 50 μm pinhole is placed at a location X' that has roughly the same distance to the portable mirror as the distance between the portable mirror and the interaction point X. Both the pump and probe beams are adjusted to pass through the pinhole at X', so that they overlap spatially at the interaction point X too.

2.4 Timing calibration

As introduced in Chapter 1.4.2, the pump-probe mechanism of investigated molecules starts after the timing overlap of the pump and the probe pulse. Therefore the relative timing of the two laser beams need to be calibrated with sample molecules. Non-resonant TRPES or TRIY spectra of pyrrole, 1, 3 – butadiene or ammonia have been recorded for timing calibrations at low laser power in specific experiments, as symmetric Gaussian cross-correlation function can be used to describe their time-profile around zero pump-probe delay, and no probe-pump signal exist to interfere with the Gaussian. These scans allow us to determine the temporal overlap between pump and probe pulses ($\Delta t = 0$ fs) and also the time resolution of each experiment - referred to as the instrument response function (IRF; laser cross correlation of typically 200 - 250 fs).

2.5 Source chamber

Solid state heterocyclic molecules imidazole, pyrazole and pyrrole, and nucleo bases uracil and thymine that are pyrimidine derivatives (Sigma Aldrich, ≥98%) are prepared in a quartz sample holder, which is located just before the nozzle pinhole in a vacuum chamber and heated to 70 ℃, 40 ℃, 30 ℃, 210 ℃, and 175 ℃ to evaporate, respectively. A continuous molecular beam of sample vapor is carried by Helium backing gas (50 Torr) and doubly skimmed to allow differential pumping between the vacuum source chamber at 10^{-6} Torr and ultrahigh vacuum chamber at 10^{-8} Torr, where the detectors are located. The molecular beam is intersected by the UV fs pump pulse and the time-delayed probe pulse that are overlapped and focused. A schematic picture of the molecular beam preparation system is shown in Fig. 2.5.

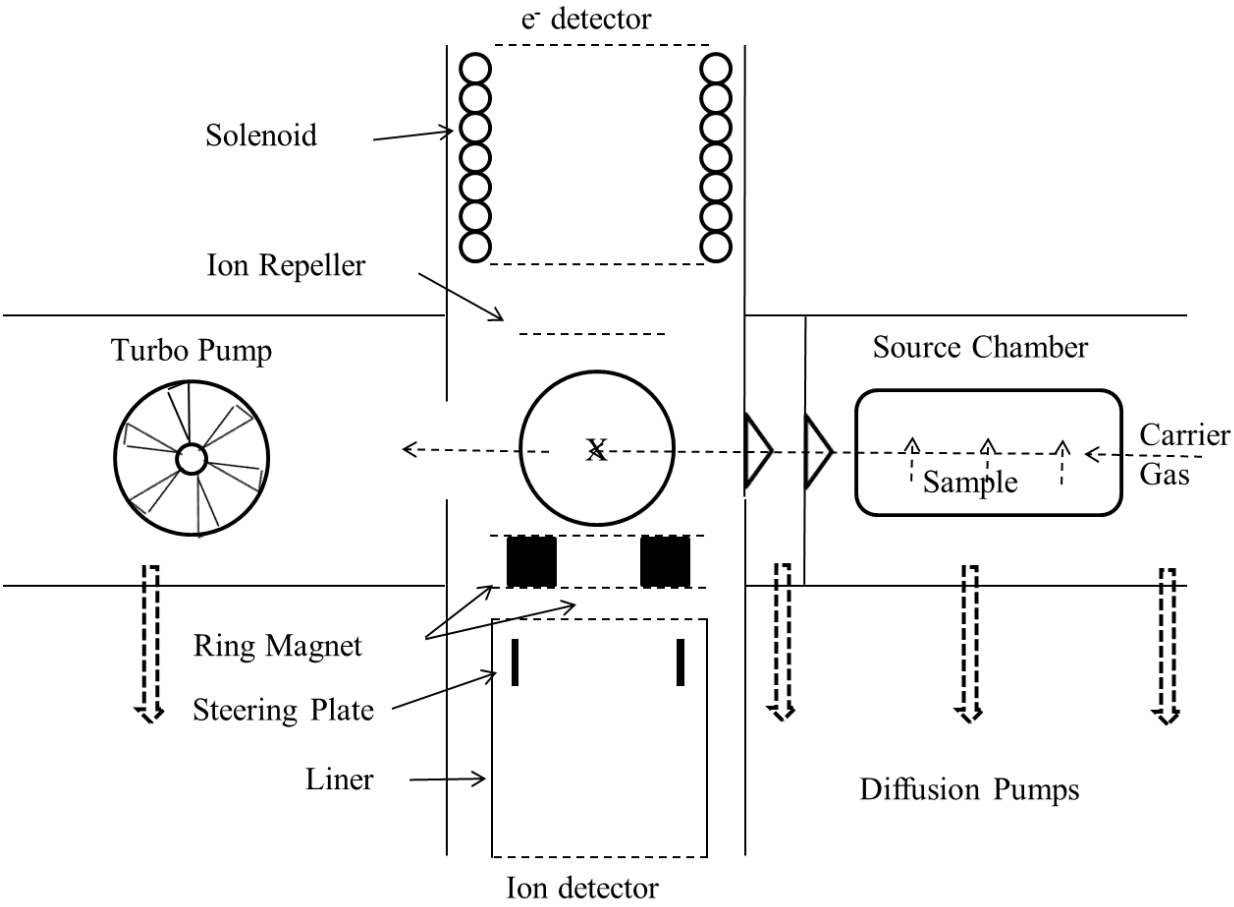

Figure 2.5 A schematic picture of molecular beam preparation, interaction region, and spectrometers. “X” is where the molecular beam intersects the laser.

Vapor diffusion pumps (VHS-6, Varian) are used to reduce pressure from the source chamber, by momentum transfer from a directed stream of oil vapor. As shown in Fig. 2.6, when operating, working fluid is evaporated by heating from boiler at the bottom, and conducted upward through a tower to an array of nozzles, before being emitted downward and outward toward water-cooled pump and condense. The condensate runs down the pump wall to return to the boiler. The boiler is typically heated to 200 ℃ while the top of the pump wall is cooled down to 30 ℃ by the cooling water to effectively condensate vapor. [6 – Moore]

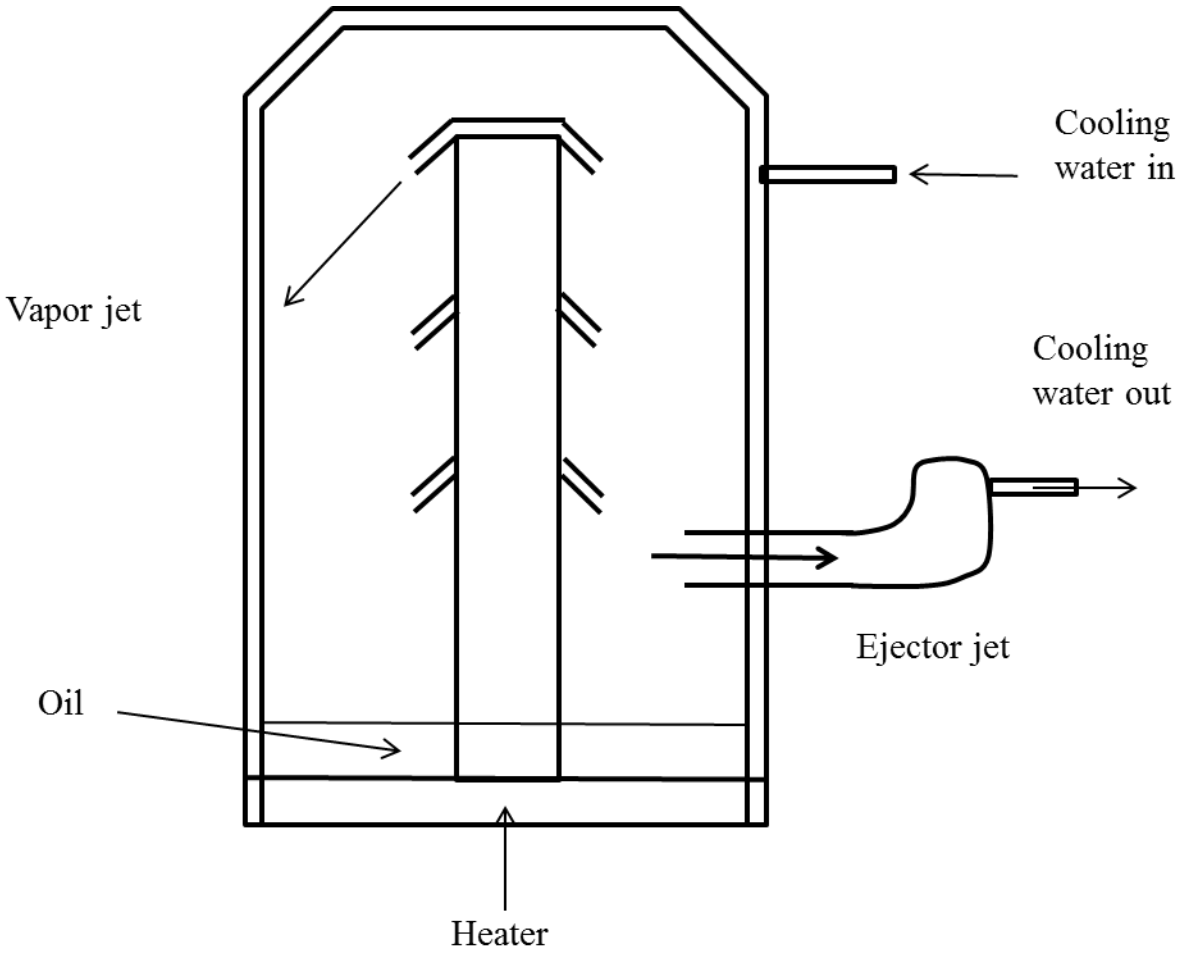

Figure 2.6 Diffusion pump working mechanism.

The spectrometers operate under ultrahigh vacuum (10^{-8} Torr) produced by a turbo molecular pump (Mitsubishi Turbo-Molecular Pump, FT-3301W). A series of rotor blades turn at 20,000 to 90,000 rpm, and are canted so that molecules hitting the blades receives a significant component of velocity in the direction of the pump exhaust [5]. The ultrahigh vacuum is generated out of normal vacuum (10^{-3} Torr), which is produced by a roughing pump (Pascal Tech., NEWCH Duo-Seal Vacuum Pump).

2.6 Spectrometers

A magnetic bottle spectrometer facilitates kinetic energy analysis of photoelectrons and kinetic energy release from hydrogen atoms, and an ion mass spectrometer collects photoions, via time-of-flight measurements.

The time-of-flight mass spectrometer (lower half, Fig. 2.5) consists of a Wiley-McLaren configuration [7 – Wiley] modified to accommodate a permanent ring magnet, which is utilized by the magnetic-bottle spectrometer. Photoions from photofragmentation and the ionized parent molecules are accelerated out of the source toward the collector by a series of constant electric fields. A positive voltage of +1500 V is applied to the ion repeller grids above the interaction region, and the entrance grids to the ion flight tube are grounded, so that a constant potential decrease is created from top to bottom in the interaction region to accelerate the ions downwards. A liner voltage of +1500 V is applied to the flight tube walls, so that the electric field remains constant through the flight tube to the ion detector at the bottom. Steering plates by both x and y orientation, are placed at the beginning of the flight tube to regulate the flown direction. As the molecular beam ejects into the interaction region from right to left (Fig. 2.6), photoions that are generated preserve an initial velocity toward the left. The x-steering plate is typically charged to +1400 – +1480 V, so that the potential difference between the steering plate and U-shaped plate opposite to the steering plate can compensate for the initial leftward momentum, and it can make most of the ions go straight down to the detector, which is charged at -4500 V. Depending on the specific photoions of interest, the x-steering voltage is set to closer to (for smaller masses) or further away from (for larger masses) the liner voltage, to guarantee that most photoions of this specific mass fly straight down to the detector. The y-steering plate is left at the same voltage as the liner, as no significant deviation from the molecular beam exists in the direction of the laser

pulse. Photoions of different atomic masses are collected with different time-of-flight (TOF), which are converted to molar masses by TOF to mass calibration scans from ammonia (NH_3) or 1, 3- butadiene, discussed in section 2.7.

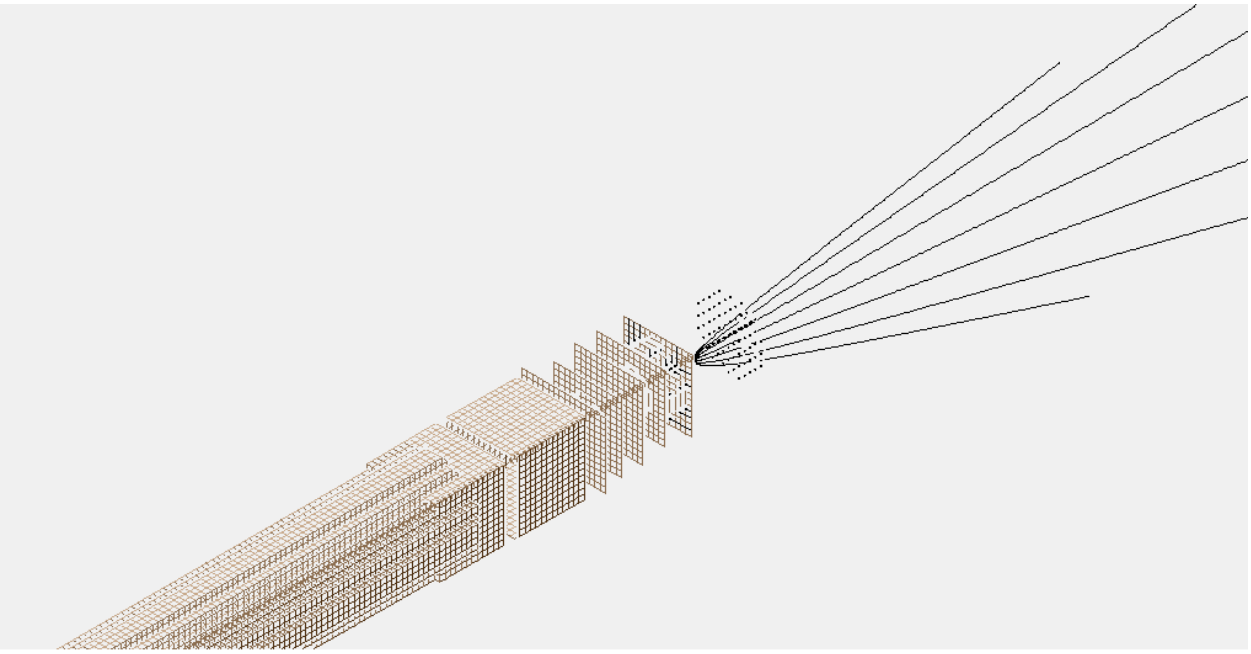

Figure 2.7 Simulated high KE electron trajectories by the magnetic field effect only in a TRPES study. Electrons with initial velocity at all directions are turned to the right by the magnetic field.

A magnetic-bottle energy spectrometer based on the design of Kruit and Read [8 – Kruit] is used to measure hydrogen TRPES and TR-TKER spectra. The magnetic-bottle-type photoelectron spectrometer consists of a permanent ring magnet and a linear solenoid. Photoelectrons are emitted with initial speed in all directions, and if their initial kinetic energies are not too high, most of the trajectories are turned toward the solenoid by the inhomogeneous ring magnet field according to the Lorentz' law (Fig. 2.7)

$$\boldsymbol{F} = q\boldsymbol{v} \times \boldsymbol{B}$$

and follow helical paths along the magnetic field lines within the solenoid (Fig. 2.8) to a microchannel plate electron detector, which is charged at +4500 – +4800 V. Magnetic-bottle electron spectrometers provide a combination of collection efficiency and energy resolution – allowing efficient collection of electrons with KEs of 0.3 eV – 4.5 eV, which is well suited to the excited state dynamic studies, and the energy resolution is limited by the femtosecond pulse bandwidth.

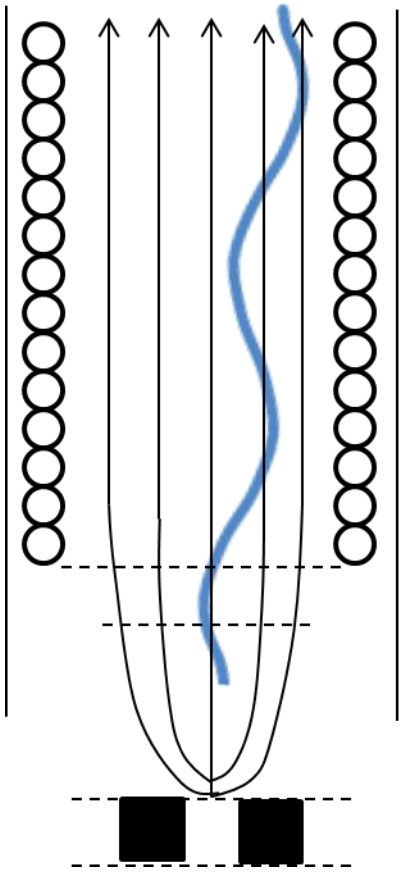

Figure 2.8 Sketch of low KE photoelectron trajectories in the electro-magnetic field.

For hydrogen KE spectra measurement, a repelling potential of +10 – +14 V is applied to the magnet grid to boost the collection efficiency for photoionized H-atoms. In both spectrometers, TOF spectra are recorded by a 2-channel multiscaler (FAST Comtech P7888-2) with 1 ns time resolution. In operation the sweep is started by a user supplied start (trigger) pulse. Photoelectrons/photoions reaching end of the flight tube are accelerated to the detector, and detected as the stop pulses, each in a specific time bin corresponding to the time of arrival relative to the start pulse. (Fig. 2.9) [9 – FAST ComTech]

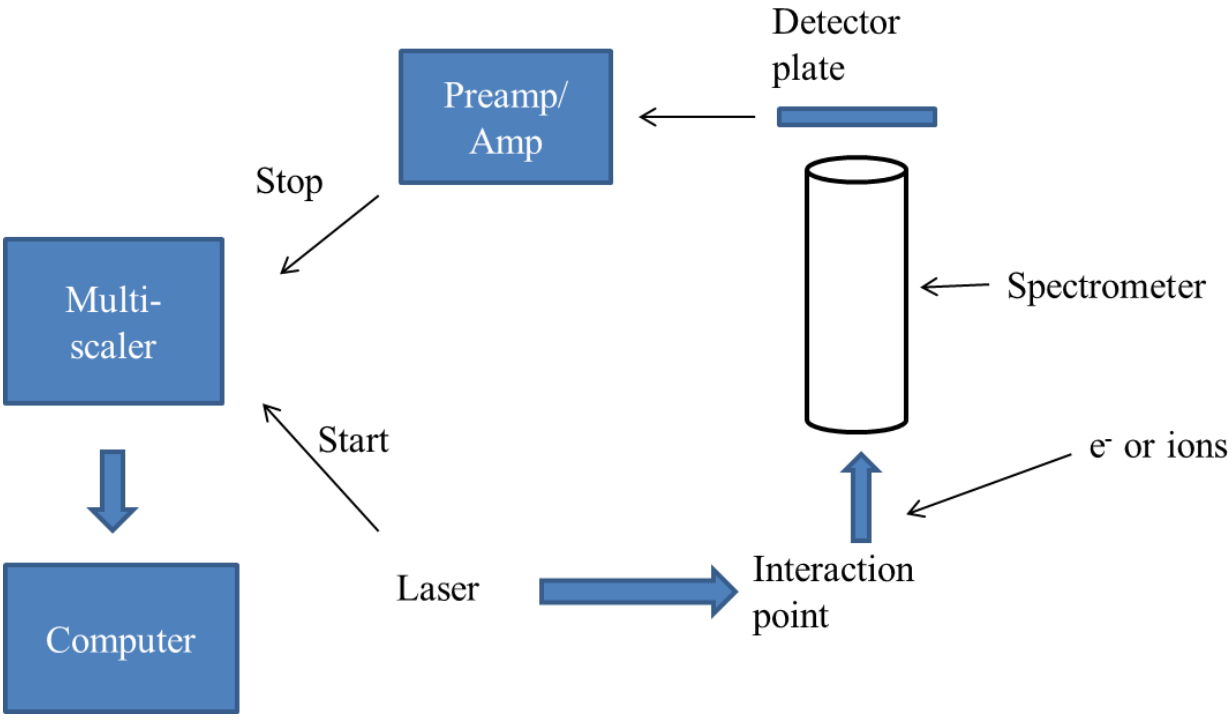

Figure 2.9 Schematic picture of the multiscaler detectors.

2.7 TOF to energy/mass calibration

TOF to photoelectron kinetic energy calibrations are performed by recording energy peaks from 1, 3-butadiene (C_4H_6). As

$$E_k \propto v^2 \propto \frac{1}{TOF^2}$$

the TOFs of the butadiene peaks are correlated to kinetic energies by

$$E_k = \frac{IR}{(TOF - T_0)^2} - E_0$$

in which IR is the slope, and T_0 and E_0 are deviations in TOF and energy, respectively. The kinetic energies of butadiene peaks are calculated from

$$E_k = E_{phot} - I.P.$$

where E_{phot} is the total photon energy, and *I. P.* is the known ionization potentials of 1, 3 – butadiene obtained from He(I) PES. [10, 11 – Eland, Turner]

TOF to H-atom kinetic energy calibrations are performed by tracking the shift of the zero kinetic energy onset in the spectrum, as a small repelling voltage is varied. The ionization region occurs at ~¾ the distance from the magnet to the grounded flight-tube entrance grid, therefore the acceleration potential experienced by the H-ions in the ionization region strongly depends on the height of the laser beam. The ratio of the effective versus applied potential is determined based on energetic shifts in 1, 3-butadiene photoelectron spectra, as shown in Fig. 2.10. The three photoelectron peaks of butadiene are shifted towards lower TOF when an increasing repelling voltage is applied. By applying TOF to photoelectron kinetic energy calibration mentioned above, the kinetic energy increase caused by applied voltage can be determined. This increased energy from the applied potential has been directly subtracted to yield the TKER spectrum.

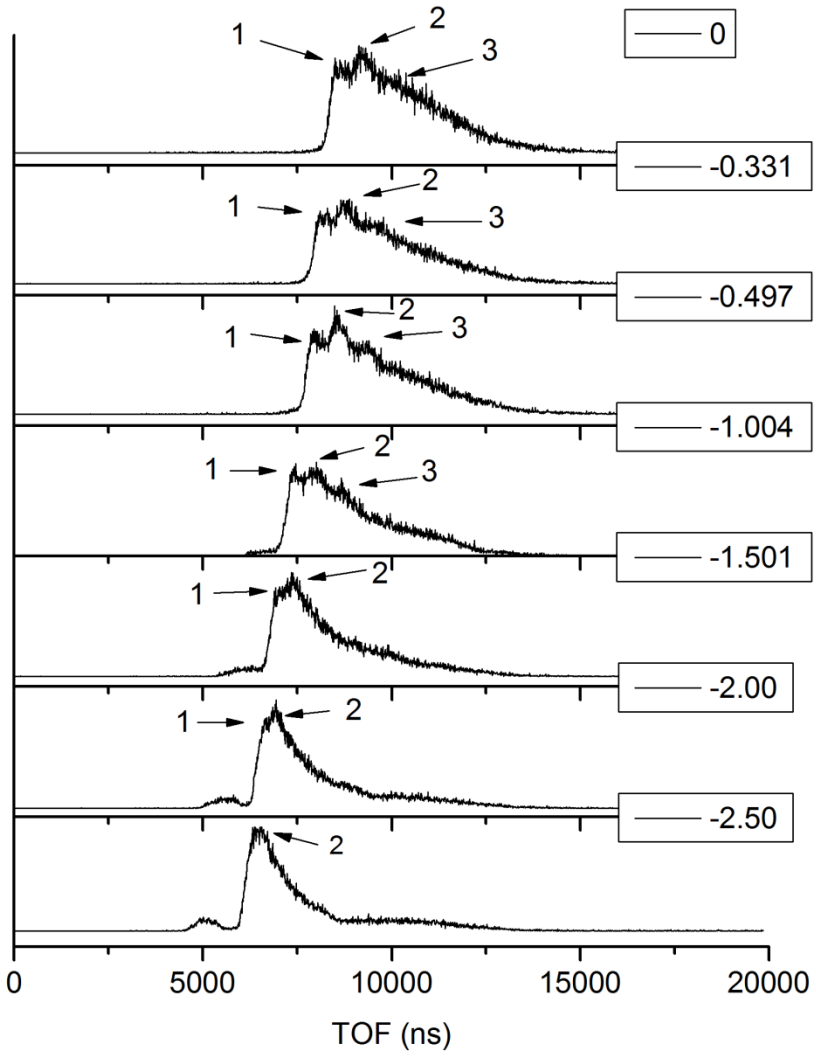

Figure 2.10 The TOFs of the three photoelectron peaks from 1, 3-butadiene shift as the voltage applied on the magnet changes from 0 V to – 2.05 V. The voltages applied are indicated at top right of each layer. Photoelectron peaks that are labeled with the same number are correlated to the same ionization potential.

TOF to atomic mass calibrations are performed by recording ion mass spectra with known atomic masses. As

$$M \propto \frac{1}{v^2} \propto TOF^2$$

the TOFs of the mass peaks can be obtained by

$$M = IR * (TOF - T_0)^2 + M_0$$

where T_0 and M_0 are deviations from TOF and atomic masses, respectively.

2.8 References

[1] P. F. Moulton, *Journal of the Optical Society of America B*, 1986, 3, 125–133.

[2] H. H. Telle, A. G. Urena, and R.J. Donovan, "Laser Chemistry: Spectroscopy, Dynamics & Applications", *John Wiley*, 2007.

[3] R. Paschotta, "Encyclopedia for Photonics and Laser Technology", *Wiley-VCH*, 2008.

[4] P. A. Franken, A. E. Hill, C. W. Peters, and G. Weinreich, *Phys. Rev. Lett.*, 1961, 7, 118.

[5] Operator's Manual, The Coherent OPerA™, http://laser.coherent.com

[6] J. H. Moore, C. C. Davis, and M. A. Coplan, "Building Scientific Apparatus, 3rd edition", *Massachusetts: Perseus Books*, 2003.

[7] W. C. Wiley and I. H. McLaren, *Rev. Sci. Instruments*, 1955, 26, 1150.

[8] P. Kruit and F. H. Read, *J. Phys. E.*, 1983, 16, 313.

[9] FAST ComTe datasheet, http://www.fastcomtec.com

[10] J. D. H. Eland, *Int. J. Mass Spectrom. Ion Phys.* 1969, *2*, 471-484.

[11] D. W. Turner, C. Baker, A. D. Baker, and C. R. Brundle, "Molecular Photoelectron Spectroscopy", *London: Wiley*, 1970.

CHAPTER 3

INVESTIGATION OF MULTIPLE ELECTRONIC EXCITED STATE RELAXATION PATHWAYS FOLLOWING 200 NM PHOTOLYSIS OF GAS-PHASE IMIDAZOLE[3]

[3] H. Yu, N. L. Evans, V. G. Stavros, and S. Ullrich, *Phys. Chem. Chem. Phys.*, 2012, 14, 6266-6272. Reprinted here with permission from the publisher.

3.1 Abstract

Imidazole acts as a subunit in the DNA base adenine and the amino acid histidine – both important biomolecules which display low fluorescence quantum yields following UV excitation. The low fluorescence quantum yields are attributed to competing non-radiative excited state relaxation pathways that operate on ultrafast timescales. Imidazole is investigated here as a model compound due to its accessibility to high level *ab initio* calculations and time-resolved gas-phase spectroscopic techniques. Recent non-adiabatic dynamics simulations have identified three non-radiative relaxation mechanisms which are active following 6.0 - 6.2 eV excitation. Presented herein is a comprehensive investigation of each mechanism using a combination of femtosecond time-resolved ion yield and total kinetic energy release spectroscopies to monitor the formation of associated photoproducts. Relaxation along the $^1\pi\sigma_{NH}$* state constitutes the predominant deactivation pathway. Timescales for NH-dissociation are extracted and distinguished from alternative H-atom sources based on their kinetic energy distributions. Larger photoproducts are observed to a lesser extent and attributed to ring fragmentation following NH-puckering and CN-stretching relaxation paths.

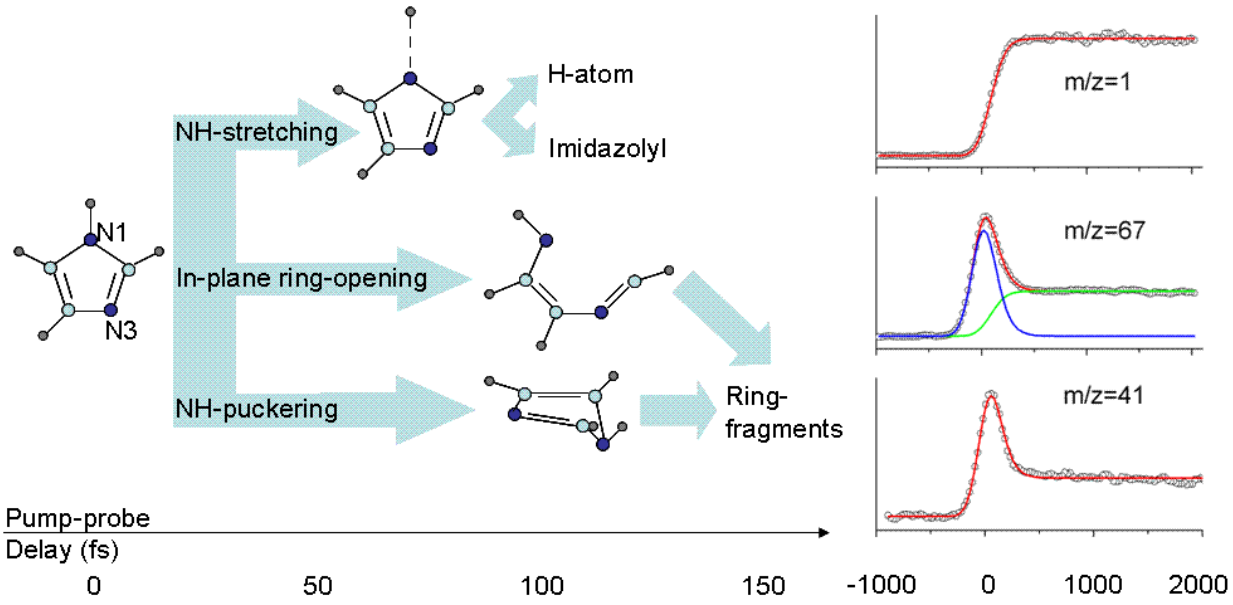

Figure 3.1 Graphical guideline of this work.

3.2 Introduction

Interest in the photophysical and photochemical processes of small biomolecules has been significant given their importance to our existence. For example, the photodynamics of the DNA base adenine, have been studied extensively both experimentally [1 – 5] and theoretically. [6, 7] Following ultraviolet (UV) excitation, adenine relaxes from the electronically excited state back to the ground state on femtosecond (fs) timescales–providing an inherent self-protection mechanism against potentially harmful radiation. As numerous publications, [3, 5, 8] with sometimes contradictory conclusions demonstrate, the relaxation dynamics of adenine are rather complex and competing pathways are difficult to disentangle. Deactivation through $^{1}\pi\sigma^{*}$ states is seemingly ubiquitous in nitrogen containing heterocycles however, their energetic onset is under debate for many molecules [9, 10] including adenine. Other deactivation mechanisms under

investigation include $^1(\pi,n)\pi^*$ pathways along ring puckering coordinates. [11] These have motivated the present study. Imidazole (Fig. 3.2), the five-membered heterocyclic subunit of adenine, also displays $^1\pi\sigma^*$ [9] and $^1\pi\pi^* \rightarrow$ ring deformation [12] mediated electronic relaxation, and therefore constitutes a model system for these mechanisms that may be easier to tackle in experimental and theoretical studies. Most importantly it can provide a detailed insight into the energetics and dynamics of these relaxation pathways which can subsequently be used to verify their presence within more complex molecules.

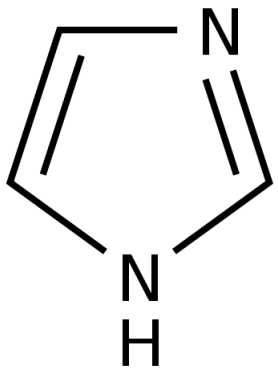

Figure 3.2 Molecular structure of imidazole.

The steady-state, gas-phase UV absorption spectrum of imidazole [13, 14] shows an onset around 243 nm, with a significant increase in absorption from approximately 220 nm toward 190 nm. The curve contour is generally broad with discernible peaks near 198 nm and 194 nm. Interpretation of this spectrum has come via ab initio quantum chemical calculations at various levels of theory. [12, 15 – 19] The highest occupied molecular orbitals (HOMOs) of imidazole have been identified as two π (3a″ and 2a″) orbitals and one nitrogen lone pair (15a′) orbital. [19] Four transitions from the HOMO are responsible for the low energy region of the imidazole absorption spectrum. An intense singlet $^1\pi\pi^*$ transition centered around 204 nm and the rising

band of a second intense singlet $^1\pi\pi^*$ transition just below 190 nm are responsible for the overall broad shape of the spectrum. In close energetic proximity to the $^1\pi\pi^*$ transitions lie $^1\pi\sigma_{CH}^*$ and $^1n\sigma_{NH}^*$ (3s) states with non-zero oscillator strengths, to which, sharp features in the absorption spectrum at 198 and 194 nm have been assigned, respectively. Note, that although the dipole allowed $S_0 \rightarrow {}^1\pi\sigma_{NH}^*$ (3s) transition is computed as being the lowest energy singlet excited state, symmetry considerations suggest an almost zero intensity for this transition. [12] It is then assumed that $^1\pi\sigma_{NH}^*$ (3s) absorption is very weak and contributes only to the long wavelength onset of the spectrum. [15]

Radiationless deactivation of low lying UV-excited states in imidazole has recently been investigated by high-level non-adiabatic dynamics simulations. [12, 20] Four conical intersections (CI) with S_0 have been identified, and are described as: (i) NH-stretching ($^1\pi\sigma_{NH}^*/S_0$), (ii) CN-stretching (planar ring-opening, $^1\pi\sigma_{CN}^*/S_0$), (iii) NH-puckering, and (iv) N-puckering. [12] Reaction paths, leading from the Franck–Condon region to these CIs, have also been characterized, [12] but dynamics calculations show that only the first three channels are active after excitation to the $^1\pi\pi^*$ state in the 6.0–6.2 eV window. [20] The NH-stretching CI ($^1\pi\sigma_{NH}^*/S_0$) lies 4.3–4.4 eV above the ground state and requires the least amount of geometric deformation from the Franck–Condon region; the path is barrierless and is therefore considered the most probable deactivation channel. In fact, 83% of excited state trajectories are expected to pass through the $^1\pi\sigma_{NH}^*/S_0$ CI. [20] Relaxation from the initially excited $^1\pi\pi^*$ state to the $^1\pi\sigma_{NH}^*/S_0$ CI is expected in 105 fs [20] – demonstrating the efficiency of this coupling with S_0. In comparison, $^1\pi\sigma^*$ mediated pathways account for up to 80% of the relaxation of the related heterocycle pyrrole – whose $^1\pi\sigma^*$ state can also be weakly excited directly because of vibronic coupling. [21] The CN-stretching ($^1\pi\sigma_{CN}^*/S_0$) CI lies only 3.2–3.9 eV above the ground state,

however it requires the largest distortion from the Franck–Condon geometry [12] and is expected in only 1% of excited state trajectories. [20] Timescales for this relaxation channel could not be calculated due to a statistically insufficient number of trajectories. The NH-puckering CI lies 5.0–5.3 eV above the ground state and is connected barrierlessly with the Franck–Condon region. [12] Calculations show that 16% of excited state trajectories relax to the NH-puckering CI within 175 fs of initial excitation. [20] As the authors in ref. 12 suggest, imidazole can either relax back to the ground state or can undergo a multitude of fragmentation processes at both the $^1\pi\sigma_{CN}^*/S_0$ and NH-puckering/S_0 CIs. However, ground state repopulation to fragmentation branching ratios are currently unavailable.

Until now, experiments have mostly focused on probing photoproducts following relaxation through the $^1\pi\sigma_{NH}^*/S_0$ CI. Ashfold and co-workers have employed total kinetic energy release (TKER) spectroscopy at various wavelengths across the excited state absorption spectrum. Between 238–220 nm, the $^1\pi\sigma_{NH}^*$ state is populated directly and deactivation results in production of fast H-atoms from N-H bond fission. [15, 22] The fast H-atom feature in the TKER spectrum peaks at ~9200 cm^{-1}. This feature remains even at their shortest excitation wavelength (193 nm) where direct $^1\pi\pi^*$ excitation dominates over the direct $^1\pi\sigma_{NH}^*$ excitation. Detection of a fast H-atom peak following 193 nm photoexcitation is taken as evidence of indirect $^1\pi\sigma_{NH}^*$ population from the optically bright $^1\pi\pi^*$ state in accordance with the calculations described above. The TKER spectra also display a low energy H-atom feature peaking near 1500 cm^{-1} whose intensity increases with the excitation energy. The authors assign this peak to statistical decay of vibrationally excited ground state imidazole. However, whilst this mechanism may be operative at long time-delays (ns), recent work by Hadden *et al*. [23] employing time-resolved velocity map ion imaging (TR-VMI) suggests that the low energy H-

atom feature is very likely multicomponent in nature, given their observation of low energy H-atoms at very short time-delays (~100 fs). In addition to statistical decay of vibrationally excited ground state imidazole operating at much longer time-delays, these authors suggest that alternative pathways must be operative at these short time-delays such as multiphoton dissociative ionization of the parent cation to generate low energy H-atoms directly.

In this work we present an experimental study of the photochemistry of gas-phase imidazole following $^1\pi\pi^*$ excitation. A combination of time-resolved ion yield (TRIY) and H-atom TKER spectroscopy has been used to probe photoproduct formation associated with the NH-stretching and ring deformation pathways to obtain a more complete picture of the excited state dynamics of imidazole. Our data are interpreted within the theoretical model described above.

3.3 Results and discussion

Upon 200 nm excitation of the $^1\pi\pi^*$ state in imidazole, three deactivation pathways have been identified by non-adiabatic dynamics simulations, [12, 20] whereby 83%, 16%, and 1% of excited state trajectories will relax along the $^1\pi\sigma^*_{NH}$, NH-puckering, and CN-stretching coordinates, respectively. [20] In general, relaxation along any of these coordinates can lead directly back to the ground state or to molecular fragments. Specifically, deactivation along the $^1\pi\sigma^*_{NH}$ state can lead to H-atom extraction [15, 23] while NH-puckering and CN-stretching pathways (referred to as ring deformation pathways) may produce larger photoproducts in subsequent fragmentation steps. [12, 26] Here, we present a comprehensive analysis of ultrafast electronic relaxation pathways in imidazole following 200 nm excitation, by monitoring the timescales for photofragment production using a combination of TRIY and TKER spectroscopies.

In sections 3.3.1 and 3.3.2, TRIY data using 251 nm and 243 nm probe pulses are analyzed in an effort to clock relaxation along ring deformation and $^1\pi\sigma^*_{NH}$ coordinates, respectively. In section IIIC we distinguish between H-atoms from $^1\pi\sigma^*_{NH}$ deactivation and alternative sources based on a bimodal H-atom energy distribution as observed in the TKER spectrum.

3.3.1 Two-color TRIY spectra—a probe of relaxation through ring deformation modes

Fig. 3.3 displays TRIY data recorded with 200 nm pump and 251 nm probe pulses, the latter of which has been purposefully selected to be below the onset of imidazole's absorption spectrum to avoid excitation from the probe pulse and unwanted probe–pump signals. The primary purpose of this data set is to investigate $^1\pi\pi^* \rightarrow$ ring deformation relaxation paths which may lead to subsequent excited state ring fragmentation or ground state repopulation. Statistical dissociation of a vibrationally hot ground state may be an alternative source of ring fragments. However, it is expected to occur on a much longer timescale than our measurement window and is not considered here**.** Mass spectra**,** recorded at two pump–probe delays ($\Delta t = 0$ fs and $\Delta t = 1000$ fs), are shown in Fig. 3.3 (a) and (b)**.** A gate around each m/z peak is integrated at all pump–probe delays to produce the delay traces in Fig. 3.3 (c). Timescales for electronic relaxation via ring deformation paths leading to specific fragments are extracted from fits to these delay traces as explained below.

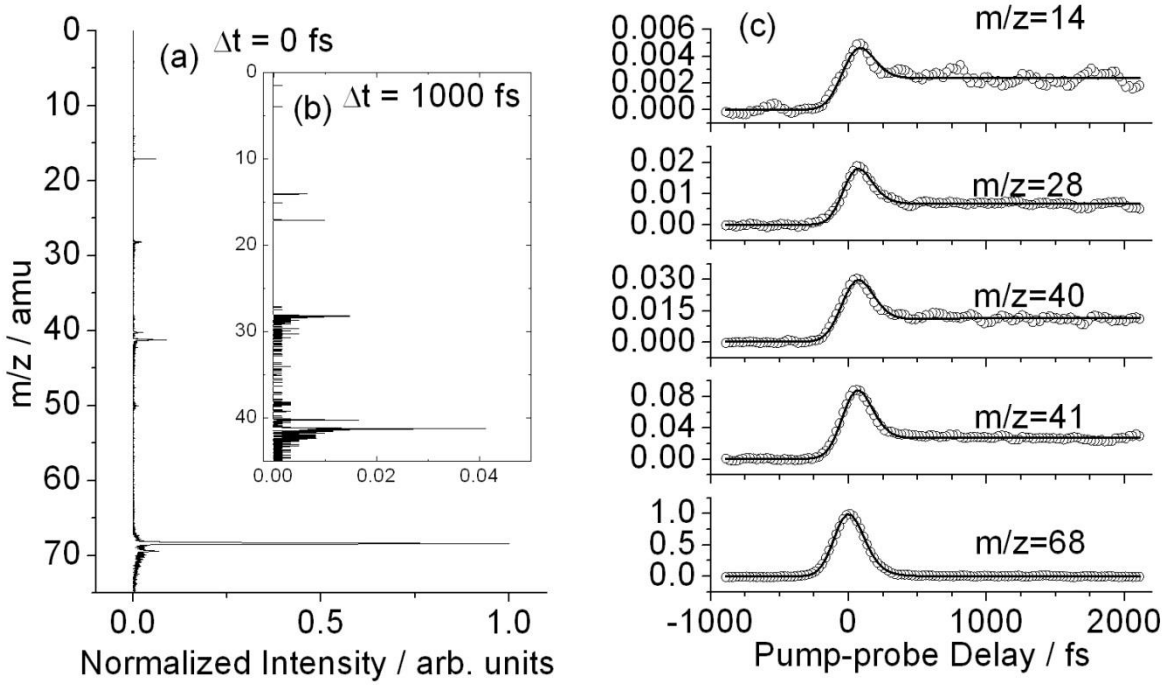

Figure 3.3 TRIY scans of imidazole recorded with a 200 nm pump and 251 nm probe. Panels (a) and (b) display mass spectra at $\Delta t = 0$ fs and $\Delta t = 1000$ fs, respectively. Transients for m/z = 14, 28, 40, 41, and 68 (top to bottom) shown in panel (c) are obtained by integrating the mass spectra at all pump-probe delays.

The mass spectrum recorded at $\Delta t = 0$ fs (Fig. 3.3 a) shows a dominant imidazole parent ion ($C_3H_4N_2^+$) at m/z = 68, major fragments at m/z = 41, 40, 28, and 14, which are assigned to $C_2H_3N^+$, $C_2H_2N^+$, CH_2N^+, CH_2^+, respectively, and minor contributions at m/z = 69 and 17. The m/z = 69 peak height is ~5% of the parent peak and is therefore attributed to the ^{13}C isotopomer. The m/z = 17 peak corresponds to residual NH_3, which is used for mass and timing calibrations.

Surprisingly absent is a peak at m/z = 67, which would correspond to the photoionized imidazolyl fragment ($C_3H_3N_2^+$) produced through N–H dissociation after relaxation along the $^1\pi\sigma_{NH}^*$ state. One may expect significant imidazolyl products since $^1\pi\sigma_{NH}^*$ relaxation is considered the major channel in imidazole, with ~83% of excited state trajectories following this path. [20] The lack of an m/z = 67 peak will be discussed further below.

Photoproduct transients are displayed for m/z = 14, 28, 40, 41, and 68 (top to bottom) in Fig. 3.3 (c). The imidazole parent (m/z = 68) trace extends slightly toward positive pump–probe delays beyond our Gaussian IRF. This trace is fit with a single exponential decay function convoluted with the IRF of fixed FWHM = 225 fs as determined by NH_3 calibration scans. The extracted decay constant, τ_D = 73 fs, [27] indicates the average lifetime, over all decay paths, of the initially excited $^1\pi\pi^*$ state. This value agrees nicely with recent time-resolved photoelectron spectroscopy (TRPES) results, [20] but underestimates the theoretical average lifetime, reported as τ_D = 117 fs. [20] According to the trajectory calculations, this average lifetime is composed of weighted time constants of 105 fs and 175 fs for relaxation along the NH-stretching (83%) and ring deformation (17%) paths, respectively. The discrepancy between experiment and theory has recently been discussed. [11, 20] Nevertheless, the experimental measurements show an overall good agreement with the current theoretical model.

The shape of the fragment (m/z = 14, 28, 40, and 41) transients differs from that of the parent ion. Following an initial peak which is similar to the parent, the fragment signals level off at a constant non-zero value. All fragment delay traces are fit with the summation of two independent functions, an exponential decay, and an exponential rise that are both convoluted with the IRF. This choice of fitting function was made in analogy to the analysis of H-atom delay traces which will be discussed below. Important fit parameters include the time constant for the exponential

decay (τ_D) and rise (τ_R). The initial peak and decay can be fit using the decay constant of the parent, τ_D = 73 fs. Imidazole remains in an electronically excited state during this time and is then easily ionized by the probe pulse. Subsequent dissociation from the ionic state, i.e. dissociative ionization, leads to cationic fragments and, consequently, these charged fragments contribute to the peak in the corresponding m/z traces during the parent excited state lifetime. Appearance energies of 11–14 eV have been reported for cationic fragments of m/z = 41, 40, and 28 [26] (which is reached by additional absorption of one or two probe photons in our experiments). The constant signal at $\Delta t \geq 500$ fs is then associated with fragmentation products resulting from the $^1\pi\pi^* \rightarrow$ ring deformation relaxation pathway in the neutral excited state. The timescale for fragmentation is characterized by the exponential rise time constant τ_R. Rise time constants are in the 107–162 (±30) fs range and are interpreted as the total $^1\pi\pi^* \rightarrow$ fragment appearance time. The mechanisms discussed above are considered the dominant pathways for the observed time-dependent fragmentation signals. Mechanisms based on multiphoton absorption of the pump are minimized (but not excluded) by our selection of low pump pulse energies. Such examples include two-photon ionization of the imidazole parent which populates its cationic ground state. The imidazole cation can either undergo dissociation directly in its ground state or excited state dissociation following absorption of one or more additional probe photons. Neutral and charged fragments are produced in both cases, but the former requires an additional probe step, i.e. multiphoton ionization of a neutral fragment, to constitute a time-dependent signal.

Important information regarding the product state distributions can be obtained through analysis of fragment signal intensities. This requires knowledge of the order of the ionization process for each mass which has been determined from a power dependency study. For this purpose, TRIY spectra were recorded under similar conditions as in Fig. 3.3 but at two additional probe pulse

energies (4.5 μJ and 11 μJ). All different fragments integrated over Δt = 1000–2000 fs recorded at 11 μJ probe energy were ~10 times stronger than those recorded at 4.5 μJ probe energy, yielding a multi-photon order of ~2.6 ($\log_{11/4.5}10$). We therefore conclude that the fragmentation signals recorded at low probe power (3 μJ and 4.5 μJ) are a result of two-photon ionization, and a probe pulse as strong as 11 μJ may lead to contributions from three photon ionization. This is further supported by the absence of a HCN fragment signal (ionization potential IP = 13.6 eV [28]) in Fig. 2b, that would require three-photon ionization. The exact molecular structures of the observed fragments are unknown but typical ionization energies around 9–12 eV and lowest excited state energies around 0.5–4.5 eV have been reported for possible photoproducts CH_2, [29 – 31] CH_2N, [32 – 34] C_2H_2N, [35] C_2H_3N. [35] Initial 200 nm excitation deposits 6.2 eV into the parent molecule which then has to undergo dissociation of two ring bonds to produce the observed fragments. Photoproducts share a few eV of internal and translational energy between the co-fragments which are consequently left in the vibrationally hot ground electronic state or possibly in the lowest excited state, depending on their electronic excited state energies. Subsequently, they are two-photon ionized by the 251 nm probe (9.8 eV). This picture is consistent with photoproduct distributions of UV dissociated pyrrole by Lee and co-workers, [36] who reported dissociation energies for ring opened bi-radical photoproducts (C_3H_4) of 2.8 and 3.5 eV, and HCN with either vinyl methylene or cyclopropene cofragments of 5.3 and 3.5 eV, respectively.

Mass spectra and time traces in Fig. 3.3 have been normalized to the m/z = 68 maximum signal intensity. The ratios of fragment signals at Δt = 1000 fs to parent signal at Δt = 0 fs are listed in Table 3.1 (I_F/I_P) and describe the relative yields of individual fragments. These values do not provide a measure of total fragmentation branching ratios during excited state relaxation due to

one- versus two-photon ionization of parent and fragments, respectively; however, the relative ratios among different fragmentation channels can be extracted since all fragments undergo two-photon ionization. Based on the observation of the m/z = 41 co-fragment, HCN elimination is a dominant process during imidazole ring fragmentation similar to the pyrrole study of Blank *et al*. [36] The absence of an m/z = 67 peak could be due to many reasons. One of these is a low cross-section for two-photon ionization. Alternatively, the vertical ionization potential may be energetically too high to be reached in a two-photon ionization process and may require three-photons. After NH-bond dissociation which requires 4.2 eV [37] and generation of an H-atom photoproduct with kinetic energy, imidazolyl is left in its ground electronic state, as predicted by Devine *et al*. [15] The internal energy imparted to the imidazolyl radical is less than that available to access the first excited electronic state, which has been calculated to be approximately 0.7 eV. [38] The vertical ionization potential of imidazolyl is unknown, but Van den Brom *et al*. have estimated the IP of pyrrolyl to be around 9 eV. The IP of imidazole is slightly higher than for pyrrole. In analogy we expect vertical ionization of the imidazolyl in the 9–11 eV range, i.e. comparable to or higher than pyrolyl. [39]

Table 3.1 Fit parameters for the fragments shown in Fig. 3.3. I_F/I_P is the ratio of fragment signal intensity (at $\Delta t = 1000$ fs) to parent signal intensity (at $\Delta t = 0$ fs). All time constants are reported with a ± 30 fs error

m/z (amu)	τ_R (fs)	I_F/I_P
41	156	0.028
40	162	0.011
28	107	0.007
14	117	0.002

3.3.2 Two-color TRIY spectra—a probe of relaxation through the $^1\pi\sigma_{NH}^*$ state

Here, the $^1\pi\sigma_{NH}^*$ mediated relaxation channel is studied through analysis of H-atom and imidazolyl photoproduct yields. TRIY data were recorded with 200 nm pump and 243 nm probe pulses, and are presented in Fig. 3.4. Again the mass spectra at $\Delta t = 0$ and $\Delta t = 1000$ fs are displayed and time traces for m/z = 1 and m/z = 67 are presented. Previous results [15] have shown that N–H dissociation following $^1\pi\sigma_{NH}^*$ state relaxation yields imidazolyl and H-atoms in their ground electronic state – both of which require multiphoton ionization. A high-power 243 nm probe was selected primarily to ionize photodissociated H-atoms through 2 + 1 REMPI of the Lyman-α transition but has the added advantage of increasing the multiphoton ionization signal

of imidazolyl.

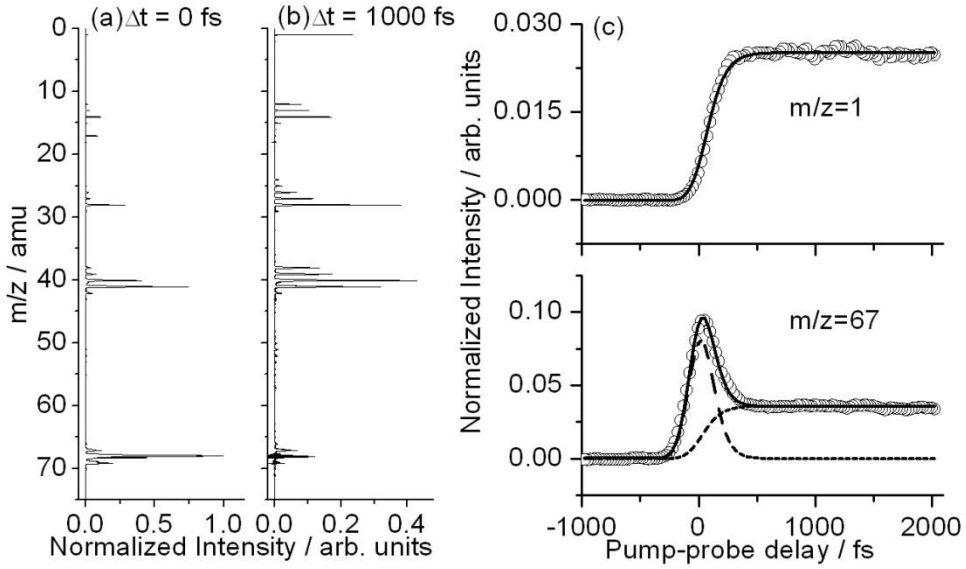

Figure 3.4 TRIY scans of imidazole recorded with a 200 nm pump and 243 nm probe. Panels (a) and (b) display mass spectra at $\Delta t = 0$ fs and $\Delta t = 1000$ fs, respectively. Transients for m/z = 1, 67 (top to bottom) shown in panel (c) are obtained by integrating the mass spectra at all pump-probe delays.

Peaks at m/z = 1 and 67 are evident in Fig. 3.4 along with a noticeably enhanced fragmentation pattern. Again, the main fragment peaks (m/z = 14, 28, 40, and 41) appear but with a trail of smaller peaks differing by one mass unit. Here, the fragmentation pattern arises from higher

order multi-photon ionization caused by the higher probe laser intensity, which is verified by the observation of the HCN (m/z = 27) fragment peak which is absent in Fig. 3.3 (b), indicating at least three-photon ionization. A separate experiment, with a low power 243 nm probe, reveals the same fragmentation dynamics as the 251 nm scans. Therefore, the fragmentation dynamics extracted in section 3.3.1 can be more strongly associated with two photon ionization of ground state photoproducts.

Timescales for $^1\pi\sigma_{NH}^*$ relaxation are extracted through analysis of the m/z = 1 and 67 transients. The H-atom (m/z = 1) time trace consists of a single step function that lacks the initial peak observed at other masses. It is therefore fit by a single exponential rise convoluted with the IRF. A rise constant of τ_R = 94 (±30) fs is extracted. These dynamics are associated with excited state flux from the $^1\pi\pi^*$ state that crosses onto the $^1\pi\sigma_{NH}^*$ surface and undergoes N–H dissociation. At this point it should be noted that TRIY measures the total H-atom yield and as such does not provide any means to distinguish between various other sources that may contribute to the overall H-atom signal. This issue is resolved by the experiments described in section 3.4. Due to the dominance of $^1\pi\sigma_{NH}^*$ mediated deactivation in imidazole, TRIY provides a good approximation for the time scales of excited state H-atom elimination and a valuable comparison with the TRIY time trace of its cofragment imidazolyl.

H-atom elimination naturally leads to formation of the associated imidazolyl product. Imidazolyl and H-atoms both originate from relaxation along the $^1\pi\sigma_{NH}^*$ pathway, and should therefore have identical appearance dynamics. However, m/z = 67 displays a peak near Δt = 0 fs similar to the other fragments, and is fit with the sum of exponential decay and rise functions convoluted with the IRF. Individual contributions from the decay and rise components are indicated as dashed and dotted lines, respectively, in Fig. 3.4 (c). Again, we attribute this peak to dissociative

ionization of the monomer, and describe it with a decay constant fixed to the monomer decay, τ_D = 73 fs. The exponential rise is then associated with N-H dissociation following $^1\pi\sigma_{NH}$* relaxation. We have chosen to fix τ_R = 94 fs as determined from the H-atom trace and find that these values nicely describe the m/z = 67 trace within our error of ±30 fs.

3.4 H-atom TKER spectra

The lifetime for H-atom dissociation obtained by TRIY and reported in section 3.3.2 is considered an average over all H-atom emission processes. However, it is known [15, 23] that H-atom emission from imidazole follows a bi-modal energy distribution. Here, we probe photodissociated H-atoms through 2 + 1 REMPI and energy analyze in an effort to extract timescales for relaxation paths leading to each H-atom energy range.

In Fig. 3.5 (a) we present the H-atom TKER spectrum obtained by integrating over the time window $\Delta\mathbf{t}$ = 1000–2000 fs. A bi-modal distribution is clearly evident whereby a sharp low-energy peak is centered near 1200 cm^{-1} and a broader high-energy feature is centered near 8000 cm^{-1}. The $^1\pi\sigma$* mediated N–H bond cleavage will yield 8000–9500 cm^{-1} kinetic energy H-atoms, [23] and we therefore assign the high-energy (fast) feature to this mechanism. Two possible assignments for the low-energy (slow) feature can be found in the literature. Statistical unimolecular decay of the vibrationally hot ground state has been identified in the TKER experiments of Ashfold, [15] while TR-VMI measurements have led Hadden *et al*. [23] to identify multiphoton dissociative ionization as the more likely candidate for the low-energy H-atoms within the time window of their experiments (100 ps). Our experiment does not afford new information about the source of slow H-atoms.

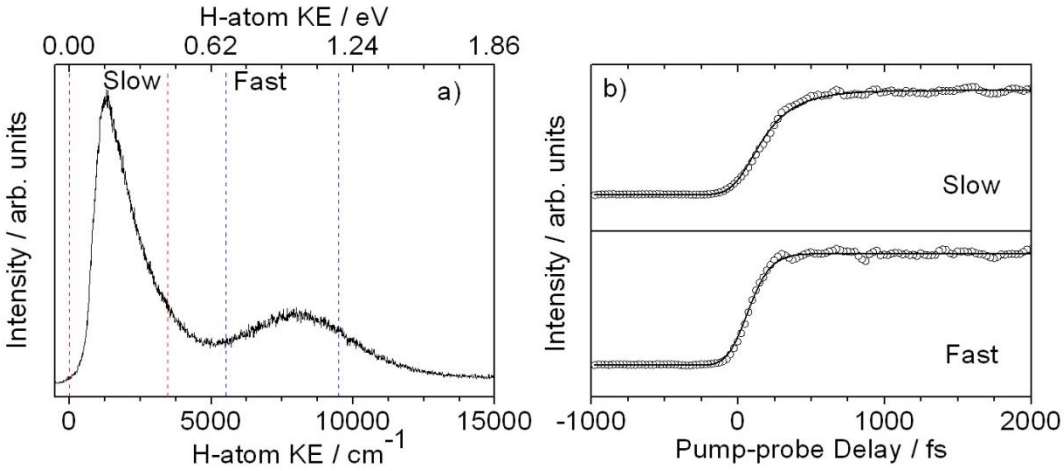

Figure 3.5 TKER spectrum of imidazole recorded at 200 nm pump and 243 nm probe. Transient H^+ signal is shown in (b) for the slow and fast H-atoms, which are integrated between the red and blue dashed lines in (a), respectively. The height of the high and low KE H-peaks does not reflect the actual ratio of the competing pathways since the collection efficiency of the magnetic bottle varies at different kinetic energies.

Photodissociation dynamics are determined from fits to the transient profiles presented in Fig. 3.5 (b). These profiles are obtained by energy integrating peaks in the TKER spectrum at all pump–probe delays. Integration ranges are 0–3500 cm^{-1} and 5500–9500 cm^{-1} for low- and high-energy H-atoms, respectively, as indicated in Fig. 3.5 (a). Also, the total H-atom transient is obtained, by integrating over all H-atom energies but is not shown in Fig. 3.5. All delay traces

display zero intensity at negative pump–probe delays followed by a single step which rises near Δt = 0 fs and plateaus after a few hundred fs. An exponential rise convoluted with the Gaussian IRF is then well suited to fit these transients. In all the delay traces, the IRF is constrained to 225 fs as obtained from NH_3 calibration. Fit parameters τ_R are extracted and are taken as the H-atom appearance times. Rise constants, τ_R = 199, 82 and 104 fs (±30) for slow, fast and all H-atoms respectively, are extracted from the fits to their corresponding delay traces and are listed in Table 3.2. The 104 fs appearance time from total H-atom trace agrees within our error with the 94 fs appearance time obtained from TRIY data in section 3.3.2. Total dissociation times of slow and fast H-atoms are in excellent agreement with the TR-VMI result by Hadden *et al*. [23] The 82 fs appearance time of the high kinetic energy H-atoms is also in-line with the theoretical 105 fs relaxation time of the NH-stretching path. [20]

Table 3.2 Fit parameters for H-atoms of different kinetic energy ranges. All time constants are reported with a ±30 fs error

	Integration range (cm^{-1})	τ_R (fs)
Low KE	0–3500	199
High KE	5500–9500	82
All KE	0–42500	104

3.5 Conclusions

The UV photophysics of imidazole are studied experimentally. TRIY spectra and TKER spectra are analyzed based on ab initio calculations and dynamics simulations. 200 nm excitation to the $^1\pi\pi^*$ state is investigated.

The following photophysical model is proposed through analysis of the experimental data and shown in Fig. 3.6: after excitation to the $^1\pi\pi^*$ state, several deactivation pathways are active. The $^1\pi\sigma^*$ pathway associated with the NH-stretching coordinate is the most dominant and fastest channel with a lifetime of around 82 fs. Ring puckering and CN-stretching only play a minor role in the $^1\pi\pi^*$ depopulation. Both the $^1\pi\sigma^*$ and ring deformation pathways lead to photofragmentation products that are characterized experimentally using time-resolved mass spectrometry. H-atoms, probed at 243 nm through (2 + 1) resonant multiphoton ionization, show a 94 ± 30 fs rise time following initial excitation. Larger fragments, including $C_2H_3N^+$, $C_2H_2N^+$, CH_2N^+, CH_2^+, observed in the time-resolved mass spectra are believed to be associated with the ring puckering and ring opening mechanism, and rise in 107–162 fs. Directly related to this increase in appearance time is the overall minor role that this channel plays. Dynamical processes of imidazole in the time-window of our experiment, i.e., −1000–2000 fs, are all completed on timescales close to the timing resolution of the experiment. Appearance times of the photoproducts from the NH-stretching and ring deformation pathways can roughly be placed at 82 ± 30 fs and 107–162 ± 30 fs, respectively, which are of comparable magnitude to the theoretical relaxation times of 105 fs and 175 fs.

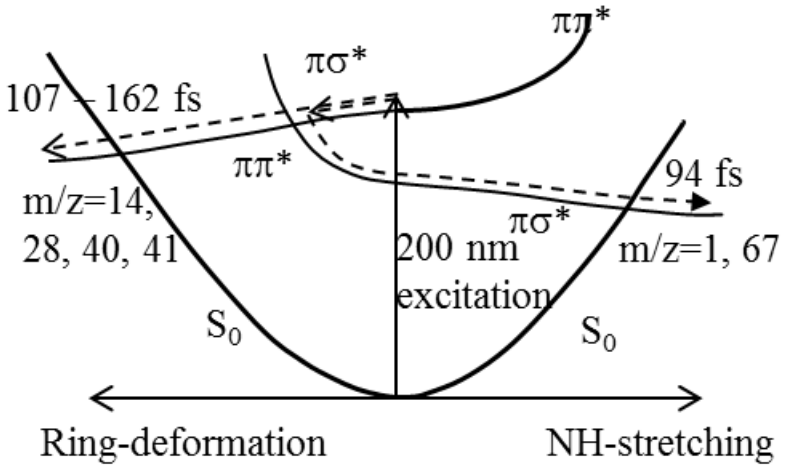

Figure 3.6 Schematic picture of the dynamics involved.

3.6 References

[1] C. E. Crespo-Hernandez, B. Cohen, P. M. Hare and B. Kohler, *Chem. Rev.*, 2004, **104**, 1977.

[2] K. L. Wells, G. M. Roberts and V. G. Stavros, *Chem. Phys. Lett.*, 2007, **446**, 20.

[3] C. Z. Bisgaard, H. Satzger, S. Ullrich and A. Stolow, *ChemPhysChem*, 2009, **10**, 101.

[4] K. L. Wells, D. J. Hadden, M. G. D. Nix and V. G. Stavros, *J. Phys. Chem. Lett.*, 2010, **1**, 993.

[5] N. L. Evans and S. Ullrich, *J. Phys. Chem. A*, 2010, **114**, 11225.

[6] A. Broo, *J. Phys. Chem. A*, 1998, **102**, 526.

[7] A. L. Sobolewski and W. Domcke, *Eur. Phys. J. D*, 2002, **20**, 369.

[8] S. Ullrich, T. Schultz, M. Z. Zgierski and A. Stolow, *Phys. Chem. Chem. Phys.*, 2004, **6**, 2796.

[9] M. N. R. Ashfold, B. Cronin, A. L. Devine, R. N. Dixon and M. G. D. Nix, *Science*, 2006, **312**, 1637.

[10] M. N. R. Ashfold, G. A. King, D. Murdock, M. G. D. Nix, T. A. A. Oliver and A. G. Sage, *Phys. Chem. Chem. Phys.*, 2010, **12**, 1218.

[11] M. Barbatti and S. Ullrich, *Phys. Chem. Chem. Phys.*, 2011, **13**, 15492.

[12] M. Barbatti, H. Lischka, S. Salzmann and C. M. Marian, *J. Chem. Phys.*, 2009, **130**, 03430.

[13] S. Cradock, R. H. Findlay and M. H. Palmer, *Tetrahedron*, 1973, **29**, 2173.

[14] L. Klasinc, B. Ruščič, F. Kajfež and V. Šunjić, *Int. J. Quantum Chem.*, 1978, **14**, 367.

[15] A. L. Devine, B. Cronin, M. G. D. Nix and M. N. R. Ashfold, *J. Chem. Phys.*, 2006, **125**, 184302.

[16] F. B. C. Machado and E. R. Davidson, *J. Chem. Phys.*, 1992, **97**, 1881.

[17] L. Serrano-Andres, M. P. Fulscher, B. O. Roos and M. Merchan, *J. Phys. Chem.*, 1996, **100**, 6484.

[18] A. A. Jarzecki and T. G. Spiro, *J. Raman Spectrosc.*, 2001, **32**, 599.

[19] B. G. Ramsey, *J. Org. Chem.*, 1979, **44**, 2093.

[20] R. Crespo-Otero, M. Barbatti, H. Yu, N. L. Evans and S. Ullrich, *Chem. Phys. Chem.*, 2011, **17**, 3365.

[21] M. Vazdar, M. Eckert-Maksić, M. Barbatti and H. Lischka, *Mol. Phys.*, 2009, **107**, 845.

[22] M. G. D. Nix, A. L. Devine, B. Cronin, R. N. Dixon and M. N. R. Ashfold, *J. Chem. Phys.*, 2006, **125**, 133318.

[23] D. J. Hadden, K. L. Wells, G. M. Roberts, L. T. Bergendahl, M. J. Paterson and V. G. Stavros, *Phys. Chem. Chem. Phys.*, 2011, **13**, 10342.

[24] C. A. Williams, G. M. Roberts, H. Yu, N. L. Evans, S. Ullrich and V. G. Stavros, *J. Phys. Chem. A,* 2012, 116, 2600.

[25] P. Kruit and F. H. Read, *J. Phys. E: Sci. Instrum.*, 1983, **16**, 313.

[26] M. Schwell, H. Jochims, H. Baumgartel and S. Leach, *Chem. Phys.*, 2008, **353**, 145.

[27] It is possible to extract time constants that are much faster than the instrument response function. Representative examples of this can be found in *Faraday Discuss.*, 2004, **127**, 193 and *Phys. Chem. Chem. Phys.*, 2010, **12**, 7988. Our measurements suggest that we are able to extract time constants that are approximately 30% of our IRF.

[28] D. W. Turner, C. Baker, A. D. Baker and C. R. Brundle, *MolecularPhotoelectron Spectroscopy,* Wiley, New York, 1970, p. 345.

[29] K.-C. Lau and C. Y. Ng, *J. Chem. Phys.*, 2005, **122**, 224310.

[30] P. Jensen and P. R. Bunker, *J. Chem. Phys.*, 1988, **89**, 1327.

[31] P. M. Zimmerman, J. Toulouse, Z. Zhang, C. B. Musgrave and C. J. Umrigar, *J. Chem. Phys.*, 2009, **131**, 124103.

[32] F. L. Nesbitt, G. Marston, L. J. Stief, M. A. Wickramaaratchi, W. Tao and R. B. Klemm, *J. Phys. Chem.*, 1991, **95**, 7613.

[33] G. F. Adams, D. R. Yarkony, R. J. Bartlett and G. D. Purvis, *Int. J. Quantum Chem.*, 1983, **23**, 437.

[34] N. R. Brinkmann, S. S. Wesolowski and H. F. Schaefer III, *J. Chem. Phys.*, 2001, **114**, 3055.

[35] R. P. Thorn Jr., P. S. Monks, L. J. Stief, S. C. Kuo, Z. Zhang, S. K. Ross and R. B. Klemm, *J. Phys. Chem. A,* 1998, **102**, 846.

[36] D. A. Blank, S. W. North and Y. T. Lee, *Chem. Phys.*, 1994, **187**, 35.

[37] G. da Silva, E. E. Moore and J. W. Bozzelli, *J. Phys. Chem. A*, 2006, **110**, 13979.

[38] J. M. Bofill, S. Olivella and A. Sole, *J. Am. Chem. Soc.*, 1989, **111**, 7740.

[39] A. J. van den Brom, M. Kapelios, T. N. Kitsopoulos, N. H. Nahler, B. Cronin and M. N. R. Ashfold, *Phys. Chem. Chem. Phys.*, 2005, **7**, 892.

CHAPTER 4

ULTRAFAST DYNAMICS OF UV-EXCITED IMIDAZOLE

4.1 Introduction

Trajectory-based nonadiabatic dynamics simulations are currently one of the frontiers of computational chemistry. These simulations demand a delicate combination of high-quality and high-speed methods to achieve a proper description of the excited-state time evolution of molecules (for a recent review, see Ref. [1]). Although the basis for these dynamical simulations was set early in the 1970s, [2, 3] only in the last fifteen years, [4-8] with the development of computational capabilities and efficient quantum chemical methods, have they become a routine tool for research in photochemistry and photophysics. [9-11]

Much of the research in nonadiabatic dynamics simulations has focused on the relaxation processes following photoexcitation of organic molecules. [1, 12, 13] These simulations have provided a mechanistic view of ultrafast processes by determining the relative importance and time constants for each available reaction pathway. Additionally, nonadiabatic dynamics simulations can help in the interpretation of femtosecond (fs) spectroscopic data, which often need theoretical insights to be deconvoluted. [14]

In this work, we turn our attention to the dynamics of imidazole ($C_3H_4N_2$) in the gas phase. Imidazole is the chromophore of important biological compounds such as histidine and

histamine, both nonfluorescent species. [15] It is one of the chromophores of urocanic acid, one of the main UV absorbers in the skin of mammals. [16, 17] Moreover, it has also been reported that deformation of the imidazole ring may be connected to internal conversion in the purine-derived DNA bases excited in the UV-C spectral region. [18, 19]

As with the closely related heterocycles pyrrole (C_4H_5N) [20-24] and furan (C_4H_4O), [25] UV-excited imidazole is known to return to the ground state by internal conversion. [26] Four conical intersections between the first excited and ground states have been previously described for imidazole. [27] In structural terms, they are characterized by NH dissociation, CN dissociation, N puckering, and NH puckering. [27] In particular, the NH- and CN-dissociation conical intersections are connected by the same branch of crossing seam. [27] Here, we combine theoretical nonadiabatic dynamics simulations and experimental time-resolved photoelectron spectroscopy (TRPES), both in the gas phase, to discuss how each conical intersection contributes to the internal conversion, depending on the initial excitation energy.

One- and two-color photoelectron spectra were recorded experimentally by using a UV fs laser system and magnetic-bottle-type photoelectron spectrometer. The one-color spectra span wavelengths between 265.7 nm (4.67 eV) and 200.8 nm (6.18 eV). The two-color time-resolved spectra were recorded for two distinct pump wavelengths: 239.6 nm (5.17 eV), corresponding to direct excitation of the dark $^1\pi\sigma^*_{NH}$ singlet state, and 200.8 nm (6.18 eV), corresponding to excitation of the bright $^1\pi\pi^*$ singlet state. The dynamics simulations were tuned to investigate imidazole within similar excitation windows. Excitation into the low-energy region (named window A) was achieved by restricting the initial excitation energy to lie between 5.0 and 5.2

eV. Excitation into the high-energy region (named window B) was achieved by restricting the initial excitation energy to lie between 6.0 and 6.2 eV.

Trajectory-based nonadiabatic dynamics simulations are computationally expensive, and one must always observe the trade-off between computational speed and quantum-chemical quality to select the appropriate method for each case. The method we chose for this work is time-dependent density functional theory (TDDFT). Although computationally efficient, TDDFT has important handicaps, which may lead to qualitatively wrong results. [28] Conventional functionals are known to produce a bad description of dispersion interactions, [29] as well as of doubly excited, [30] charge-transfer, [31] and multireference [32] states. In particular, it has been shown that the lack of double excitations in linear-response TDDFT leads to wrong dimensionality of the intersection space. [30] While some of these problems (dispersion, charge-transfer states) can be attenuated by a proper choice of functionals, others (double excitation, multireference states) depend on new formulations of excited-state computations beyond linear-response TDDFT. [33] Altogether, this means that TDDFT may not work well to describe the excited-state dynamics of some molecules and that excited-state dynamics with TDDFT must always be preceded by an extensive check of the potential-energy surfaces. In the case of imidazole, the validity of TDDFT for studying its excited-state dynamics has been assured by the good comparison between TDDFT and ab initio multireference configuration interaction (MRCI) dynamics performed for pyrrole [23, 34]and by comparative investigation of reaction pathways of imidazole computed with different methods, presented here and in reference [27]. However, as we shall discuss below, the TDDFT method proved to be inadequate for investigating crossing to the ground state, which is quite an important restriction.

Computational studies of ultrafast processes, including nonadiabatic dynamics simulations, are often restricted to description of the ground and excited states of the photoactivated molecules. On the other hand, experimental measurements of these same processes are often obtained with pump–probe setups, whereby the probe laser often produces photoions. Thus, for proper comparison to experimental data, theory should also account for the cationic states of the investigated molecule. [35-37] In the present work, not only the electronic states of neutral imidazole, but also those of the imidazole cation, were investigated along the main reaction pathways. Additionally, a simple procedure to simulate photoelectron spectra based on computation of ionization potentials (IP) for geometries obtained during the dynamics simulations was developed. This technique allows assignment of contributions from different cationic states to several bands in the experimentally measured spectrum. (Theoretical calculations were performed by the Barbatti group.) [38]

4.2 Experimental Results

4.2.1 One-Color Photoelectron Spectra

One-color UV photoelectron spectra of imidazole were recorded at wavelengths of 200.8 (Figure 4.1 a), 241.6 (Figure 4.1 b), 253.9 (Figure 4.1 c), and 265.7 nm (Figure 4.1 d) by using a two-photon (1+1) ionization scheme. Photoelectron spectra are plotted in terms of electron binding energy (BE), which is computed as the difference between the total photon energy and the measured photoelectron kinetic energy. The first and the second ionization potentials (IP_1=8.81 and IP_2=10.38 eV according to Ref. 39) are indicated in the figure, too. The cutoff of the photoelectron spectra at different electron binding energies is a result of the different total photon

energies for each respective wavelength. Here, the ionization wavelength is varied to probe different regions of the imidazole absorption spectrum.

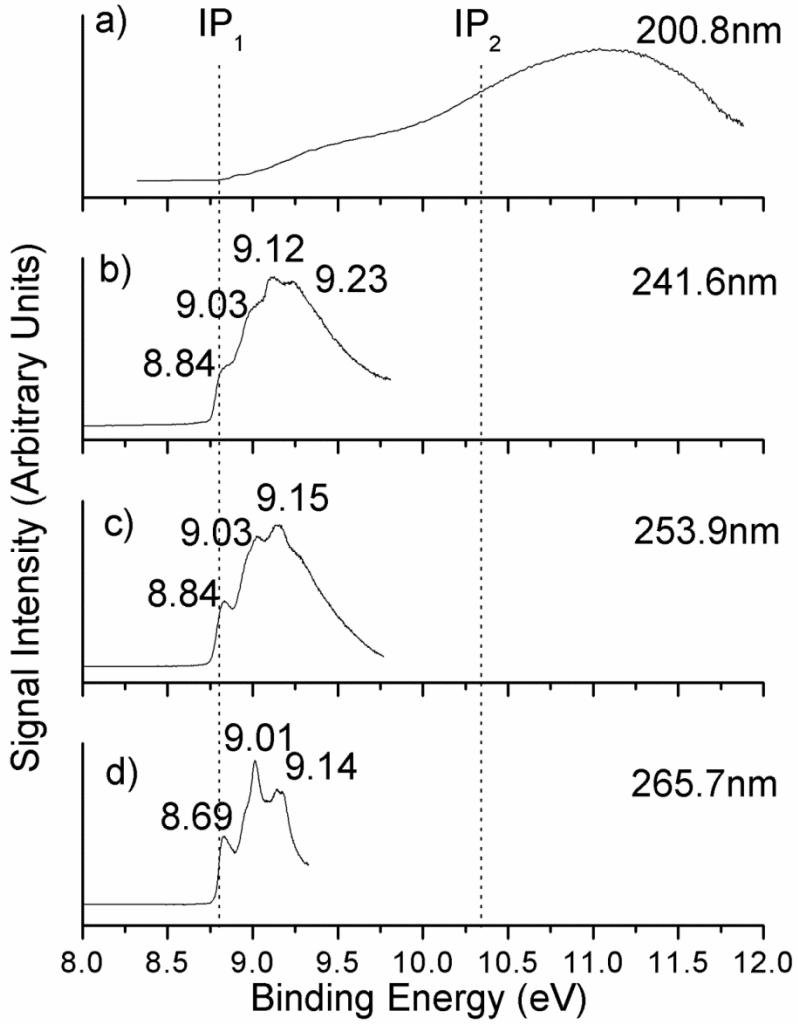

Figure 4.1 Photoelectron spectra of imidazole from one-color, two-photon (1+1) ionization at various wavelengths. Vertical dashed lines indicate IP_1 (8.81 eV) and IP_2 (10.38 eV) [39] energies required for vertical ionization into D_0 and D_1 cationic states, respectively. Vibrational structure on the D_0 cation, with 0.18 eV spacing, is also indicated (b–d).

At 265.7 (4.67 eV; Figure 4.1 d) and 253.9 nm (4.88 eV; Figure 4.1 c), the one-photon energies are below the onset of the imidazole absorption spectrum, [40] and the photoelectron spectra show nonresonant two-photon ionization into the ground state of the cation. Vibrational structure is observed with an energetic spacing of 0.18 eV that is consistent with cationic in-plane skeletal stretching modes observed by He(I) photoelectron spectroscopy. [39, 41] The long-wavelength tail of the imidazole absorption spectrum shows a slow onset around 244 nm (5.08 eV), which has been attributed to the very weak $\sigma^*_{NH} \leftarrow \pi$ transition. The photoelectron spectrum recorded at 241.6 nm (5.13 eV; Figure 4.1 b) still displays the same vibrational structure as observed for longer excitation wavelengths, but peaks show increased broadening as a result of excitation into the repulsive $^1\pi\sigma^*_{NH}$ state. The observed changes are subtle, since the intensity of the $\sigma^*_{NH} \leftarrow \pi$ transition is very low. At 200.8 nm (6.18 eV), the one-photon excitation energy is above the $^1\pi\sigma^*_{NH}$ state and in the middle of the lowest $^1\pi\pi^*$ band. Overall, the photoelectron spectrum at 200.8 nm (Figure 4.1 a) is broad and structureless due to the accessibility of various ultrafast excited-state relaxation pathways, which are explored further in this article.

4.2.2 Two-Color Time-Resolved Photoelectron Spectra

Two-color time-resolved photoelectron spectra (TRPES) were recorded for two different excitation windows and are displayed in Figure 4.2. The top and bottom panels in Figure 4.2 correspond to excitation into windows A and B, respectively. The TRPES are presented in Figure 4.2 b) and Figure 4.2 f). Two-color photoelectron binding energy spectra obtained from time integration of the TRPES data are given in Figure 4.2 a) and Figure 4.2 e). Horizontal dashed lines indicate regions (B_0 and B_1) corresponding to ionization into D_0 and D_1 cations at the beginning of the dynamics. Below, we discuss how multiple cationic states contribute to the

photoelectron yield in region B_1. The TRPES were integrated over each of these regions at all pump–probe delays, and the transient profiles are shown in Figure 4.2 c), d), g), and h). Timescales for ultrafast electronic relaxation were extracted from fits (solid lines) of these transients as described below.

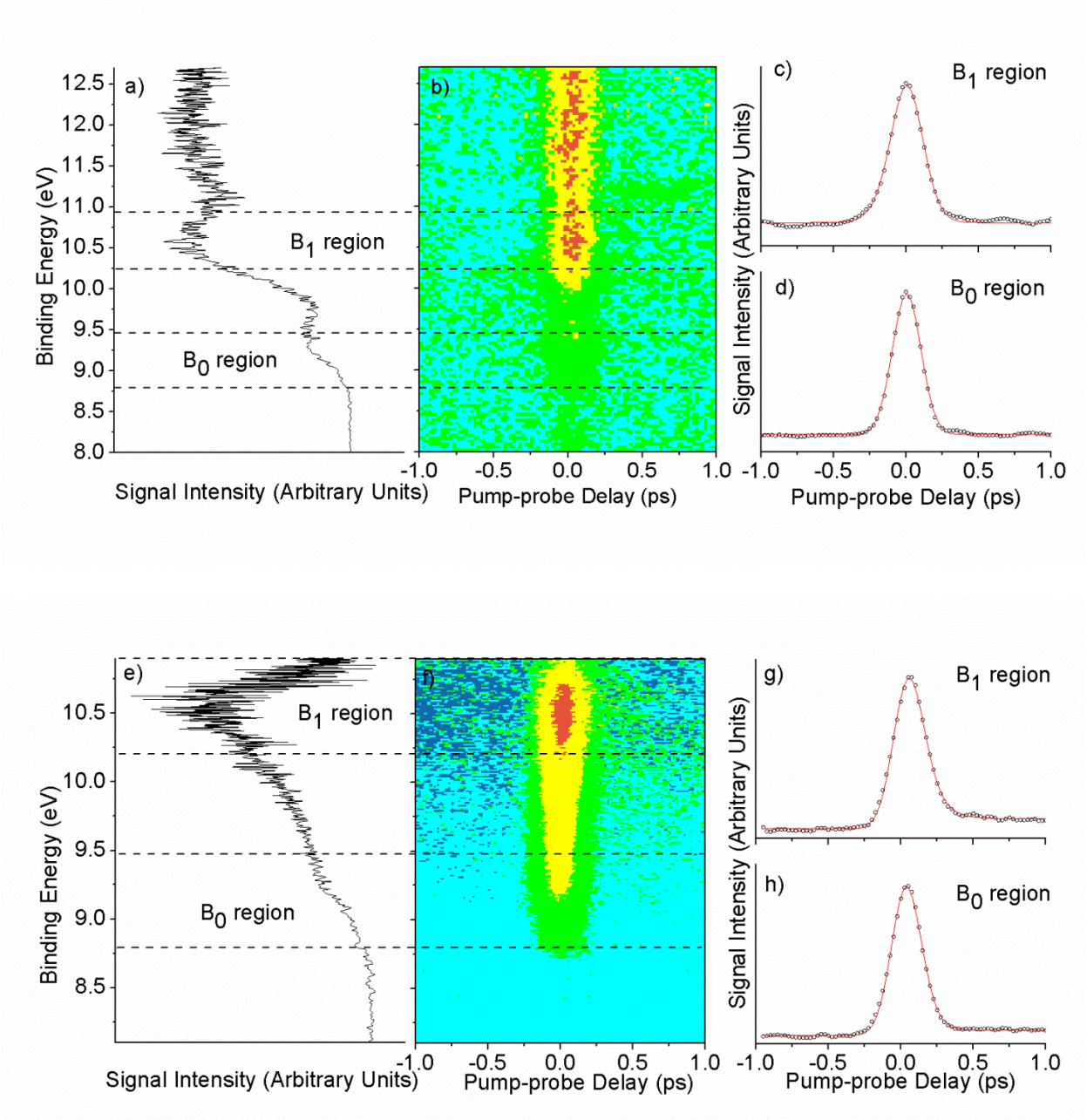

Figure 4.2 Time-resolved photoelectron spectra of imidazole recorded for direct excitation into

$^1\pi\sigma^*_{NH}$ (top) or $^1\pi\pi^*$ (bottom) states. Two-dimensional data are presented (b and f). Integrated electron binding energy spectra are shown (a and e). The B_0 and B_1 regions discussed in the text are indicated by dashed lines. Transient time traces (c, d, g, and h) and fits (solid lines) are used to extract excited-state relaxation dynamics (see text).

In window A (Figure 4.2, top), the $^1\pi\sigma^*_{NH}$ state is directly excited with a 239.6 nm pump. Dynamical evolution of this state is probed, through two-photon ionization, by a time-delayed 266.1 nm pulse. In window B (Figure 4.2, bottom), the $^1\pi\pi^*$ state is directly excited with a 200.8 nm pump and is probed by one-photon ionization at 251.6 nm. These probe wavelengths are energetically below the onset of the absorption spectrum of imidazole and are therefore nonresonant with any low-lying excited states. This pump–probe scheme was adopted to allow direct analysis of $^1\pi\sigma^*_{NH}$ (window A) and $^1\pi\pi^*$ (window B) excitation without interference from probe-induced excitation. The total photon energies in windows A and B are 14.5 and 11.1 eV, respectively. Ionization into both D_0 (IP_1=8.81 eV) and D_1 (IP_2=10.38 eV) is therefore accessible in both excitation windows. [39] Peaks in the integrated photoelectron spectra (Figure 4.2 a and Figure 4.2 e) are evidence of ionization into both cationic states.

Fits to the photoelectron transients (Figure 4.2 c, d, g, h) were utilized to extract timescales for relaxation processes in imidazole. The fitting procedure is described here and relevant fit parameters are compiled in Table 4.1. In the case of window A (Figure 4.2 c and Figure 4.2 d), both transients show a Gaussian-like shape which is noticeably wider in the B_1 region. These transients were fitted with a forward and reverse exponential decay convoluted with the Gaussian instrument response function (IRF). The IRF was taken with a fixed width of 225 fs, as determined from instrument calibration, for all fits in both excitation windows. Only relaxation

along the $^1\pi\sigma^*_{NH}/S_0$ conical intersection is active in excitation window A. Thus, we assign the decay constant τ_D for the forward (positive pump–probe delay) exponential decay as the lifetime of the $^1\pi\sigma^*_{NH}$ state. The origin of the exponential decay toward negative pump–probe delays is currently unknown but may be due to multi-photon, 266 nm excitation of high-lying Rydberg states. In window B (Figure 4.2 g and h), a similar time profile is present but with a positive baseline offset at long pump–probe delays ($\Delta t \geq 500$ fs). Transients in window B can then be fit by summation of a single exponential decay and an exponential rise, both convoluted with the Gaussian IRF. The decay constant is assigned as the lifetime of the $^1\pi\pi^*$ state, including all possible subsequent relaxation pathways. The exponential step is attributed to ionization of fragmentation products, commensurate with a $^1\pi\pi^* \rightarrow$ ring deformation$\rightarrow$fragmentation pathway proposed by theory.

Table 4.1 Decay constants τ_D [fs] obtained from fits of experimental TRPES as described in the text. Estimated errors are ±15 and ±30 fs for windows A and B, respectively.

	B_0	B_1
window A	17	44
window B	50	74

4.3 Theoretical Results (Theoretical calculations were performed by the Barbatti group.) [38]

4.3.1 Vertical Excitations and Ionization Potentials

Vertical excitation energies, obtained from all considered levels of theory, are given in the Supporting Information. Table 4.2 reports selected results for the TZVP+mod basis set together with the root mean square deviation (RMSD) between the present theoretical results and the experimental results of Devine et al. [40] using the fitted values reported in reference. [27]

Table 4.2 Vertical excitation energies ΔE [eV] and oscillator strengths f calculated with the TZVP+mod basis set. a and w are the area and the width of the experimental absorption bands, respectively. Root mean square deviation (RMSD) for the theoretical values with respect to experimental values.

	B3LYP		PBE0		BHLYP		Exptl [39]	
	ΔE	f	ΔE	f	ΔE	f	ΔE	a/w
1.	[a] Estimated experimental vertical excitation energy. [27]							
$^1\pi\sigma^*_{NH}$	5.22	0.000	5.51	0.000	5.65	0.000	–	–
$^1\pi\sigma_{CH}$*	6.09	0.027	6.36	0.028	6.47	0.031	6.26	0.01/0.04
$^1\pi\pi$*	6.23	0.119	6.40	0.145	6.49	0.167	6.08 (6.25)	0.10/0.26
$^1\pi\sigma_{CH}$*	6.32	0.000	6.58	0.003	6.73	0.000	–	–
$^1n\sigma^*_{NH}$	6.36	0.047	6.74	0.030	7.18	0.047	6.40	0.03/0.06
$^1n\pi$*	6.41	0.003	6.60	0.001	7.06	0.007	–	–
$^1\pi\sigma^*_{NH}$	6.60	0.002	6.92	0.001	7.18	0.000	–	–
RMSD	0.13	–	0.28	–	0.52	–	–	–

In contrast to the results obtained for pyrrole, [23] the B3LYP functional is in better agreement with experimental values than the PBE0 functional. The functional with the largest fraction of Hartree–Fock (HF) exchange contribution (BHLYP) provides the worst results. The

B3LYP/TZVP+mod level of theory offers a good compromise between accuracy and computational cost and was chosen for the dynamics simulations reported here.

Table 4.3 lists IPs for imidazole calculated according to Equation (1) (n=0; see Computational Section) with different methods and with the electron propagation theory (EPT) in the OVGF approximation. [42, 43] The IPs calculated according to Koopmans' theorem are presented in the Supporting Information. The first IP, calculated with TD-B3LYP, is in relatively good agreement with the experimental value [39] and corresponds to removal of an electron producing a π hole. The second IP calculated with TD-B3LYP is 9.89 eV; it corresponds to an n hole, and is shifted by only 0.95 eV above IP_1. This is in plain disagreement with the experimental photoelectron spectrum, [39] which shows IP_2 shifted by 1.57 eV above IP_1. The third IP calculated with TD-B3LYP corresponds to a π hole, and the value of 10.45 eV is in good agreement with the experimental value of IP_2 (10.38 eV).

Table 4.3 Vertical ionization potentials [eV] of imidazole calculated with TD-B3LYP/TZVP+mod, RI-CC2/TZVP+mod, and OVGF/aug-cc-pVDZ methods and experimental values from reference [39]. Values are sorted according to the CC2 results. The values in parentheses are relative to IP_1.

		Vertical IP [eV]			Exptl [38]
		TD-B3LYP	RI-CC2	OVGF	
IP_1	π hole	8.94 (0.00)	9.10 (0.00)	8.91 (0.00)	8.81 (0.00)
IP_2	π hole	10.45 (1.51)	10.31 (1.21)	10.35 (1.44)	10.38 (1.57)
IP_3	n hole	9.89 (0.95)	10.69 (1.59)	10.35 (1.44)	–
IP_4	n hole	13.77 (4.83)	14.37 (5.27)	14.32 (5.41)	14.03 (5.22)
IP_5	π hole	14.00 (5.06)	14.46 (5.36)	14.68 (5.77)	14.77 (5.96)

Different from the TD-B3LYP results, IPs calculated with the RI-CC2 method and with OVGF approximation (see Table 4.3) show that the second band (10.38 eV) in the experimental photoelectron spectrum [39] is a mix of IP_2 and IP_3, which are related to π and n holes, respectively. In fact, the experimental band has a double structure that has been previously associated to vibrational progression. [39] These results indicate that the TD-B3LYP method underestimates the IP for the first n hole by about 0.5 eV.

The underestimation of the first n hole is not exclusive to the B3LYP functional and also occurs with the PBE0 functional, as the Koopmans' theorem results in the Supporting Information show. The increase of the fraction of HF exchange in the functional, up to 50 % in BHLYP,

tends to correct the problem, which indicates that it is related to the asymptotic behavior of the exchange functional. In fact, the asymptotically corrected CAM-B3LYP functional [44] predicts IPs similar to those calculated with the RI-CC2 method.

4.3.2 Reaction Paths

Four S_1/S_0 conical intersections have been previously described for imidazole, characterized by NH dissociation, CN dissociation, N puckering, and NH puckering. [27] Here, the linearly interpolated potential-energy paths between the Franck–Condon region and the four conical intersections were calculated at the TD-B3LYP/TZVP+mod level of theory. The pathways to NH dissociation and NH puckering are shown in Figure 4.3. The remaining paths are presented in the Supporting Information.

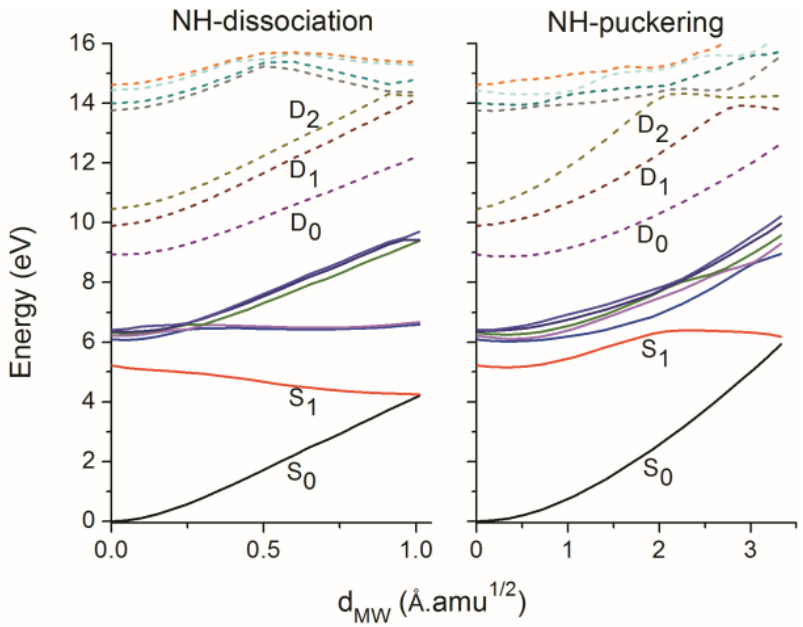

Figure 4.3 Linearly interpolated paths for neutral (solid lines) and cationic (dashed lines) states of imidazole along the NH-dissociation and NH-puckering paths calculated at the TD-B3LYP/TZVPP+mod level.

After S_1 excitation (window A), the only available deactivation channel is NH dissociation. Starting from the same state, the CN-dissociation, N-puckering, and NH-puckering channels have barriers to reach the ground state from S_1. The CASSCF curves show the same features (see Supporting Information in Ref. [27]). The curves calculated with the DFT/MRCI method, [27] however, differ in that that the NH- and N-puckering pathways appear to be barrierless. The differences can be associated with the geometries employed in each case. For the CASSCF and TDDFT calculations, the geometries of the puckered conical intersections were optimized at the same level of theory. In the case of TDDFT, geometry optimization in the S_1 state was performed until the method broke down due to nonconvergence of the Kohn–Sham equations. The last converged geometry was taken as an approximation for the conical intersection. Note that due to limitations of the TDDFT method, [30] the split of the surfaces around this crossing point is not necessarily conical. On the other hand, for the DFT/MRCI method, for which energy gradients are not available, the CASSCF geometries were used in the reaction pathways. For this reason, the CASSCF and TDDFT calculations should represent a better description of the reaction pathways in imidazole than the DFT/MRCI calculations.

4.3.3 Dynamics

Dynamics simulations were started in spectral windows A (5.0–5.2 eV) and B (6.0–6.2 eV). The simulated absorption cross section of imidazole is shown in Figure 4.4, along with indications for both excitation windows. The distribution of trajectories among the several adiabatic states

relevant for each window is given in Table 4.4. For window A, only the S_1 state is populated. For window B, the bright state, which is dominated by the $\pi\pi^*$ configuration, may be S_2 through S_6, depending on the nuclear geometry. As shown in Table 4.4, for most of the geometries generated by the Wigner distribution (see Experimental Section), the bright state is the third excited state, S_3.

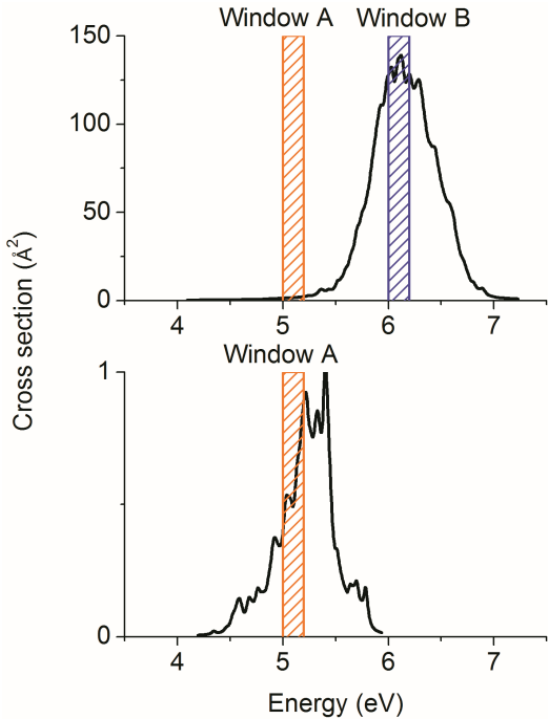

Figure 4.4 Imidazole absorption spectrum calculated with the B3LYP/TZVP+mod method. The energy windows for initial conditions generation are shown. In the bottom graph, only the vibronic-coupled dark band is shown.

Table 4.4 Number of trajectories in each window and for each initial state.

Window	ΔE [eV]	Initial state							Total
		S_1	S_2	S_3	S_4	S_5	S_6	S_7	
A	5.0–5.2	50	–	–	–	–	–	–	50
B	6.0–6.2	–	22	33	26	16	3	–	100

When dynamics simulations are started in window A, the initial population is concentrated in the $^1\pi\sigma_{NH}^*$ (S_1) dark state. All trajectories decay through the NH-dissociation pathway, which is readily accessible from the Franck–Condon region, as shown in Figure 4.3 (left). Figure 4.5 shows the potential-energy profile of one typical trajectory starting in window A. The conical intersection is reached by a strong destabilization of the ground state (closed shell configuration) caused by NH dissociation. The time constant for NH dissociation, obtained by fitting the excited-state population with a single exponential decay function, is 14 fs (Table 4.5). This value is similar to the NH-dissociation time constant of 20 fs previously obtained for pyrrole. [23]

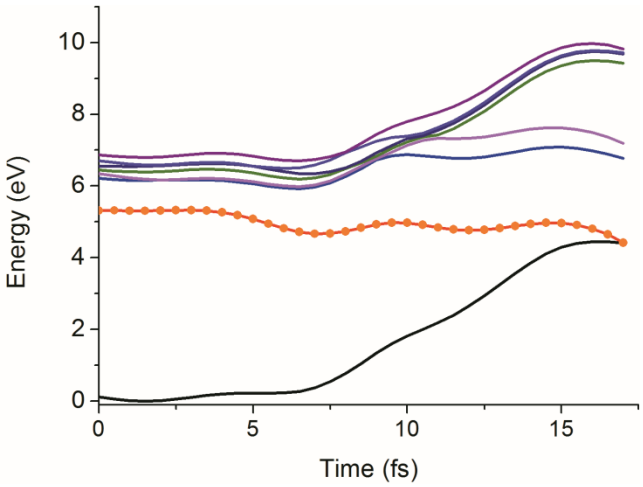

Figure 4.5 Potential energy of the ground and excited states as a function of time for a typical trajectory in window A. The current state at each time is indicated by dots.

Table 4.5 Distribution of mechanisms and lifetimes.

Mechanism	Window A		Window B	
	Distrib.	τ [fs]	Distrib.	τ [fs]
NH dissociation	100 %	14	83 %	105
NH puckering	–	–	16 %	175
N puckering	–	–	–	–
ring opening	–	–	1 %	–
average lifetime	–	14	–	117

Window B lies at 6.0–6.2 eV, which is 1 eV higher than window A. When dynamics simulations start in this window, the extra excitation energy allows the decay to proceed through channels other than the NH-dissociation pathway. Nevertheless, the most important relaxation mechanism is still NH dissociation, with a contribution of 83 %. NH puckering takes place in 16 % of cases, and only 1 % of the trajectories decay through the CN-dissociation conical intersection. Deactivation by puckering at the N site was not observed.

Excitation into window B populates mostly the $^1\pi\pi^*$ state (Table 4.2), which may be S_2 to S_6, depending on the initial geometry. From this state, imidazole first relaxes to the S_1 state. If it reaches S_1 in a region of $\pi\sigma^*_{NH}$ character, it follows the NH-dissociation pathway to the ground state. On the other hand, if it reaches S_1 in a region of $\pi\pi^*$ character, it follows the NH-puckering pathway to the ground state. Either way, relaxation to the S_1 state, obtained by fitting the sum of the S_2 to S_7 populations with an exponential decay function, takes 98 fs. Consequently, the time constant to populate S_0 for window B is larger than that for window A, with a value of 117 fs. In particular, deactivation through the NH-dissociation mechanism is elongated from 14 fs in window A to 105 fs in window B (Table 4.5). Deactivation through the ring-puckering mechanism is even slower and takes place in 175 fs. One single trajectory was deactivated through a ring-opening mechanism, and therefore the deactivation time for this process could not be estimated. The dynamics of imidazole starting in window B with 117 fs time constant is slightly faster than that of pyrrole excited in a equivalent energy window [23] (166 fs).

4.3.4 Evolution of Ionization Potentials

The potential-energy curves for the cation are shown along the NH-dissociation and NH-puckering paths in Figure 4.3. Along the NH-dissociation pathway starting in the S_1 state (the pathway followed when dynamics is started in window A), the D_0 potential energy increases. Consequently, the first ionization potential from the first excited state ($IP_1=E[D_0(t)]-E[S_1(t)]$) increases as well. This quantity, computed for all trajectories in window A, is shown in Figure 4.6 a). A few trajectories oscillate around an equilibrium value, but these trajectories all decay to the ground state before 100 fs.

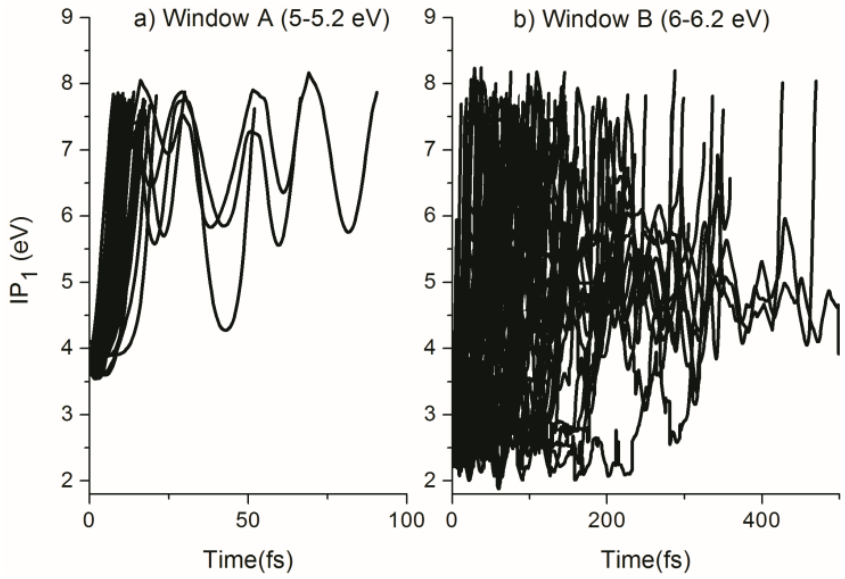

Figure 4.6 Change of IP_1 with time for a) window A and b) window B. This quantity is computed as $IP_1=E[D_0(t)]-E[S_1(t)]$, where n is the current state.

The behavior of IP_1 is more complex when the reaction path is followed from a higher energy excited state than S_1. Between the Franck–Condon region and the S_2/S_1 crossing, which occurs along the puckering coordinate (see Figure 4.3, right), IP_1 is almost constant. After the crossing,

however, following the paths in the S_1 state, IP_1 increases either following the NH-puckering intersection or the NH-dissociation intersection. The complexity of the IP evolution for highly excited states is reflected in the IP profiles during the dynamics started in window B, as shown in Figure 4.6 b).

4.3.5 Two-Color Spectrum

4.3.5.1 Window A (E_{pump}=5.19 eV, E_{probe}=9.30 eV)

Figure 4.7 shows the partial contributions to the photoelectron spectrum in window A from IP_1 to IP_4. For this window, IP_1 covers the range between 8.7 and 13.4 eV, which can be understood by noting that the main deactivation process in window A is NH dissociation. The NH elongation with time directly correlates to the increase of IP_1 (see Figure 4.3), which explains why IP_1 contributes over a wide range of BE.

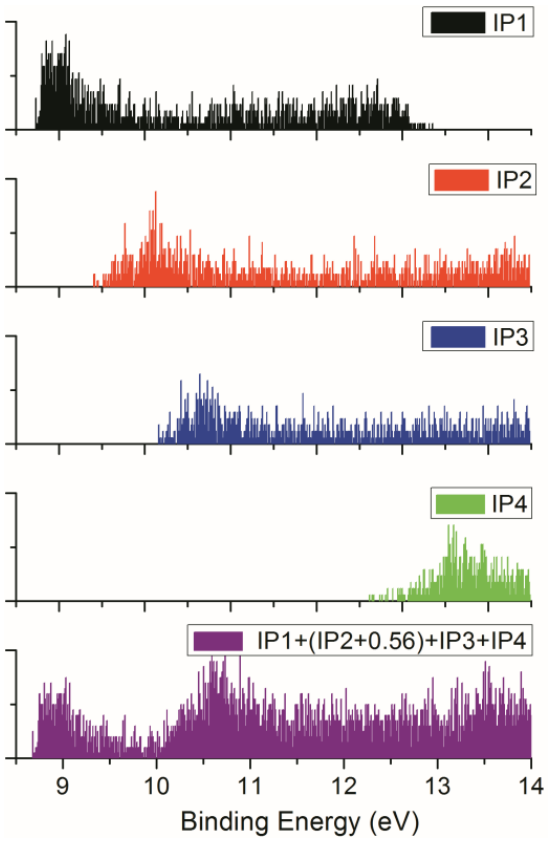

Figure 4.7 Population as a function of the binding energy (BE) integrated over time in window A following ionization into IP_1 through IP_4. The bottom graph shows the sum of all partial contributions. IP_2 was shifted by +0.56 eV to account for underestimation by the TD-B3LYP method.

The shapes of the IP_2 and IP_3 contributions are very similar to each other, but IP_2 is displaced to lower energies due to the TD-B3LYP underestimation of the D_1 state energy, as discussed above. Therefore, to properly consider the contribution of IP_2, it is necessary to shift its distribution by +0.56 eV, which corresponds to the difference between IP_2 and IP_3 for the Franck–Condon geometry. This uniform shift is justified by the fact that the D_2–D_1 energy gap does not change significantly along either the NH-dissociation pathway or the NH-puckering pathway.

The partial contribution of ionization to the third excited state (IP_4) of the cation begins at 12.5 eV. The sum of all contributions (including the shift for IP_2) is shown in the bottom graph of Figure 4.7. It should be compared to the experimental spectrum in Figure 4.2 a). Even though the relative intensities do not agree with the present experimental results, the simulations do show the main qualitative features, a peak at about 9 eV, another at about 10.5 eV and a broad distribution for energies higher than 11 eV.

The main contribution to the first peak is ionization to the ground state of the cation (IP_1). In this region, the contributing species only slightly deviate from the Franck–Condon geometry, and the peak arises during the first few femtoseconds of the dynamics. The second peak can be associated with ionization into the first and the second excited states of the cation (IP_2 and IP_3) added to a background contribution from IP_1. In both cases, the low-energy contribution also occurs during the beginning of the dynamics. The broad high-energy band is mainly due to ionization into IP_4, with non-negligible contributions from IP_1 (below 13 eV), IP_2 and IP_3.

4.3.5.2 Window B (E_{pump}=6.18 eV, E_{probe}=4.93 eV)

Figure 4.8 shows the partial contributions from IP_1, IP_2, and IP_3 to the photoelectron spectrum in window B. As in the case of window A, IP_1 contributes over the whole range, while IP_2 and IP_3 are restricted to the high-energy region. The sum of all partial contributions (bottom graph in Figure 4.8) shows two broad bands. The first band is centered at about 9.2 eV and is dominated by ionization into IP_1, and the second at about 11 eV is composed of ionization into IP_1, IP_2 and IP_3. These two bands at 9.2 and 11 eV are in qualitative agreement with the experimental results (Figure 4.2 e). Additionally, the simulation shows two well-resolved peaks at about 9 eV (energy

gap 0.16 eV), which do not have any correspondence in the experimental spectrum. A structure bearing some similarity, with a 0.18 eV gap, appears in the one-color experimental photoelectron spectrum (Figure 4.1 b–d).

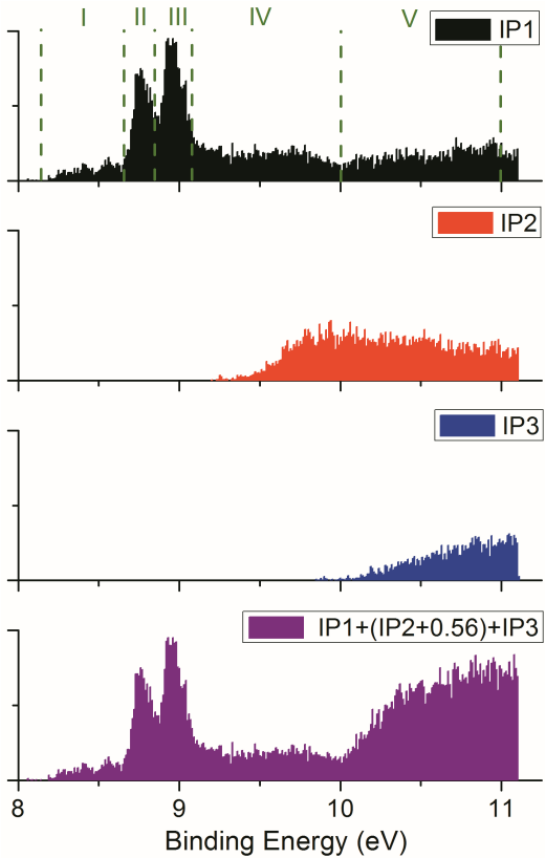

Figure 4.8 Population as a function of the binding energy BE integrated over time in window B, following ionization into IP_1 to IP_3. The bottom graph shows the sum of all partial contributions. IP2 was shifted by +0.56 eV to account for underestimation by the TD-B3LYP method.

In window B, imidazole is initially excited into the $^1\pi\pi^*$ state and the molecule may be ionized from several different states during the excited-state dynamics. For the sake of analysis, the IP_1 contribution is split into five intervals, as illustrated in Figure 4.8. These intervals can be related to different time regimes and different molecular structures. The fraction of each adiabatic state

(current state) for each interval is shown in Table 4.6, which shows that the contribution from the lowest excited states increases systematically from interval I to V. This trend reflects the relaxation of imidazole through excited states with low BE corresponding to the early times in the dynamics.

Table 4.6 Contribution [%] of each adiabatic state to ionization into D_0 for different BE regions.

	I	II	III	IV	V
	8.00–8.72	8.72–8.86	8.86–9.36	9.36–10.00	10.00–11.00
S_1	–	–	–	3	28
S_2	–	–	12	24	20
S_3	–	≈0	27	26	19
S_4	6	26	26	20	14
S_5	21	29	17	13	9
S_6	32	27	11	9	6
S_7	41	17	7	5	4

The population distribution in Table 4.6 can also shed light on the two resolved peaks at about 9 eV. It shows that, while in interval II the maximum occurs for S_5, in interval III the maximum occurs for S_3. This means that, during the dynamics, there is a trend to concentrate either on the top of the manifold of states (around S_5) or on its bottom (around S_3). As shown in Table 4.2, the

energy gap between S_3 and S_5 is 0.13 eV for the Franck–Condon geometry, explaining the gap between the two peaks.

4.4 Discussion

The main features of the excited-state dynamics of imidazole in the gas phase are schematically illustrated in Fig. 4.9. From the Franck-Condon region (center of the graph), there are two important reaction channels: relaxation along the $^1\pi\sigma_{NH}^*$ state (NH- dissociation, right) and relaxation along the $^1\pi\pi^*$ state (ring puckering, left). The importance of each of these two pathways is deeply dependent on the excitation energy.

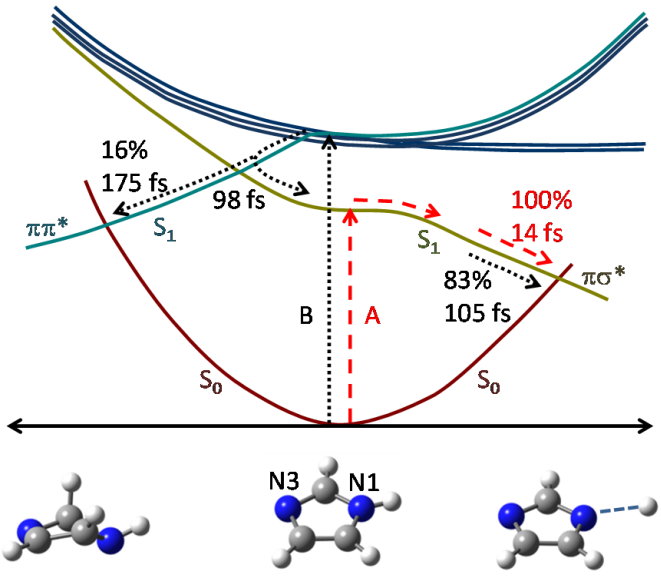

Fig. 4.9 Schematic illustration of the deactivation mechanisms observed in the dynamics simulations of imidazole.

Excitation in the low-energy (5.0–5.2 eV) region (window A) populates the $^1\pi\sigma^*_{NH}$ state, and imidazole is left with no alternative but to relax along this state. Internal conversion under this condition happens on the sub-50 fs timescale, more specifically in 14 fs, according to the simulations.

Excitation in the high-energy (6.0–6.2 eV) region (window B) mainly populates the $^1\pi\pi^*$ state. From there, imidazole relaxes through a manifold of states and the ring-puckering channel is opened in addition to the NH-dissociation channel. In the competition between these two channels, the latter is dominant, accounting for 83 % of the internal conversion events. Internal conversion in window B takes place after 117 fs (weighted average over the two channels). In particular, NH dissociation is much slower in this window (105 fs) than in window A (14 fs) due to the 98 fs needed to relax to the S_1 state.

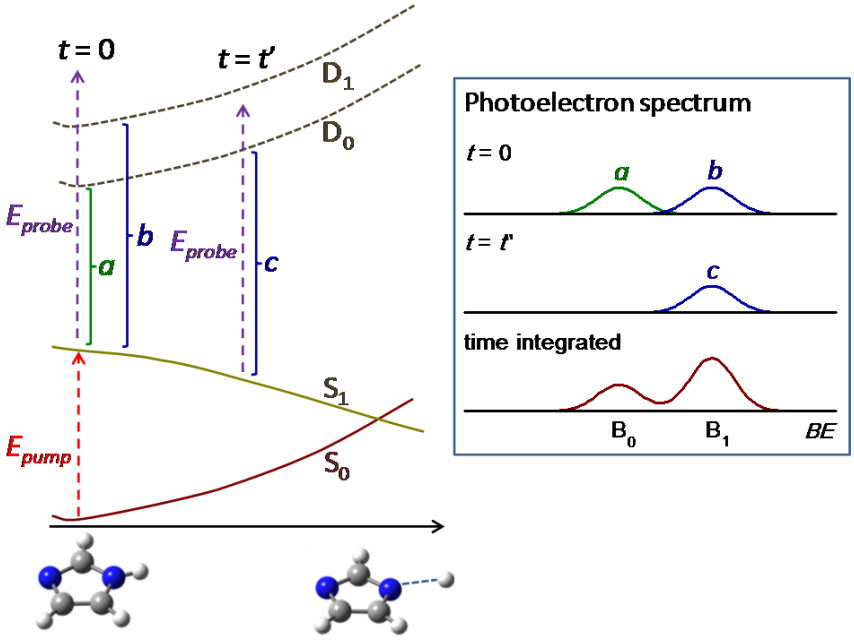

Figure 4.10 Schematic illustration of the pump–probe process (left) and of the different contributions as a function of time to the photoelectron spectrum (right).

Simulations of the photoelectron spectra show that, with the exception of the lowest binding energy band (ca. 9.5 eV), all other features in the spectrum are composed of ionization into multiple states. These contributions are schematically illustrated in Figure 4.10, for window A. At t=0, ionization into D_0 and D_1 states gives rise to bands B_0 and B_1, respectively. Later in the excited-state dynamics (t=t'), band B_0 fades out because of the energetic stabilization of S_1 and destabilization of the cation states. Ionization to D_0 is still possible, but now contributes to the B_1 region.

For both windows, the lowest band (B_0) arises due to ionization into the D_0 state only. For window A, the experimental time for the fade-out of this band (17±15 fs, Table 4.1) should be related to the motion out of the Franck–Condon region, marked by the point where the cationic state energies start to increase (d_{MW}≈2.5 Å amu$^{1/2}$ in Figure 4.3, left). This is the beginning of the dissociation process, still before the internal conversion takes place. The theoretical time for this process is 6 fs. For window B, the fade-out of the lowest band should be related to the transfer from high excited states to the S_1 state. The theoretical time for this process, 98 fs, is in qualitative agreement with the experimental value, 50±30 fs.

For both windows, the B_1 band disappears when ionization into D_0 can no longer occur. Ideally, this would occur near the conical intersection with the ground state, so as to provide the internal conversion time. However, for window A, whose probe energy is 9.3 eV, D_0 can be accessed even after the conical intersection is reached, but before the relaxation of the imidazolyl radical (IP_1=9.93 eV at B3LYP/TZVP-mod level). Thus, τ_D=44±15 fs (Table 4.1) is an upper value for the internal conversion time after excitation into window A. The theoretical value, 14 fs (Table 4.5), on the other hand, is slightly underestimated due to the failure of TDDFT to treat the S_1/S_0

crossing satisfactorily (see Computational Section). In any case, both experimental and theoretical results point to a very short internal conversion time, likely between 14 and 44 fs.

For window B, with probe energy of 4.93 eV, the B_1 band should fade out somewhat before the NH-dissociation conical intersection is reached (see Figure 4.3, left). Therefore, the experimental value τ_D=74±30 fs should be a lower limit on the internal conversion time. The theoretical estimate of 117 fs is, as before, also underestimated by the present TDDFT approach. Thus, both experimental and theoretical data point to an internal conversion time slightly larger than 100 fs in this window.

Total kinetic energy release (TKER) spectroscopy and time-resolved velocity map imaging (TR-VMI) studies of H-atom elimination showed that there are two distinct kinetic energy regimes for H-atom dissociation following imidazole internal conversion. [26, 40] For excitation at 200 nm (window B), the time constants associated with the fast and slow hydrogen atoms are 78±37 and 163±50 fs, respectively. [26] The fast hydrogen release was related with direct dissociation along the $^1\pi\sigma^*_{NH}$ state, while the slow hydrogen release was associated with dissociation along the first excited state of the imidazolyl radical. Our dynamics simulations did not follow the dissociation process taking place after the conical intersection region, but, in principle, imidazole can follow both dissociation pathways, as well as return to the vibrationally hot ground state (from where the dissociation could still occur but on a much longer timescale). Thus, the predicted 105 fs needed to reach the NH-dissociation conical intersection after excitation in window B can be taken as an estimate for the dissociation time in either imidazolyl+H pathway. Note that this value lies between the two aforementioned experimental time constants, within the error bars.

4.5 Conclusion

The ultrafast internal conversion of UV-excited imidazole in the gas phase has been investigated by trajectory-based nonadiabatic dynamics simulations [38] and time-resolved photoelectron spectroscopy. Dynamics simulations were performed at the TDDFT level by employing the fewest-switches surface-hopping approach. One- and two-color photoelectron spectra were recorded spanning a large spectral region. A simple approach for simulating photoelectron spectra based on the theoretical dynamics data has been presented and applied to investigate the contributions from several cationic states to the experimental two-color spectra.

The results show that the dominant mechanisms in internal conversion of imidazole are deeply dependent on the excitation wavelength, with yields and time constants very similar to those observed in pyrrole. Excitation of the dark $^1\pi\sigma^*_{NH}$ band leads to a dominance of the NH-dissociation pathway, with internal conversion taking place in the sub-50 fs timescale. Excitation of the bright $^1\pi\pi^*$ band leads to a competition between the NH-dissociation and NH-puckering mechanisms in a ratio of 21:4, with internal conversion time slower than in the former case by a factor eight.

4.6 Experimental and Computational Methods

The experimental setup consists of a femtosecond (fs) laser system with ultraviolet (UV) conversion capabilities, gaseous molecular beam source, and a photoelectron photoion spectrometer, and has been described in detail elsewhere. [45]

The optical layout is based on a commercially available femtosecond oscillator/amplifier pair (Coherent Inc., Mira 900, and Legend Elite HE). The amplifier output (1 kHz, 800 nm, 130 fs, 3.5 mJ/pulse) is split to produce UV pump and probe pulses at different wavelengths in subsequent frequency-conversion steps. The third (266 nm) or fourth (200 nm) harmonic of the amplifier fundamental is produced in a custom-built setup employing second harmonic and sum-frequency generation. Tunable UV (238–267 nm) pulses are created by optical parametric amplification of white-light continuum (Light Conversion, TOPAS-C). Pump–probe wavelength and power schemes, specific to each experiment, are described below. Pump and probe pulses are time-delayed relative to each other via a motorized optical delay line before being recombined on a dichroic beam splitter and focused (f=30 or 50 cm) collinearly into the interaction region of the photoelectron photoion spectrometer through a UV-fused silica window.

Imidazole (Aldrich, ≥ 99.5 %) is placed in a quartz sample holder located just before the pinhole nozzle and is heated to about 70–110 °C. A continuous molecular beam of the sample vapor carried by helium backing gas (50 Torr) is doubly skimmed to allow differential pumping between the high-vacuum source chamber and ultrahigh-vacuum spectrometer. The magnetic-bottle-type photoelectron spectrometer consists of a permanent ring magnet and a linear solenoid. [46] Photoelectron trajectories are turned toward the solenoid by the inhomogeneous ring magnet field and follow field lines within the solenoid to a microchannel plate detector. Magnetic-bottle electron spectrometers provide a combination of collection efficiency and energy resolution which is well suited to this application, where energy resolution is limited by the femtosecond pulse bandwidth. Time-resolved photoelectron time-of-flight (TOF) spectra are recorded for about 40 000 laser pulses at each delay step in the range $-1000 \leq \Delta t \leq 2000$ fs. Steps of 25 fs are taken in all time-resolved experiments. A molecular beam of 1,3-butadiene (C_4H_6) gas is used for

1) TOF to electron kinetic energy calibration, 2) to determine the temporal overlap between pump and probe (Δt=0), and 3) to determine the timing resolution of each experiment, referred to as the instrument response function (IRF; laser cross correlation of 225 fs).

Separate pump–probe color schemes were used to record TRPES data in excitation windows A and B. For window A, 239.6 nm (5.17 eV) pump pulses (3.1 μJ/pulse) are generated by the TOPAS, while the third harmonic (266.1 nm=4.66 eV) of the Ti:Sa fundamental (6.8 μJ pulse) is used as the probe. Two-photon (1+1′) ionization would result in photoelectrons with about 0.5 eV kinetic energy. Low-energy electrons are not collected efficiently by our magnetic-bottle setup. A three-photon ionization (1+2′) scheme is therefore used for measurements in excitation window A. Energetic photoelectrons (4–5.5 eV) produced in this manner are slowed by a 2 V potential on the ring magnet in order to achieve good collection efficiency and energy resolution. For excitation window B, the fourth harmonic (200.8 nm=6.17 eV) of the Ti:Sa fundamental serves as the pump pulse and a 251.6 nm probe from the TOPAS provides ionization. TRPES spectra are recorded with low pulse energies of 0.5 μJ/pulse (200.8 nm) and 1.5 μJ/pulse (TOPAS) to minimize fragmentation. All two-color spectra are dynamically background subtracted by using shutters that alternately block the pump and probe beams to record unwanted one-color signals.

Steady-state one-color photoelectron spectra are recorded with single-wavelength, two-photon (1+1) ionization of the sample. At higher photon energies (6.17 eV), background electrons produced by stray light become significant and must be subtracted from the photoelectron spectrum. For this purpose, a photoelectron spectrum without the molecular beam is recorded under otherwise identical conditions.

Quantum-Chemical Methods: [38] Vertical excitation energies, linearly interpolated paths between the Franck–Condon geometry and the conical intersections, absorption spectra, and dynamics simulations were computed with TDDFT [47, 48] with the B3LYP functional [49, 50] and the TZVP+mod basis set. The TZVP+mod basis set is the standard def2-TZVP basis set [51] with an extra set of diffuse s and p functions on the heavy atoms. The exponents of these extra Gaussian functions were obtained as one-third of the most diffuse exponent of each kind. A detailed study of vertical excitations for imidazole is reported in reference [27]. Here, other functionals and basis sets were tested as well. The additional functionals were PBE0 [52] and BHLYP. [53] The considered basis sets were TZVPP, [51] aug-cc-pVDZ, aug-cc-pVTZ, (d)-aug-cc-pVDZ, and (d)-aug-cc-pVTZ. [54]

The absorption spectrum of imidazole was calculated by the method reported in reference [55]. The ground-state geometries were sampled by means of a harmonic-oscillator Wigner distribution. A total of seven excited states were included in the simulations to compute the first spectrum band (Figure 4.4, top). The vibronic band between 5.0 and 5.2 eV was also considered separately by an additional spectral simulation including a single excited state (Figure 4.4, bottom). 500 points were calculated as well. In both cases, the width of the Lorentzian line shapes was set to δ=0.05 eV.

Dynamics Simulations: Nonadiabatic dynamics simulations were performed with consideration of the ground state and the seven lowest excited states. The fewest-switches surface-hopping method was employed to account for nonadiabatic events between excited states. [56] Nonadiabatic coupling terms were calculated numerically as proposed in reference [57] and implemented in reference [23]. The TDDFT method employing the B3LYP functional and the

TZVP+mod basis set was used for calculations of electronic energy, energy gradient, and nonadiabatic coupling term. The maximum simulation time was 500 fs. The classical equations were integrated with steps of 0.5 fs, while the quantum equations were integrated with steps of 0.025 fs by using interpolated quantities between classical steps. As the TDDFT description fails in the region of crossings between the first excited state and the ground state, no hopping to the ground state was considered. The excited-state lifetime was estimated as the time required to reach an S_1/S_0 crossing.

The geometries and velocities generated during the spectral simulation procedure were used as initial conditions for the dynamics. The dynamics simulations were initiated in two windows, corresponding to excitation into the 5.0–5.2 eV (window A, see Figure 4.4) and 6.0–6.2 eV range of the spectrum (window B). For window A, 50 trajectories were calculated, and in window B, 100 trajectories were calculated. The number of trajectories starting in each adiabatic state is shown in Table 4.4. The calculations were performed with the Newton-X program [28, 58] interfaced to Turbomole. [59]

Photoelectron-Spectrum Simulations: A simple model was employed to simulate the photoelectron spectrum based on the dynamics results. To analyze the evolution of ionization potentials with time, cationic states for the geometries spanned during the dynamics simulations were computed at the unrestricted TD-B3LYP/TZVP+mod level of theory. Ionization potentials were calculated as the energy difference between the potential energy of the current singlet state of the neutral molecule $S_n(t)$ and the potential energy of the doublet state of the cationic species $D_m(t)$ [Eq. (4.1)]:

$$IP_{m+1}(t) = E\left(D_m(t)\right) - E\left(S_n(t)\right)$$

As for the experiments, the spectrum was plotted in terms of binding energy, which was calculated as [Eq. (4.2)]:

$$\begin{aligned} BE(t) &= E_{pump} + E_{probe} - E_k(t) \\ &= E_{pump} + E_{probe} - \left(E_{probe} - IP_{m+1}(t)\right) = E_{pump} + IP_{m+1}(t). \end{aligned}$$

The ensemble of dynamics points contributing to the simulated photoelectron spectrum was constrained to obey two conditions [Eqs. (4.3) and (4.4)]:

$$\begin{aligned} &E_{tot}\left(S_i(t=0)\right) - E_{tot}\left(S_0(t=0)\right) \\ &= E\left(S_i(t=0)\right) - E\left(S_0(t=0)\right) \le E_{pump}; \end{aligned}$$

$$E_{tot}\left(D_m(t)\right) - E_{tot}\left(S_n(t)\right) \approx E\left(D_m(t)\right) - E\left(S_n(t)\right) \le E_{probe}$$

The first condition ensures that only points whose potential-energy gap between the initial excited state (S_i) and the ground state is smaller than the pump energy E_{pump} were considered. This condition was checked at the initial time of each trajectory. Our initial condition procedure assumes that at t=0 fs the kinetic energy of the excited state is equal to that of the ground state. Then, only the potential energies E, rather than the total energy E_{tot}, need be compared. If, for a specific trajectory, the first condition is not satisfied at t=0 fs, then all points in the trajectory are discarded. Note that inequality (3) is not applied to the whole Wigner distribution, but only to the subset composing the initial-conditions ensemble, which is a good representation of the absorption spectrum including vibronic corrections within a limited energy window. The second condition checks whether a certain point can be ionized to a certain cation state with the available probe energy. This condition must be checked at each time step.

After applying both conditions to the whole set of trajectories, the ensemble of points $\{\mathbf{R}_k^{n,m}(t)\}$ is determined. Here, **R** is the molecular geometry at time *t* for trajectory *k* which can be ionized from S_n to D_m. We assume that the ionization probability is the same for all points in $\{\mathbf{R}_k^{n,m}(t)\}$ and the simulated photoelectron spectrum is finally given by the distribution of $\{\mathbf{R}_k^{n,m}(t)\}$ values consolidated over all variables *k*, *n*, *m*, and *t*. In particular, we analyzed partial contributions to the photoelectron spectrum arising from ionization into particular states D_m. In such cases, the distribution is not consolidated over the variable *m*.

As the transition probabilities are not explicitly computed, the present photoelectron-spectrum simulations should be regarded as a qualitative approximation. Nevertheless, it allowed assignment of different features in the measured spectrum. Procedures for more involved photoelectron spectrum simulations based on dynamics results with explicit computation of ionization probabilities have been reported for other molecules, for instance in references [25], [36] and [60].

4.7 References

[1] M. Barbatti, *WIREs: Comp. Mol. Sci.*, 2011, **1**, 620–633.

[2] J. C. Tully, R. K. Preston, *J. Chem. Phys.*, 1971, **55**, 562–572.

[3] A. Warshel, *Nature*, 1976, **260**, 679–683.

[4] B. R. Smith, M. J. Bearpark, M. A. Robb, F. Bernardi, M. Olivucci, *Chem. Phys. Lett.*, 1995, **242**, 27–32.

[5] P. Cattaneo, M. Persico, *Chem. Phys. Lett.*, 1998, **289**, 160–166.

[6] I. Frank, J. Hutter, D. Marx, M. Parrinello, *J. Chem. Phys.*, 1998, **108**, 4060–4069.

[7] M. Ben-Nun, J. Quenneville, T. J. Martínez, *J. Phys. Chem. A*, 2000, **104**, 5161–5175.

[8] M. Hartmann, J. Pittner, V. Bonacic-Koutecky, *J. Chem. Phys.*, 2001, **114**, 2106–2122.

[9] M. Barbatti, A. J. A. Aquino, J. J. Szymczak, D. Nachtigallová, P. Hobza, H. Lischka, *Proc. Natl. Acad. Sci.*, USA 2010, **107**, 21453–21458.

[10] M. Böckmann, N. L. Doltsinis, D. Marx, *Angew. Chem.*, 2010, **122**, 3454–3456;

Angew. Chem. Int. Ed., 2010, **49**, 3382–3384.

[11] D. Polli, P. Altoe, O. Weingart, K. M. Spillane, C. Manzoni, D. Brida, G. Tomasello, G. Orlandi, P. Kukura, R. A. Mathies, M. Garavelli, G. Cerullo, *Nature*, 2010, **467**, 440–443.

[12] G. A. Worth, L. S. Cederbaum, *Annu. Rev. Phys. Chem.*, 2004, **55**, 127–158.

[13] B. G. Levine, T. J. Martínez, Annu. *Rev. Phys. Chem.*, 2007, **58**, 613–634.

[14] I. V. Hertel, W. Radloff, *Rep. Prog. Phys.*, 2006, **69**, 1897.

[15] H. Du, R. C. A. Fuh, J. Z. Li, L. A. Corkan, J. S. Lindsey, *Photochem. Photobiol.*, 1998, **68**, 141–142.

[16] N. K. Gibbs, J. Tye, M. Norval, *Photochem. Photobiol. Sci.*, 2008, **7**, 655–667.

[17] M. Barbatti, *Phys. Chem. Chem. Phys.*, 2011, **13**, 4686–4692.

[18] S. Perun, A. L. Sobolewski, W. Domcke, *Chem. Phys.*, 2005, **313**, 107–112.

[19] M. Barbatti, H. Lischka, *J. Am. Chem. Soc.*, 2008, **130**, 6831–6839.

[20] Z. Lan, A. Dupays, V. Vallet, S. Mahapatra, W. Domcke, *J. Photochem. Photobiol. A*, 2007, **190**, 177–189.

[21] V. Poterya, V. Profant, M. Farnik, P. Slavicek, U. Buck, *J. Chem. Phys.*, 2007, **127**, 064307.

[22] I. Frank, K. Damianos, *J. Chem. Phys.*, 2007, **126**, 125105.

[23] M. Barbatti, J. Pittner, M. Pederzoli, U. Werner, R. Mitric, V. Bonacic-Koutecký, H. Lischka, *Chem. Phys.*, 2010, **375**, 26–34.

[24] B. Cronin, M. G. D. Nix, R. H. Qadiri, M. N. R. Ashfold, *Phys. Chem. Chem. Phys.*, 2004, **6**, 5031–5041.

[25] T. Fuji, Y.-I. Suzuki, T. Horio, T. Suzuki, R. Mitric, U. Werner, V. Bonacic-Koutecky, *J. Chem. Phys.*, 2010, **133**, 234303–234309.

[26] D. J. Hadden, K. L. Wells, G. M. Roberts, L. T. Bergendahl, M. J. Paterson, V. G. Stavros, *Phys. Chem. Chem. Phys.*, 2011, **13**, 10342–10349.

[27] M. Barbatti, H. Lischka, S. Salzmann, C. M. Marian, *J. Chem. Phys.*, 2009, **130**, 034305.

[28] M. Barbatti, G. Granucci, M. Persico, M. Ruckenbauer, M. Vazdar, M. Eckert-Maksic, H. Lischka, *J. Photochem. Photobiol. A*, 2007, **190**, 228–240.

[29] S. Grimme, *J. Comput. Chem.*, 2006, **27**, 1787–1799.

[30] B. G. Levine, C. Ko, J. Quenneville, T. J. Martínez, *Mol. Phys.*, 2006, **104**, 1039–1051.

[31] M. J. G. Peach, P. Benfield, T. Helgaker, D. J. Tozer, *J. Chem. Phys.*, 2008, **128**, 044118.

[32] N. C. Handy, A. J. Cohen, *Mol. Phys.*, 2001, **99**, 403–412.

[33] S. Grimme, M. Waletzke, *J. Chem. Phys.*, 1999, **111**, 5645–5655.

[34] M. Vazdar, M. Eckert-Maksic, M. Barbatti, H. Lischka, *Mol. Phys.*, 2009, **107**, 845–854.

[35] U. Werner, R. Mitric, V. Bonacic-Koutecky, *J. Chem. Phys.*, 2010, **132**, 174301.

[36] H. R. Hudock, B. G. Levine, A. L. Thompson, H. Satzger, D. Townsend, N. Gador, S. Ullrich, A. Stolow, T. J. Martinez, *J. Phys. Chem. A*, 2007, **111**, 8500–8508.

[37] R. Mitrić, V. Bonačić-Koutecký, J. Pittner, H. Lischka, *J. Chem. Phys.*, 2006, **125**, 024303.

[38] R. Crespo-Otero, M. Barbatti, H. Yu, N. L. Evans, and S. Ullrich, ChemPhysChem., 2011, **12**, 3365–3375.

[39] L. Klasinc, B. Ruščič, F. Kajfež, V. Šunjić, *Int. J. Quantum Chem. Quantum Bio. Symp.*, 1978, **14**, 367–371.

[40] A. L. Devine, B. Cronin, M. G. D. Nix, M. N. R. Ashfold, *J. Chem. Phys.*, 2006, **125**, 184302.

[41] S. Cradock, R. H. Findlay, M. H. Palmer, *Tetrahedron*, 1973, **29**, 2173–2181.

[42] W. von Niessen, J. Schirmer, L. S. Cederbaum, *Comput. Phys. Rep.*, 1984, **1**, 57–125.

[43] Gaussian 09 (Revision A.02), M. J. Frisch, G. W. Trucks, H. B. Schlegel, G. E. Scuseria, M. A. Robb, J. R. Cheeseman, G. Scalmani, V. Barone, B. Mennucci, G. A. Petersson, H. Nakatsuji, M. Caricato, X. Li, H. P. Hratchian, A. F. Izmaylov, J. Bloino, G. Zheng, J. L. Sonnenberg, M. Hada, M. Ehara, K. Toyota, R. Fukuda, J. Hasegawa, M. Ishida, T. Nakajima, Y. Honda, O. Kitao, H. Nakai, T. Vreven, J. Montgomery, J. A., J. E. Peralta, F. Ogliaro, M. Bearpark, J. J. Heyd, E. Brothers, K. N. Kudin, V. N. Staroverov, R. Kobayashi, J. Normand, K. Raghavachari, A. Rendell, J. C. Burant, S. S. Iyengar, J. Tomasi, M. Cossi, N. Rega, N. J. Millam, M. Klene, J. E. Knox, J. B. Cross, V. Bakken, C. Adamo, J. Jaramillo, R. Gomperts, R. E. Stratmann, O. Yazyev, A. J. Austin, R. Cammi, C. Pomelli, J. W. Ochterski, R. L. Martin, K. Morokuma, V. G. Zakrzewski, G. A. Voth, P. Salvador, J. J. Dannenberg, S. Dapprich, A. D. Daniels, Ö. Farkas, J. B. Foresman, J. V. Ortiz, J. Cioslowski, D. J. Fox, *Gaussian, Inc.*, Wallingford, CT, **2009**.

[44] T. Yanai, D. P. Tew, N. C. Handy, *Chem. Phys. Lett.*, 2004, **393**, 51–57.

[45] N. L. Evans, S. Ullrich, *J. Phys. Chem. A*, 2010, **114**, 11225–11230.

[46] P. Kruit, F. H. Read, *J. Phys. E*, 1983, **16**, 313.

[47] R. Bauernschmitt, R. Ahlrichs, *Chem. Phys. Lett.*, 1996, **256**, 454–464.

[48] F. Furche, R. Ahlrichs, *J. Chem. Phys.*, 2002, **117**, 7433–7447.

[49] A. D. Becke, *J. Chem. Phys.*, 1993, **98**, 5648–5652.

[50] P. J. Stephens, F. J. Devlin, C. F. Chabalowski, M. J. Frisch, *J. Phys. Chem.*, 1994, **98**, 11623–11627.

[51] F. Weigend, M. Häser, H. Patzelt, R. Ahlrichs, *Chem. Phys. Lett.*, 1998, **294**, 143–152.

[52] J. P. Perdew, K. Burke, M. Ernzerhof, *Phys. Rev. Lett.*, 1996, **77**, 3865–3868.

[53] A. D. Becke, *J. Chem. Phys.*, 1993, **98**, 1372–1377.

[54] T. H. Dunning, *J. Chem. Phys.*, 1989, **90**, 1007–1023.

[55] M. Barbatti, A. J. A. Aquino, H. Lischka, *Phys. Chem. Chem. Phys.*, 2010, **12**, 4959–4967.

[56] J. C. Tully, *J. Chem. Phys.*, 1990, **93**, 1061–1071.

[57] S. Hammes-Schiffer, J. C. Tully, *J. Chem. Phys.*, 1994, **101**, 4657–4667.

[58] M. Barbatti, G. Granucci, M. Ruckenbauer, F. Plasser, J. Pittner, M. Persico, H. Lischka, *NEWTON-X: a package for Newtonian dynamics close to the crossing seam,* **2011**,

[59] R. Ahlrichs, M. Bar, M. Haser, H. Horn, C. Kolmel, *Chem. Phys. Lett.*, 1989, **162**, 165–169.

[60] H. Tao, T. K. Allison, T. W. Wright, A. M. Stooke, C. Khurmi, J. v. Tilborg, Y. Liu, R. W. Falcone, A. Belkacem, T. J. Martinez, *J. Chem. Phys.*, 2011, **134**, 244306.

CHAPTER 5

EXPLORING ULTRAFAST H-ATOM ELIMINATION VERSUS PHOTOFRAGMENTATION PATHWAYS IN PYRAZOLE FOLLOWING 200 NM EXCITATION

5.1 Introduction

Recent years have seen numerous studies into the photophysics of biomolecules, such as DNA bases, [1] amino acids [2] and their associated subunits [3] from both experimental and theoretical standpoints. In the case of the DNA bases (particularly the purine derived bases adenine and guanine) this has been fuelled by an attempt to more acutely understand their remarkable resistance toward ultraviolet (UV) radiation, resulting in low fluorescence quantum yields. [1] One of the theories put forward to explain this was triggered by the seminal computational studies of Sobolewski et al., which places photochemistry driven by $^1\pi\sigma^*$ states as a centerpiece for rationalizing this photoresistive behavior. [4] In this work they proposed that dissociative $^1\pi\sigma^*$ states, localized along heteroatom hydride (X–H, where X is most commonly O or N) bond coordinates, may be either directly or indirectly accessed following excitation from the electronic ground state (S_0). Specifically, in the case of indirect excitation, optically bright $^1\pi\pi^*$ states were implicated as notable candidates for imparting reactive flux onto the $^1\pi\sigma^*$ surface following internal conversion (IC). Dissociative $^1\pi\sigma^*$ states may then facilitate either (i) an effective route for nonradiative relaxation back to S_0 via efficient electronic state couplings or (ii) direct X–H bond fission resulting in the abstraction of H-atoms.

These theoretical studies have since given rise to a plethora of experimental research focused on obtaining greater insights into the behavior of species predicted to exhibit σ* mediated relaxation dynamics. This research has included both time and frequency domain measurements, some of the most prominent of which have included multimass ion imaging, [5, 6] H-atom photofragment translational spectroscopy (PTS), [3, 7] time-resolved velocity map ion imaging (TR-VMI), [8-10] and time-resolved photoelectron spectroscopy. [11-14] Recently, the $^1\pi\sigma^*$ oriented photochemistry of imidazole (Figure 5.1 a), a five-membered N-containing heterocycle that acts as the UV chromophore in biomolecules such as adenine and histidine, has received notable attention, both experimentally [15, 16] and computationally. [17] Pyrazole (Figure 5.1 b), a structural isomer of imidazole obtained by a simple exchange of the N and C atoms at the 2- and 3-positions within the aromatic ring, is much more elusive within biological motifs. [18] As a result, its photochemistry and particularly the participation of $^1\pi\sigma^*$ surfaces located along the N–H coordinate has received much less attention. [19] However, gaining a greater understanding of its photochemistry is by no means without intrinsic merit, as it can provide insight into how the positions of the N atoms within this class of heterocycles influence resultant dynamics of nitrogen rich aromatics. Here, we turn our attention to gaining a greater understanding of the complex photochemistry occurring in pyrazole after 200 nm excitation. Specifically, we aim to (i) extract time scales for the elimination of H-atoms from the N–H coordinate mediated via either direct or indirect population of the lowest energy repulsive $^1\pi\sigma^*$ ($1^1A''$) state, (ii) extract time scales for any alternative relaxation channels originating from the $^1\pi\pi^*$ ($2^1A'$) state leading to large molecular fragments, and finally, (iii) compare and contrast the ultrafast dynamics of pyrazole with those of its structural isomer imidazole. [16]

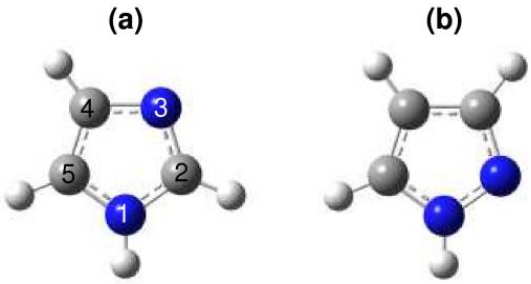

Figure 5.1 Molecular structures of (a) imidazole and (b) pyrazole.

Ashfold and co-workers have recently investigated the wavelength dependent H-atom photolysis of pyrazole using the high resolution H-atom (Rydberg) time-of-flight (TOF) technique at multiple excitation energies in the range $220 \geq \lambda \geq 193.3$ nm. [19] Their results show that photoexcitation at wavelengths greater than 220 nm (5.64 eV) results in no appreciable H-atom signal. Following excitation at 220 nm the recorded total kinetic energy release (TKER) spectrum of H-atoms displays a single broad structureless distribution peaked at around ~1500 cm^{-1} with a lower intensity tail extending to around 12 000 cm^{-1}. This upper wavelength threshold of 220 nm for the observation of H-atom production is supported by the previously measured vacuum UV (VUV) absorption spectrum of pyrazole in the vapor phase, [20] which shows the onset of a broad absorption feature at ~220 nm. The low kinetic energy (KE) feature persists down to a wavelength of 193.3 nm (6.40 eV). The origins of the slow H-atoms in this feature were attributed to population of the first $^1\pi\pi^*$ ($2^1A'$) excited state followed by either IC back to a vibrationally hot S_0 (X^1A') ground state and subsequent statistical unimolecular decay (producing a statistical distribution of slow H-atoms) or a resonance-enhanced multiphoton ionization (REMPI) process via the $^1\pi\pi^*$ state, resulting in dissociative ionization, producing H-atoms (and corresponding cofragment ions). [19] For $\lambda \leq 214$ nm (5.78 eV), a new lower

intensity feature at high KE (~9500 cm^{-1}) begins to appear within the high energy tail of the low KE feature. Such a feature is characteristic of nascent fast H-atoms and the mechanism for their formation was assigned to direct excitation of the repulsive $^1\pi\sigma^*$ ($1^1A''$) state, resulting in rapid N–H bond fission and the production of pyrazolyl radical cofragments (C_{2v} symmetry) in both its ground ($\tilde{X}^2A_2$) and first excited ($\tilde{A}^2B_1$) states, which are separated by only ~270 cm^{-1} (~0.03 eV) and undergo strong pseudo-Jahn–Teller vibronic mixing. [19, 21]

A number of ab initio quantum calculations, performed at varying levels of theory, have also been used to obtain insight into the vertical excitation energies of the singlet excited states of pyrazole. [19, 22, 23] Multireference configuration interaction (MRCI) calculations by Palmer and Guest [23] determined that the onset of the $2^1A' \leftarrow X^1A'$ ($\pi^* \leftarrow \pi$) and $1^1A'' \leftarrow X^1A'$ ($3s,\sigma^* \leftarrow \pi$) transitions lie at 5.61 and 5.87 eV, respectively, which correlate well with the aforementioned experimental observations. [19, 20] These calculations were later complemented by complete active space calculations with second-order perturbation theory (CASPT2) by King *et al.*, [19] whose adiabatic excitation values quantitatively agree with the energies of Palmer and Guest. At the same level of theory, King *et al*. also calculated the ground X^1A' and excited $1^1A''$ ($^1\pi\sigma^*$) potential energy profiles with respect to the N–H bond axis. These profiles indicate that at elongated N–H bond distances (~2.5 Å) the energy of the $1^1A''$ state decreases and becomes degenerate with the X^1A' ground state, giving rise to a $^1\pi\sigma^*/S_0$ conical intersection (CI). In addition to this, King et al. also propose, on the basis of empirical information for the energy splitting between the $\tilde{X}^2A_2$ and $\tilde{A}^2B_1$ states in the pyrazolyl radical products (~0.03 eV) [19, 21] and the vertical excitation for a second higher energy $2^1\pi\sigma^*$ state (obtained from information regarding pyrazole ionization potentials [22]), that there is likely to be an additional $2^1\pi\sigma^*/S_0$ CI very close in both energy and geometry to the aforementioned CI associated with the $1^1A''$ and

X^1A' state degeneracy. These findings are in line with studies by Yarkony and co-workers conducted on the pyrazolyl radical, [24, 25] which potentially implicates the presence of a rarer three-state CI ($2^1\pi\sigma^*/^1\pi\sigma^*/S_0$). Such electronic state properties are notably different from those calculated for imidazole, [17, 19] which is predicted to exhibit no close lying/iso-energetic degeneracies along the ground state potential. By measuring the nascent H-atoms as a function of kinetic energy, it may be possible to gain insights into any competition between adiabatic and nonadiabatic dynamics at these state crossings. These dynamics will govern how the propagating wave packet bifurcates into channels that yield either (i) the closely spaced $\tilde{X}^2A_2$ and $\tilde{A}^2B_1$ pyrazolyl radical products (correlated to the diabatic $^1\pi\sigma^*$ and $2^1\pi\sigma^*$ dissociation asymptotes, respectively) or (ii) radical products in their second excited $\tilde{B}^2B_2$ state (correlating to the diabatic X^1A' ground state dissociation asymptote).

Because the origins of the $2^1A' \leftarrow X^1A'$ ($\pi^* \leftarrow \pi$) and $1^1A'' \leftarrow X^1A'$ ($3s,\sigma^* \leftarrow \pi$) transitions lie near 5.6 and 5.9 eV, respectively, [18, 22] and are both transition dipole allowed, both states can in principle be accessed at 200 nm (6.2 eV), potentially resulting in competing relaxation mechanisms. In addition to the $^1\pi\sigma^*$ mediated dynamics described above, the $^1\pi\pi^*$ state may possibly relax into a variety of ring deformation pathways, as has been predicted for the related heterocycle imidazole. [17] In imidazole, these have been described as (i) ring-opening at the N_1–C_2 bond (see Figure 5.2 a) and (ii) various ring-puckering pathways in order of increasing energy of the $^1\pi\pi^*/S_0$ potential energy surface (PES) crossings. [17] It has been suggested in related heteroaromatics [26-28] that at the $^1\pi\pi^*/S_0$ CIs these ring deformation modes can lead to experimentally observed photofragmentation patterns. [29, 30] In particular, Barbatti et al. have specifically called for experimental investigation of time-resolved fragmentation patterns to better understand the $^1\pi\pi^*$ ($2^1A'$) → ring deformation → photofragment pathway in imidazole.

[17] Heterocycle relaxation involving ring deformation modes may account for up to 20% of the total deactivation, [17, 26-28] and experimental studies to probe similar deactivation mechanisms that may operate in pyrazole should not be neglected.

In this paper we investigate the electronic excited state dynamics of pyrazole after 200 nm excitation, including both $1^1A''$ ($^1\pi\sigma^*$) and $2^1A'$ ($^1\pi\pi^*$) mediated relaxation pathways. First we report TR-VMI measurements that investigate the ultrafast time scales for N–H bond fission in pyrazole. TR-VMI has the benefit of simultaneously affording both temporal *and* energetic information regarding the H-atom elimination process. By partitioning these H-atoms as a function of energy (rather than measuring a total H-atom yield), we can extract individual appearance time scales for low energy H-atom distributions and any resulting high energy H-atoms, which may be generated through dissociation along $^1\pi\sigma^*$ surfaces. Time-resolved ion yield (TRIY) experiments are also presented to investigate possible $^1\pi\pi^*$ ($2^1A'$) → ring deformation → photofragment relaxation channels. Fragmentation dynamics are observed directly from the temporal evolution of our mass spectrum and are analyzed within the theoretical models put forward for the structural isomer imidazole. [17] (The VMI experiments were performed by the Stavros group.) [31]

5.2 Experimental Section

Two separate, but complementary, experiments were performed to fully investigate $1^1A''$ ($^1\pi\sigma^*$) and $2^1A'$ ($^1\pi\pi^*$) mediated dynamics in pyrazole following 200 nm photolysis. The TR-VMI experiments performed at the University of Warwick U.K. (UW) [31] and the TRIY experiments performed at the University of Georgia (UGA) will be described in this section. The reader is directed to previous work for further experimental details. [9, 14, 32]

5.2.1 Time-Resolved Velocity Map Ion Imaging [31]

TR-VMI experiments at UW utilize femtosecond (fs) laser pulses derived from a commercial oscillator and regenerative amplifier system (Spectra-Physics, Tsunami and Spitfire XP-Pro). The regenerative amplifier operates at 125 Hz for these experiments and delivers 3 mJ/pulse centered at 800 nm with a temporal full width at half-maximum (fwhm) of 45 fs. These fundamental pulses have a bandwidth of ~30 nm (~500 cm^{-1}). The fundamental output is subsequently split into three beams of equal energy (1 mJ/pulse). Of these three beams, one is up-converted into the 200 nm pump, which is achieved via frequency doubling the fundamental in a type-I β-barium borate (BBO) crystal to generate 400 nm, followed by successive frequency mixing (type-II and type-I BBO crystals, respectively) with the residual 800 nm pulses to generate third harmonic (267 nm) and finally the desired 200 nm fourth harmonic (~1 μJ/pulse). The remaining two beams are used to pump two optical parametric amplifiers (Light Conversion, TOPAS model 4/800/f), of which one is used in these experiments to generate 243.1 nm probe pulses (~7 μJ/pulse). These 243.1 nm probe pulses are used to selectively ionize any H-atoms via a 2 + 1 REMPI process, resonant with the two-photon allowed 2s ← 1s transition. The pump and probe are temporally delayed with respect to each other using a computer controlled delay stage (Physik-Instrumente, M-505) with a minimum step size for these experiments of 25 fs. Both pump and probe pulses are focused through f = 50 cm MgF_2 and CaF_2 lenses, respectively, and are collinearly recombined at a dichroic mirror. These collinearly focused beams then enter the interaction region of a VMI spectrometer where they perpendicularly intersect a molecular beam of pyrazole. Nonresonant multiphoton ionization of NH_3 and Xe is employed as a method for determining both the delay position corresponding to the temporal overlap of the pump and

probe (Δt = 0), to within an accuracy of ±15 fs, and the associated cross-correlation/instrument response function (IRF). For these experiments a Gaussian IRF is used with a measured fwhm of ~160 fs.

A molecular beam is generated by seeding pyrazole (Sigma-Aldrich, ≥ 98%) molecules in He (2–3 bar) and is transferred into vacuum using an Even–Lavie pulsed solenoid valve [33] operating at 125 Hz and synchronized to the laser system. The valve is heated to 100 ℃ to generate a sufficient vapor pressure of pyrazole (measurements have been carried out at lower temperatures with the results presented in sections and remaining unchanged). The backing pressure and opening time of the valve has been optimized to reduce the degree of clustering of the parent ion relative to the parent ion monomer. Typical opening times for the valve are between 10 and 15 μs. The molecular beam machine consists of differentially pumped source and interaction chambers, partitioned by a 2 mm skimmer. The pulsed valve is housed within the source chamber, while the interaction chamber contains VMI optics, replicating the arrangement described by Eppink and Parker. [34] Generated cations are then accelerated toward a position sensitive detector (under VMI focusing conditions), which consists of a pair of 40 mm diameter chevron microchannel plates (MCPs) coupled to a P-43 phosphor screen (Photek, VID-240). By applying a timed voltage pulse (Behlke) to the rear MCP, we are able to gate the detector to measure only the H^+ signal. A two-dimensional projection of the three-dimensional H^+ distribution is subsequently obtained by capturing the light emitted from the phosphor screen using a charge-coupled device (Foculus). One-dimensional radial/velocity spectra of the ionized H-atoms are obtained through deconvolution of the recorded H^+ images by incorporating a polar onion-peeling method [35] into our data acquisition program coded in LabVIEW.

5.2.2 Time-Resolved Ion Yield

The experimental setup at UGA consists of a commercially available femtosecond laser system, continuous-expansion molecular beam source and photoelectron-photoion spectrometer. The femtosecond system comprises an oscillator and regenerative amplifier pair (Coherent Inc., MIRA 900 and Legend Elite-HE) that produces a kilohertz train of 800 nm pulses with 12 nm (~200 cm^{-1}) bandwidth and 3.5 mJ/pulse energy. The amplifier output is split into 0.75 and 1.5 mJ/pulse beams for subsequent conversion into the UV pump and probe pulses, respectively. The 200 nm pump is produced in a custom-built setup using successive frequency doubling, and two sum-frequency generation steps in type-I BBO crystals. UV probe pulses are created by optical parametric amplification (Light Conversion, TOPAS-C), tuned to 243.1 nm as in the TR-VMI studies. For investigation of excited state fragmentation pathways, the power of the pump and probe beams is intentionally kept low to reduce multiphoton processes, which can lead to unwanted nonresonant fragmentation. Pulse energies for the pump and probe are typically 1.0 and 3.5 μJ/pulse, respectively, as measured at the spectrometer input. One-color (i.e., pump or probe alone) signal intensity is small compared to that of the pump–probe signal.

The pump–probe delay (Δt) is controlled via a motorized delay line (Newport, ESP 300) in the probe beam path with a minimum step size of 25 fs. The two beams are combined at a dichroic optic and are focused by two independently adjustable f = 50 cm UV fused silica lenses into the interaction region of the photoelectron-photoion spectrometer, where they intersect a molecular beam of pyrazole seeded in He.

The molecular beam is produced by continuous coexpansion of He and pyrazole vapor through a 200 μm pinhole and is doubly skimmed by 3 and 5 mm diameter conical apertures (Beam Dynamics), respectively, before entering the spectrometer. Pyrazole (Sigma-Aldrich, ≥98%) is

held in a quartz cup behind the pinhole under ~50 Torr (~7×10^{-2} bar) of He and is heated to 40 ℃ to produce sufficient vapor pressure. The pinhole to skimmer distance (1.5 and 20 cm to the first and second skimmer, respectively) assures that a well collimated beam enters the spectrometer where it is intersected by pump and probe pulses. Interaction of the laser and pyrazole beams produces cations that are mass analyzed in a Wiley–McLaren like TOF spectrometer whose flight tube axis is mutually orthogonal to both the laser and molecular beam paths. Nonresonant multiphoton ionization of 1,3-butadiene (C_4H_6), nitric oxide (NO), and NH_3 at 200 and 243.1 nm is employed for TOF to ion-mass calibration, for determination of temporal overlap (Δt = 0), and for determination of the IRF. Here, the IRF, and therefore the timing resolution of this experiment is ~225 fs.

All spectra shown in section are recorded for the pump–probe delay range $-850 \leq \Delta t \leq +2150$ fs in 25 fs steps and the yield of peaks at m/z = 14, 28, 40, 41, and 68 is monitored as a function of Δt. Molecular decay pathways resulting in each m/z peak are illuminated through fits of these TRIY data, as will be discussed in section 5.3.3.

5.3 Results and Discussion

5.3.1 H^+ Image, Total Kinetic Energy Release Spectrum, and Recoil Anisotropies [31]

Figure 5.2 displays a H^+ velocity map ion image obtained from photoexcitation of pyrazole at 200 nm, followed by selective probing of dissociated H-atoms using 2 + 1 REMPI at 243.1 nm. The temporal delay between the pump and probe pulses has been set to Δt = +2.5 ps, such that the pump (200 nm) precedes the probe (243.1 nm). For completeness, we also highlight that (i) when the probe precedes the pump (i.e., negative time delays), there is negligible H^+ signal, indicative of selectively probing only nascent H-atoms at positive pump–probe delays, and (ii)

detuning the probe wavelength off-resonance ($\lambda \neq 243.1$ nm) results in no measurable H^+ signal, confirming that only neutral H is being ionized and detected when on-resonance ($\lambda = 243.1$ nm). The pump–probe image in Figure 5.2 displays two distinct features, the first of which is a broad distribution with a large signal density around the center of the image. This signal corresponds to probing of low KE H-atoms ($\sim$2000 cm^{-1}) as the radial distance, *R*, from the center of the image is directly proportional to the velocity, *v*, of the photodissociated H-atoms. *R* can then in turn be translated into KE space using both the appropriate $R^2 \propto KE$ Jacobian [36] and a calibration factor, the latter of which is obtained via photodissociation of HBr at 200 nm. [37] The second feature is a narrower distribution situated at larger radii, correlating to higher KE ($\sim$10 000 cm^{-1}), with a pronounced H-atom recoil anisotropy that peaks around 90 ° to the pump polarization vector, ε, which is represented by the double headed arrow in Figure 5.2. The preservation of this recoil anisotropy in the measured image suggests that these high KE H-atoms are generated on a time scale faster than the rotational period of the neutral pyrazole parent and commonly implicates a rapid photodissociation pathway via a dissociative state. Thus, we attribute these H-atoms to fast N–H bond fission along the repulsive $1^1A''$ ($^1\pi\sigma^*$) state. In the succeeding paragraphs we discuss the origins of both the low and high KE features in greater detail.

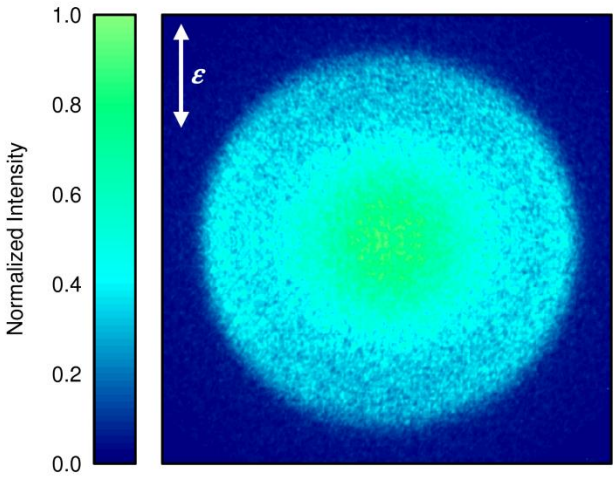

Figure 5.2 Raw velocity map image of H^+ generated following excitation of pyrazole at 200 nm and probing H-atoms with 243.1 nm. The pump–probe delay was set to Δt = +2.5 ps. The polarization of the pump laser, ε, relative to the image is shown by the double-headed arrow.

In Figure 5.3 (a) we show the H-atom TKER spectrum at Δt = +2.5 ps (circles), which is derived from the H^+ image in Figure 5.2 using a polar onion-peeling algorithm. [35] The TKER scale has been arrived at by assuming $C_3N_2H_3$ (m/z = 67 amu) as the radical cofragment. The spectrum displays a clear bimodal distribution with a low KE feature (correlated with the signal at the center of the H^+ image) peaking at ~2000 cm^{-1} and possessing a tail that decays in intensity at higher KE. The second feature, at higher KE, corresponds to the anisotropic signal observed at larger radii in the image and exhibits a Gaussian profile centered at ~9800 cm^{-1}. These low and high KE features are fitted to a statistical Boltzmann distribution and a Gaussian function, respectively (red and blue shading in Figure 5.3 (a), respectively), with the overall fit to the TKER spectrum shown by the solid black line (more details of this fitting model are provided in ref [9]. Qualitatively, the spectrum recorded in Figure 5.3 (a) is in reasonable agreement with that previously reported in the nanosecond PTS studies of Ashfold and co-workers following

photolysis at 193 nm. [19] The nanosecond PTS spectrum also displays a bimodal distribution containing both low and high KE features, the latter of which these authors assign to *direct* N–H fission along the $1^1A''$ state. [19] However, the H-atom signal ratio between the low and high KE peaks is noticeably reversed in the nanosecond spectrum, with the high KE feature appearing ~10 times less intense than the peak at low KE. We put forward arguments to explain the differences between the two spectra in the discussion that follows.

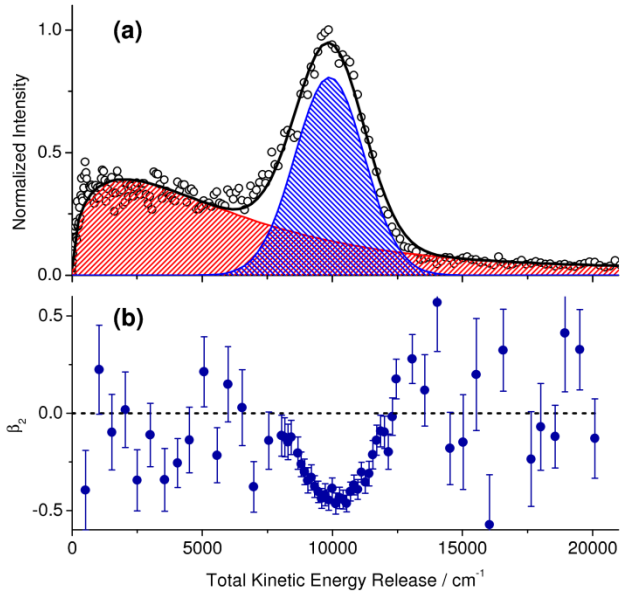

Figure 5.3 (a) H-atom TKER spectrum derived from the image shown in Figure 5.2. The corresponding fits to the TKER spectra include a statistical function (red) and a Gaussian distribution (blue). (b) Associated β_2 recoil anisotropy parameters as a function of TKER.

The high KE feature centered at ~9800 cm^{-1} is attributed to rapid N–H dissociation, mediated by the $1^1A''$ state, resulting in pyrazolyl radical cofragments in either the ground $\tilde{X}^2A_2$ or first excited $\tilde{A}^2B_1$ states. However, due to the restricted energy resolution of our measurements ($\Delta E/E$ ≈ 5% at ~10 000 cm^{-1}) it is unfortunately not possible to determine the exact branching ratio

between these two final product channels, as they are separated by only ~270 cm^{-1}. [19, 21] As a result, and for simplicity, we herein only refer to this feature in terms of the radical ground $\tilde{X}^2A_2$ state product channel. The maximum TKER associated with the high KE feature, $TKER_{max}$ (~13 000 cm^{-1}) may also be used to provide an estimate for the strength of the N–H bond, D_0(N–H), using the following expression:

$$D_0(\mathrm{N{-}H}) = h\nu_{pump} - TKER_{max} \qquad (1)$$

where $h\nu_{pump}$ is the energy of the pump pulse (50 000 cm^{-1}) and assuming that H-atoms generated with $TKER_{max}$ are associated with pyrazolyl radicals in their vibrational ground state, $\tilde{X}^2A_2$ (v = 0). Using the values above yields an approximate value for D_0(N–H) of ~37 000 cm^{-1}, which, within the resolution of our VMI spectrometer, is in very good agreement with previously reported values by King *et al.* (37 680 ± 49 cm^{-1}) [19] and Gianola *et al.* (37 210 ± 210 cm^{-1}). [38]

It is important to elucidate the photophysical mechanism that imparts reactive flux onto the $1^1A''$ state and gives rise to the dominant high KE component of the TKER spectrum in Figure 5.4 (a). Noting that (i) the excitation threshold for the $1^1A''$ state is ~214 nm (~47 150 cm^{-1}) [19, 23] and that (ii) as a result of pyrazoles low symmetry (C_s point group), excitation to the dissociative $1^1A''$ manifold is transition dipole allowed ($A' \otimes a'' \otimes A'' = A'$), direct population of the $1^1A''$ state is feasible at 200 nm (50 000 cm^{-1}), despite the relatively small oscillator strength of the $1^1A'' \leftarrow X^1A'$ transition. Alternatively, it may also be possible to transfer flux to the $1^1A''$ surface indirectly, following excitation to the optically bright $2^1A'$ ($^1\pi\pi^*$) surface. The $2^1A'$ state exhibits an excitation onset of ~220 nm (~45 450 cm^{-1}) [19, 20] and may then undergo $2^1A' \rightarrow 1^1A''$ IC. To identify the correct mechanism, the recoil anisotropy, β_2, of the measured H-atom photoproducts in the high KE peak may be utilized; as a given electronic state transition will

have the largest excitation probability when its associated dipole moment vector, μ, is aligned parallel to the electric field vector of the pump pulse, ε, the measured recoil anisotropy will provide insight into the orientation of the dissociating N–H bond relative to μ. Hence, one may extrapolate information regarding the initially populated electronic state. [39] The measured recoil anisotropies are displayed as a function of TKER in Figure 4.4 (b) (error bars correspond to a single standard deviation), where the values for β_2 are obtained by fitting the H-atom angular distributions at each radius in the image to the even terms of a second-order Legendre polynomial. [36] Formally, β_2 may take values in the range $-1 \leq \beta_2 \leq 2$, where the limiting values of −1 and +2 correspond to purely perpendicular and parallel transitions, respectively. For the high KE peak at 9800 cm^{-1} we measure a nonlimiting negative recoil anisotropy of $\beta_2 \approx -0.5$, which is in agreement with the value previously determined by Ashfold and co-workers at 193 nm. [19] From this we may infer that N–H bond fission does not occur parallel to the excitation transition dipole, allowing us to negate indirect population of the $1^1A''$ state from the optically bright $2^1A'$ surface, as symmetry conservation and theory calculations show that the transition dipole moment for $2^1A' \leftarrow X^1A'$ excitation is in the molecular plane and is oriented near parallel to the N–H coordinate, respectively. [19] Ergo, this indirect pathway would yield H-atoms predominantly parallel to ε with a positive β_2 value, which we do not observe here. The alternative *direct* method for imparting flux to the repulsive $1^1A''$ PES does, however, correlate with the observed negative β_2 value, as symmetry and calculations show that the $1^1A'' \leftarrow X^1A'$ transition moment is aligned out of the molecular plane and approaching 90 ° to the dissociating N–H bond, giving rise to a perpendicular (negative) recoil anisotropy. [19] We therefore propose that the high KE peak in Figure 5.2 a. originates from direct excitation to the lowest energy $^1\pi\sigma^*$

state resulting in rapid N–H bond fission, the time scale for which we explore in greater detail in section 5.3.2.

We also consider the origins of the low KE feature, which displays a Boltzmann-like profile peaking at ~2000 cm^{-1}. Previously, King et al. provided two viable possibilities for the formation of low KE H-atoms from photoexcited pyrazole. [19] (i) Following excitation to the $1^1A''$ state, reactive flux can travel along this repulsive surface toward the $^1\pi\sigma^*/S_0$ CI, where the wave packet may bifurcate and nonadiabatically couple back into a vibrationally excited ground X^1A' state. Vibrational energy redistribution into modes that can promote N–H fission then results in statistical unimolecular decay from X^1A', producing H-atoms with low KE. (ii) Contributions from multiphoton processes were also considered, whereby absorption of multiple photons in the pyrazole parent cation could result in H-atom production. The former of these arguments may at first seem appealing, however, in general, RRKM theory provides a lower limit for unimolecular decay on the order of 10^{-9} to 10^{-10} s [40] and the TKER spectrum presented in Figure 5.3 (a) was recorded at a temporal delay of +2.5 ps; hence it is unlikely that the low KE feature in our spectrum possesses any major contributions from statistical decay pathways in the neutral pyrazole parent. This is likely to be one of the significant factors contributing to the disparity between the high-to-low KE signal ratios in the nanosecond measurements of King *et al*. [19] and our data, as highlighted in the paragraphs at the beginning of section 5.3.1. Alternatively, in previous work on phenol-d_5 [41] and imidazole derivatives [16] we have postulated that low KE H-atoms may contain signal components associated with excited state radical product channels. On the basis of energy differences between the ground ($\tilde{X}$) and first excited ($\tilde{A}$) states of the radical cofragments and interpretations of β_2 at low KEs, we suggested that in phenol-d_5 this may well be the case, whereas for imidazole this argument was

significantly less clear-cut. In pyrazole the energy separation between the $1^1A''$ state ($\tilde{X}^2A_2$ radical products) and ground X^1A' state ($\tilde{B}^2B_2$ radical products) asymptotes is calculated to be ~2000 cm^{-1}, [19, 21] suggesting that H-atoms correlated with $\tilde{B}^2B_2$ pyrazolyl radicals would appear as a low energy shoulder on the high KE feature, centered at ~7800 cm^{-1}. Not only do we not observe such a feature within the energy resolution of our experiment, tentatively suggesting an absence of adiabatic dynamics at the $^1\pi\sigma^*/S_0$ CI, but also these H-atoms would be far too energetic to account for the low KE signal peaked at 2000 cm^{-1}. With the above arguments in mind, we therefore hypothesize that multiphoton processes in the parent cation are the most feasible cause of these low energy H-atoms, and the time constant we extract from the low KE H^+ transients in section further supports this interpretation.

5.3.2 H^+ Transients and N–H Dissociation Dynamics [31]

Normalized transients for both the low and high KE H^+ signals are displayed in Figure 5.4 (a), (b), respectively, over the delay range −0.5 to +1 ps (circles). These time-resolved signal traces were obtained by recording TKER spectra (derived from H^+ images) at multiple pump–probe delays and integrating the signal in the low and high KE features over defined KE windows (200–1000 and 8000–11 500 cm^{-1}, respectively). The error bars displayed in Figure 5.4 correspond to a 95% confidence limit correlating to two standard deviations of the mean signal values. Before $\Delta t = 0$ (negative pump–probe delays) both transients display an absence of H^+ pump–probe signal, while around $\Delta t = 0$ there is a noticeable signal increase in both features. Notably, the low KE transient displays a pronounced spike in signal at $\Delta t = 0$, which then appears to rapidly decay. Upon increasing the pump–probe delay to $\Delta t \geq 500$ fs, the signal in

both plots has plateaued within the error bars, suggesting that the H-atom dissociation dynamics in pyrazole are occurring on ultrafast time scales of less than 500 fs for both features.

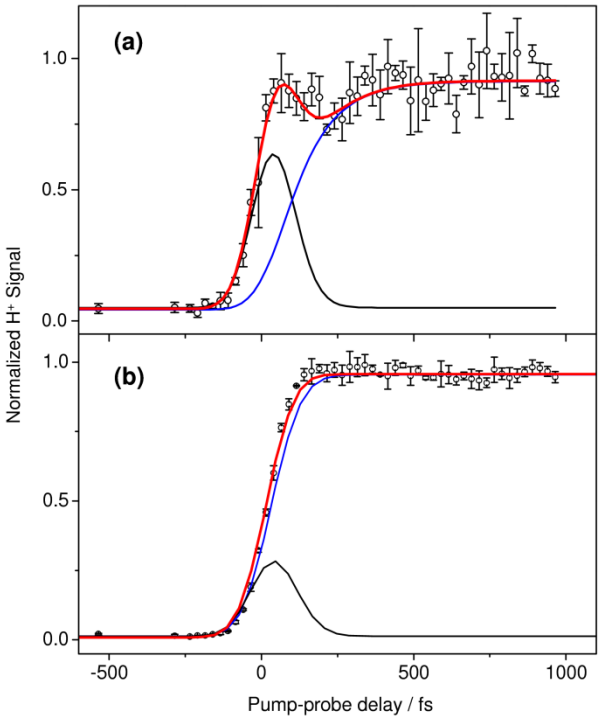

Figure 5.4 H^+ transients as a function of pump (200 nm)–probe (243.1 nm) delay for low and high KE components, (a) and (b), respectively, in pyrazole. Experimental data in (a) and (b) were fitted with a decay function (black line) and an exponential step function (blue line) convolved to the IRF giving time constants, τ, for the low (τ_L) and high (τ_H) KE components of (a) $\tau_L = 112 \pm 34$ fs and (b) $\tau_H < 50$ fs, respectively (red line). In both cases, the decay function had a time constant of $\tau_D < 50$ fs.

To extract a time constant for H-atom yield in the low KE feature, the transient signal in Figure 5.4 (a) is fitted to the sum of an exponential decay and rise, convolved with a Gaussian instrument function, $g(t)$, which accounts for our IRF of 160 fs. This fit function, $f(t)$, is formally described as

$$f(t) = g(t)^{*}\left[\left(A\exp\left(-\frac{t}{\tau_{\mathrm{D}}}\right)\right) + \left(1 - B\exp\left(-\frac{t}{\tau_{\mathrm{L}}}\right)\right)\right] \quad (2)$$

where *A* and *B* are the amplitudes of the exponential decay and rise, respectively, *t* is the pump–probe time delay, τ_L is the rise time constant for the low KE feature, and τ_D is the decay time constant. The result of this fit is shown as a solid red line through the experimental data in Figure 5.4 (a), and we extract time constants of $\tau_L = 112 \pm 34$ fs and $\tau_D < 50$ fs. The latter of these accounts for the spike in measured H^+ around $\Delta t = 0$, and the decay function (solid black line in Figure 5.4 (a) that models this signal artifact implies that it rapidly decays on a time scale significantly faster than the temporal resolution of our experiment. The limit of our temporal resolution is ~50 fs; [42] hence we quote $\tau_D < 50$ fs for the decay component of the fit. The intensity of this signal spike is noticeably sensitive to the fluences of the pump and probe pulses and decreases as the laser power is reduced. As a result, and due to its rapid decay, we attribute this signal increase around $\Delta t = 0$ to multiphoton ionization processes mediated by both pump and probe photons via the parent pyrazole cation. The remaining component of the fit, an exponential step function (solid blue line in Figure 5.4 a), generates a time constant of $\tau_L = 112 \pm 34$ fs, implying that the H-atom formation dynamics for the low KE feature are indeed direct (i.e., multiphoton). This τ_L value is concurrent with our postulate in section 5.3.1, which attributed the origins of the low KE H-atoms to multiphoton processes in the pyrazole cation, rather than statistical unimolecular decay from a vibrationally hot S_0 state in neutral pyrazole. We do, however, highlight that experiments are currently underway to investigate the role, if any, that statistical decay pathways have on H-atom elimination dynamics over significantly longer time scales (up to 600 ps) in both pyrazole and its structural isomer imidazole.

To fit the transient for the high KE feature, we first turn our attention to the TKER spectrum in Figure 5.3 (a). The Boltzmann and Gaussian fit functions that have been used to model the measured H-atom TKER profile show that there is a significant contribution of signal from the high energy tail of the low KE feature into the high KE feature. This is also true of the TKER spectra recorded around $\Delta t = 0$ (not presented), which, on the basis of integration of both the Boltzmann and Gaussian fits over the high KE feature (8000–11 500 cm^{-1}) around $\Delta t = 0$, suggests an ~35–40% contribution of the low KE feature into the integrals of the high KE peak at very early pump–probe delays. As such, the H^+ signal spike observed at $\Delta t = 0$ in the low KE transient may contribute to the integrated signal for the high KE feature. Although this is not immediately apparent in the experimental transient displayed in Figure 5.4 (b) (circles), upon increasing the pump and probe fluences (not shown), this undesired feature does indeed become much more pronounced. Therefore, fitting to the high KE transient is also performed using eq 2, where we replace the term τ_L with the appearance time constant for the high KE component, τ_H. Due to the sensitivity of the fitting procedure to the initial free input parameters, we utilize the same decay time constant, τ_D, obtained from the fit to the time-resolved signal of the low KE feature. This results in a reduction of the number of free parameters and a more localized sampling of phase space in our fitting procedure, helping to more readily extract a value for τ_H by reducing fit convergence problems. We justify this by noting that the exponential decay component in the high KE feature is likely to have the same photophysical origin as the decay feature in the low KE transient and hence exhibit the same temporal decay profile. The outcome of the fit (solid red line, Figure 5.4 (a) yields a value of τ_H which, like the decay component, is also <50 fs, implicating an exceptionally fast H-atom dissociation mechanism. As with the fits to the low KE transient, the individual rise and decay components of the overall fit are shown by

the blue and black lines in Figure 5.4 (b), respectively. The fit gives rise to a convolved decay function amplitude that is approximately ~38% of the amplitude of the rise component, in accordance with the integral ratios from the statistical and Gaussian fits to the TKER spectra around $\Delta t = 0$ (~35–40%).

The time constant obtained for H-atom yield in the high KE signal is commensurate with direct, rather than indirect, population transfer to the repulsive $1^1A''$ state followed by ultrafast H-atom elimination. Although we cannot provide an accurate quantitative value for the time scale of N–H dissociation along the $1^1A''$ surface within the temporal resolution of our measurements, we may at least add some additional weight to our finding from the high KE H^+ transient that this process will occur in <50 fs. This is achieved using a relatively simple classical model. On the basis of the known TKER of the high KE H-atoms (~9800 cm^{-1}), one may determine their average dissociation velocity (~15 250 m s^{-1}), and by making a conservative estimate of the N–H nuclear separation at which it becomes feasible to detect neutral H (5 Å), the H-atom recoil velocity can subsequently be used to obtain an estimate of ~30 fs for direct N–H bond fission via the $1^1A''$ state. It should be highlighted that this model requires a barrierless dissociation pathway along the $1^1A''$ state, an assumption supported by the near barrierless potential energy profile calculated for this state by Ashfold and co-workers. [19] In light of this, the calculation corroborates the observation from our experimental fit that, following direct $1^1A'' \leftarrow X^1A'$ excitation, bond rupture along the $1^1A''$ surface does indeed occur on a time scale faster than 50 fs.

To close this section, we briefly draw a comparison between the time scales for N–H dissociation along the lowest energy $^1\pi\sigma^*$ state observed here in pyrazole, following photoexcitation at 200 nm, and those we have previously reported in its structural isomer, imidazole, at the same

excitation energy. [16] In imidazole, the adiabatic origin of the $1^1A''$ surface (~247 nm) [15, 19] lies significantly lower in energy than in pyrazole (~214 nm), [19] whereas the onset of the optically bright $2^1A'$ state remains approximately iso-energetic in both species (~220 nm). [15, 19] A direct consequence of this is that, unlike the aforementioned dynamics in pyrazole, photoexcitation at 200 nm in imidazole results in the population of the $2^1A'$ PES rather than the repulsive $1^1A''$ state, which is supported by both our previous studies [16] and the work of Devine *et al*. [15] through a rigorous analysis of the extracted β_2 parameters. Insight from theory then suggests that vibronic coupling along appropriate in- and out-of-plane ring distortion modes facilitate efficient $2^1A' \rightarrow 1^1A''$ IC, [17] thus indirectly transferring reactive flux onto the $1^1A''$ surface, which may then lead to rapid N–H dissociation. This is in stark contrast to the direct $1^1A'' \leftarrow X^1A'$ excitation observed here and, as one may anticipate, leads to a measurably slower time scale for N–H fission of ~80 fs in imidazole at 200 nm. [16] As the imidazole time constant incorporates two ultrafast processes ($2^1A' \rightarrow 1^1A''$ IC and $1^1A''$ mediated N–H fission), we are unfortunately unable to directly extract an isolated time scale for the latter bond fission mechanism along the $1^1A''$ surface, which is analogous to the direct process observed in pyrazole, but suffice it to say that this process must occur in <80 fs. Use of a simple classical dissociation model, like that described above, implies that in imidazole N–H bond rupture along the $1^1A''$ state will also generate H-atoms in <50 fs, owing to the qualitatively similar topography of the repulsive $1^1A''$ surfaces in both pyrazole and imidazole [19] (highlighted by the similar H-atom TKER for their high KE features of 9800 cm^{-1} and 9500 cm^{-1}, [16] respectively). In an effort to verify this, experiments are currently planned to directly pump the $1^1A''$ manifold in imidazole close to its adiabatic origin.

5.3.3 Investigation of Photofragmentation Dynamics Using Time-Resolved Ion Yield

As previously emphasized, the $2^1A'$ and $1^1A''$ states of pyrazole are both transition dipole allowed and energetically accessible following 200 nm photoexcitation. Dynamics of H-atom elimination after direct excitation of the $1^1A''$ ($^1\pi\sigma^*$) manifold has been described in the previous two sections. Here we explore potential pathways arising from $2^1A'$ ($^1\pi\pi^*$) excitation. Specifically, we are interested in crossings from the $2^1A'$ state to a multitude of ring deformation pathways that may involve ring-puckering and ring-opening modes. High level ab initio calculations have yet to fully detail the ring deformation modes or the associated dynamics for pyrazole. However, the $2^1A' \rightarrow$ ring deformation $\rightarrow$ photofragment path is assumed here on the basis of analogy with the related heterocycle imidazole. [17] TRIY measurements are utilized to explore this mechanism by directly observing the dynamics of individual fragments appearing in our mass spectrum.

Results of TRIY studies using 1 μJ/pulse of 200 nm and 3.5 μJ/pulse of 243.1 nm are presented in Figure 5.5 where the ion mass spectra are shown at the left for two pump–probe delays: $\Delta t = 0$ (Figure 5.5 a) and $\Delta t = 500$ fs (Figure 5.5 b). At $\Delta t = 0$, seven primary peaks are identified, corresponding to m/z = 69, 68, 41, 40, 28, 17, and 14. The dominant pyrazole ion ($C_3H_4N_2^+$) lies at m/z = 68, with fragmentation products at m/z = 41, 40, 28, and 14 assigned as $C_2H_3N^+$, $C_2H_2N^+$, CH_2N^+, and CH_2^+, respectively. The m/z = 69 peak height is ~5% of the m/z = 68 peak and can therefore be attributed to an isotope effect in pyrazole. The m/z = 17 peak is due to remnants of NH_3, which is used for calibration as discussed in section 5.3.2. Analysis of these two peaks (m/z = 69 and 17) is not discussed further. Figure 5.5 (b) shows the mass spectrum recorded at $\Delta t = 500$ fs where the horizontal intensity scale is reduced by 20 times from that in Figure 5.5 (a). A pattern similar to that at $\Delta t = 0$ fs is observed with two immediately noticeable

differences: (i) the pyrazole parent peak intensity is greatly suppressed relative to the fragment intensities, and (ii) minor contributions to the overall mass spectrum are evident at m/z = 67, 66, 39, 38, 27, 26, 13, and 1. The first observation indicates that pyrazole does indeed undergo some fast dynamics within 500 fs, leading to molecular fragments that persist after 500 fs. Peaks at m/z = 67 and 1 are assigned to the pyrazolyl ($C_3H_3N_2^+$) and H^+ ions, respectively. Appearance of these peaks is due to direct H-atom dissociation via the repulsive $1^1A''$ state, as described in sections 5.3.1 and 5.3.2. Peaks at m/z = 66, 39, 38, 27, 26, and 13 are attributed to additional H-atom loss from the primary fragmentation peaks assigned above. Time profiles obtained for these transients suffer from poor signal-to-noise and reliable temporal fits could not be obtained. Analysis of fragmentation dynamics will therefore focus on the primary peaks only.

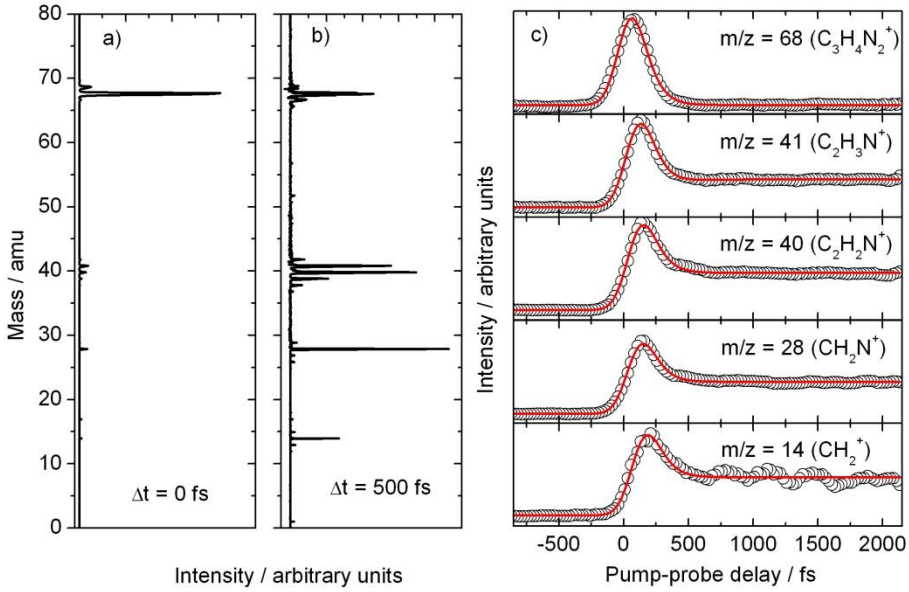

Figure 5.5 Results of TRIY experiments on pyrazole using 200 nm excitation (pump) and 243.1 nm ionization (probe) wavelengths. Photofragmentation mass spectra are shown on the left for Δt = 0 fs (a) and Δt = 500 fs (b). The horizontal intensity scale in (b) is enhanced by 20 times from (a) to highlight the fragmentation pattern. Intensities of the primary peaks at m/z = 68, 41, 40, 28, and 14 are shown as a function of pump–probe delay in (c). Fits (red lines) of these time profiles are used to extract dynamics of a $^1\pi\pi^*$ → ring deformation → photofragment relaxation channel, as described in the text.

With the pump and probe power levels used here, multiphoton one-color ionization of pyrazole is only minimal. While the exact molecular structure of each fragment is not determined here, the

ionization potential (IP) of possible ground state $C_xH_yN_z$ structures is in the 9–12 eV range. [43] Therefore, one-photon ionization of ground state fragments is also unlikely at our chosen probe photon energy (~5.1 eV), and one-photon ionization of excited state fragments is considered the most likely source of the observed *m*/*z* peaks.

The intensity ratio, I_F/I_P, is obtained by dividing the fragment peak height, I_F, at Δt = 500 fs by the parent peak height, I_P, at Δt = 0 fs, and is reported in Table 5.1. Fragment peaks are 1.8–5.7% of the parent peak height, suggesting that pyrazole preferentially relaxes along a pathway that does not lead to excited state fragments. In the related heterocycle pyrrole, 4–13% of relaxation trajectories are predicted to go through ring deformation modes (here, ring-puckering [26, 27] and ring-opening [26]), which at the CI with S_0 can either fragment or return to the vibrationally hot ground state. Similarly, in imidazole, theory predicts 16% of the trajectories proceed along the ring-puckering and 1% along the ring-opening pathway. [44] Our results suggest that $2\,^1A' \rightarrow$ ring deformation relaxation is a minor pathway in pyrazole and that dissociation of the ring deformed molecule can lead to a minor fraction of the fragments being formed in excited states.

Table 5.1. Summary of the Photo-Fragmentation Assignments and Their Associated Dynamics Extracted from the Temporal Fits Displayed in Figure 5.6 c[a]

m/*z*	Assignment	τ_R / fs	I_F/I_P
41	$C_2H_3N^+$	161	0.036
40	$C_2H_2N^+$	80	0.046
28	CH_2N^+	95	0.057
14	CH_2^+	54	0.018

a) Values for the exponential decay times, τ_D, and the start time for the exponential rise, t_R, used in the fits are both fixed at 87 fs for all fragment transients, on the basis of fits to the parent ion transient, m/z = 68 (see eq 2 and text for fit details). τ_R is the exponential rise time constant, and I_F/I_P is the ratio of each photo-fragment intensity at Δt = 500 fs, I_F, to the parent ion signal at Δt = 0 fs, I_P.

It is important to note here that the intensity of the H^+ (m/z = 1) peak in Figure 5.6 (b) cannot be used to infer that H-atom dissociation via the dissociative $1^1A''$ surface is a minor relaxation pathway. The method of H-atom detection is 2 + 1 REMPI and will possess a smaller ionization cross-section than one-photon ionization of excited state fragments. In fact, $1^1A''$ mediated relaxation, as described in the previous sections, is generally considered to be the main pathway for the structural isomer imidazole, with a predicted yield of around 83% at 200 nm. [44]

To investigate fragmentation dynamics, we present time profiles for the primary m/z peaks in Figure 5.5 (c). The data (white circles) in these time profiles are obtained by integrating a gate set over each peak for the entire pump–probe delay range ($-850 \leq \Delta t \leq 2150$ fs). Time profiles for all fragments are qualitatively similar, including the minor fragments, which are not shown. However, the parent and fragment time traces are noticeably different in that the fragments level off to a constant nonzero value after ~500 fs, whereas the parent returns to nearly zero intensity at this time. Two different fitting routines are therefore used for the parent and for the fragment traces. Fits are shown as red lines in Figure 5.5 (c) and relevant fit parameters are compiled in Table 5.1.

Attempts to fit the pyrazole parent trace with the Gaussian IRF (fwhm ~225 fs) alone results in underestimation of signal intensity in the $0 < \Delta t < 300$ fs range. Thus, the m/z = 68 trace is fit

with a single exponential decay function convoluted with the IRF. The exponential decay time obtained from this fit, τ_D = 87 ± 40 fs, corresponds to the average excited state lifetime of pyrazole, including relaxation from both the initially excited $2^1A'$ and $1^1A''$ states. Because the ratio of the initial population transfer into these states is unknown, this lifetime cannot be detailed further. With the aid of high level quantum calculations this may be possible, although such detailed calculations are beyond the scope of the work presented here.

Primary fragment (m/z = 41, 40, 28, and 14) time profiles (Figure 5.5 c) display a peak near Δt = 0 and then plateau for $\Delta t \geq 500$ fs and can be fit with the sum of independent exponential decay and rise functions convoluted with the IRF. The fit equation is very similar to the H-atom transient fit equation (eq 2) but is modified by the introduction of separate start times for the rise, t_R, and decay, t_D, functions. With reference to eq 2, there are then six free parameters in our fitting equation, t_R, t_D, τ_D (decay time constant), τ_R (rise time constant), A (decay amplitude), and B (rise amplitude), of which two are constrained by the pyrazole parent fit. The peak in the fragment traces around Δt = 0 is due to dissociative ionization of pyrazole, whereby fragmentation occurs in the parent cation. The decay time for this peak is then fixed at τ_D = 87 fs, corresponding to $2^1A'$ state decay in the pyrazole parent. The start of the decay function is offset from Δt = 0 by 50–100 fs, which is accounted for by t_D. As mentioned previously, the rise of the fragment profiles should begin subsequent to the decay of the parent into ring deformation modes. We therefore fix t_R = 87 fs and allow τ_R, which can be interpreted as the time it takes fragmentation to occur following relaxation through ring deformation modes, to be fit. Values for τ_R are in the 54–161 fs range and are reported with an error of ±40 fs (with larger ±50 fs error for m/z = 14, due to poor signal-to-noise) in Table 5.1. The errors reported for all fits are

estimated from the range of values obtained from different starting parameters during fit convergence.

The photofragmentation dynamics have been extracted directly from the evolution of mass spectra as a function of pump–probe delay. From our data, we propose that fragmentation of the ring involves $2^1A' \rightarrow$ ring deformation $\rightarrow$ photofragmentation, an interpretation based on recent calculations on the structural isomer imidazole, as summarized here. The $2^1A'$ state of pyrazole is directly populated by 200 nm absorption and excited state flux crosses into various ring deformation pathways within 87 fs. In general, at the CI with S_0 ($^1\pi\pi^*/S_0$) ring deformation modes can either relax to a vibrationally hot ground state or continue along the ring deformation pathway toward fragmentation. Our results show that some excited state trajectories do lead to fragmentation, thereby leaving some fragments in an electronically excited state. Once flux is coupled into ring deformation modes, excited state fragments appear within 160 fs.

5.4 Conclusions

Using a combination of TR-VMI [31] and TRIY studies, we have investigated the excited state dynamics of pyrazole following photoexcitation at 200 nm. The measurements presented show that both N–H dissociation and ring fragmentation pathways contribute to the excited state dynamics. The N–H dissociation pathway has been studied using TR-VMI and has identified both low (statistical) and high (Gaussian) KE H-atoms with appearance times of $\tau_L = 112 \pm 34$ fs and $\tau_H < 50$ fs, respectively. Measurements of H-atom recoil anisotropy coupled with these appearance time scales allow us to associate low and high KE features to multiphoton processes in the pyrazole cation and direct dissociation along the lowest energy $^1\pi\sigma^*$ ($1^1A''$) surface, respectively. In competition with N–H dissociation, ring fragmentation leading to excited state

fragments also occurs on an ultrafast time scale. TRIY measurements provide time constants for the appearance of excited state fragments that are all within 160 fs. We propose that these photofragments are produced through a sequential two-step mechanism: $^1\pi\pi^*$ ($2^1A'$) → ring deformation → photofragmentation, a model based on analogy with imidazole calculations. While these measurements cannot provide precise quantum yields for the different relaxation pathways, the faster $^1\pi\sigma^*$ driven N–H dissociation may suggest that ring deformation pathways are likely out-competed by $^1\pi\sigma^*$ driven N–H dissociation and hence ring fragmentation does not lead to the dominant kinetic photoproduct.

5.5 References

[1] C. E. Crespo-Hernandez, B. Cohen, P. M. Hare, and B. Kohler, *Chem. Rev.*, 2004, 104, 1977.

[2] P. R. Callis, In Methods Enzymol.; *Academic Press*: New York, 1997; Vol. 278, p 113.

[3] M. N. R. Ashfold, G. A. King, D. Murdock, M. G. D. Nix, T. A. A. Oliver, and A. G. Sage, *Phys. Chem. Chem. Phys.*, 2010, 12, 1218.

[4] A. L. Sobolewski, W. Domcke, C. Dedonder-Lardeux, and C. Jouvet, *Phys. Chem. Chem. Phys.*, 2002, 4, 1093.

[5] C. M. Tseng, Y. T. Lee, M. F. Lin, C. K. Ni, S. Y. Liu, Y. P. Lee, Z. F. Xu, and M. C. Lin, *J. Phys. Chem. A,* 2007, 111, 9463.

[6] C. M. Tseng, Y. T. Lee, C. K. Ni, and J. L. Chang, *J. Phys. Chem. A,* 2007, 111, 6674.

[7] M. N. R. Ashfold, B. Cronin, A. L. Devine, R. N. Dixon, and M. G. D. Nix, *Science*, 2006, 312, 1637.

[8] A. Iqbal and V. G. Stavros, *J. Phys. Chem. A,* 2010, 114, 68.

[9] K. L. Wells, D. J. Hadden, M. G. D. Nix, and V. G. Stavros, *J. Phys. Chem. Lett.*, 2010, 1, 993.

[10] A. Iqbal and V. G. J. Stavros, *J. Phys. Chem. Lett.*, 2010, 1, 2274.

[11] A. Stolow, A. E. Bragg, and D. M. Neumark, *Chem. Rev.*, 2004, 104, 1719.

[12] S. Ullrich, T. Schultz, M. Z. Zgierski, and A. Stolow, *Phys. Chem. Chem. Phys.*, 2004, 6, 2796

[13] H. Satzger, D. Townsend, M. Z. Zgierski, S. Patchkovskii, S. Ullrich, and A. Stolow, *Proc. Natl. Acad. Sci. U. S. A.*, 2006, 103, 10196.

[14] N. L. Evans and S. Ullrich, *J. Phys. Chem. A*, 2010, 114, 11225.

[15] A. L. Devine, B. Cronin, M. G. D. Nix, and M. N. R. Ashfold, *J. Chem. Phys.*, 2006, 125, 184302.

[16] D. J. Hadden, K. L. Wells, G. M. Roberts, L. T. Bergendahl, M. J. Paterson, and V. G. Stavros, *Phys. Chem. Chem. Phys.*, 2011, 13, 10342.

[17] M. Barbatti, H. Lischka, S. Salzmann, and C. M. Marian, *J. Chem. Phys.*, 2009, 130, 034305

[18] T. Eicher and S. Hauptmann, The Chemistry of Heterocycles: Structure, Reactions, Syntheses, and Applications. 2nd ed.; *Wiley-VCH*: Berlin, Germany, 2003.

[19] G. A. King, T. A. A. Oliver, M. G. D. Nix, and M. N. R. Ashfold, *J. Chem. Phys.*, 2010, 132, 064305.

[20] I. C. Walker, M. H. Palmer, M. J. Hubin-Franskin, and J. Delwiche, *Chem. Phys. Lett.*, 2003, 367, 517.

[21] T. Ichino, A. J. Gianola, W. C. Lineberger, and J. F. Stanton, *J. Chem. Phys.*, 2006, 125, 084312.

[22] M. H. Palmer and A. Beveridge, *J. Chem. Phys.*, 1987, 111, 249.

[23] M. H. Palmer and M. F. Guest, *Chem. Phys.*, 2003, 291, 287.

[24] S. Matsika and D. R. Yarkony, *J. Am. Chem. Soc.*, 2003, 125, 12428.

[25] M. S. Schuurman and D. R. Yarkony, *J. Chem. Phys.*, 2008, 129, 064304.

[26] M. Vazdar, M. Eckert-Maksic, M. Barbatti, and H. Lischka, *Mol. Phys.*, 2009, 107, 845.

[27] M. Barbatti, J. Pittner, M. Pederzoli, U. Werner, R. Mitric, V. Bonacic-Koutecky, and H. Lischka, *Chem. Phys.*, 2010, 375, 26.

[28] M. Barbatti, M. Vazdar, A. J. A. Aquino, M. Eckert-Maksic, and H. Lischka, *J. Chem. Phys.*, 2006, 125, 164323.

[29] A. D. Blank, S. W. North, and Y. T. Lee, *Chem. Phys.*, 1994, 187, 35.

[30] A. J. van den Brom, M. Kapelios, T. N. Kitsopoulos, N. H. Nahler, B. Cronin, and M. N. R. Ashfold, *Phys. Chem. Chem. Phys.*, 2005, 7, 892.

[31] C. A. Williams, G. M. Roberts, H. Yu, N. L. Evans, S. Ullrich, and V. G. Stavros, J. Phys. Chem. A, 2012, 166, 2600.

[32] K. L. Wells, G. Perriam, and V. G. Stavros, *J. Chem. Phys.*, 2009, 130, 074304.

[33] U. Evan, J. Jortner, D. Noy, N. Lavie, and C. Cossart-Magos, *J. Chem. Phys.*, 2000, 112, 8068.

[34] A. T. J. B. Eppink and D. H. Parker, *Rev. Sci. Instrum.*, 1997, 68, 3477.

[35] G. M. Roberts, J. L. Nixon, J. Lecointre, E. Wrede, and J. R. R. Verlet, *Rev. Sci. Instrum.*, 2009, 80, 053104.

[36] B. J. Whitaker, "Imaging in Molecular Dynamics: Technology and Applications", *Ed.; Cambridge University Press: Cambridge, UK*, 2003.

[37] P. M. Regan, S. R. Langford, A. J. Orr-Ewing, and M. N. R. Ashfold, *J. Chem. Phys.*, 1999, 110, 281.

[38] A. J. Gianola, T. Ichino, S. Kato, V. M. Bierbaum, and W. C. Lineberger, *J. Phys. Chem. A*, 2006, 110, 8457.

[39] R. N. Zare, "Angular Momentum: Understanding Spatial Aspects in Chemistry and Physics", *Wiley: New York*, 1988.

[40] K. A. Holbrook, M. J. Pilling, and S. H. Robertson, "Unimolecular Reactions", *John Wiley and sons: Chicester, UK*, 1996.

[41] A. Iqbal, M. S. Y. Cheung, M. G. D. Nix, and V. G. Stavros, *J. Phys. Chem. A*, 2009, 113, 8157.

[42] D. J. Hadden, C. A. Williams, G. M. Roberts, and V. G. Stavros, *Phys. Chem. Chem. Phys.*, 2011, 13, 4494.

[43] http://webbook.nist.gov/chemistry/

[44] M. Barbatti, personal communication.

CHAPTER 6

EXCITED STATE DEACTIVATION PATHWAYS OF PYRROLE STUDIED BY TIME-RESOLVED ION YIELD AND TOTAL KINETIC ENERGY RELEASE[4]

[4] To be submitted to JPCA.

6.1 Abstract

Time-resolved ion yield and total kinetic energy release spectroscopies have been applied to study the relaxation dynamics in pyrrole following photoexcitation at 240, 217.5, and 200 nm to the lowest electronically excited states of $\pi\sigma^*$ and $\pi\pi^*$ character. At all excitation wavelengths, NH-dissociation on the $\pi\sigma^*$ (1^1A_2) state yields high kinetic energy H atoms and ground state pyrrolyl photoproducts on timescales of <100 fs. Low kinetic energy H atoms observed at 217.5 and 200 nm, are suggestive of formation of pyrrolyl in its first excited state *via* the higher lying $\pi\sigma^*$ (2^1B_1) state. Ring deformation pathways, associated with the $\pi\pi^*$ (1^1B_2) state, compete with the NH-stretching mechanism at these shorter wavelengths and yield photofragments of intermediate masses within < 400 fs.

6.2 Introduction

Pyrrole, a simple five-membered heterocyclic molecule, is found as a subunit in biomolecules such as tryptophan, porphyrin, and chlorophyll. Spectroscopic investigations of this prototype molecule therefore provide an initial starting point in an overall endeavor towards understanding the ultraviolet (UV) photostability of larger biomolecules. The goal of the present work is to characterize major photo-fragmentation processes in pyrrole upon UV irradiation.

The UV absorption spectrum of pyrrole is characterized by a broad first absorption band covering the 190 to 225 nm wavelength range with superimposed narrow Rydberg transitions and a weak tail extending to 270 nm. A number of low-lying, vibronically coupled states contribute to the spectrum which poses a challenge to theory and at present the energetic ordering of states remains under debate. [1 – 5] In general, the majority of intensity of the first band has been attributed to the bright $\pi\pi^*$ (1^1B_2) transition with adiabatic onset around 217 nm

and only minor contributions from $\pi\pi^*$ (2^1A_1). A narrow peak at 211 nm is assigned to the $\pi 3p_y$ (1^1B_1) Rydberg transition, while weak absorbance at longer wavelengths has been associated with the optically forbidden, but vibronically induced $\pi\sigma^*$ (1^1A_2) transition. [3, 6] This assignment has been challenged by recent quantum dynamics calculations by Neville *et al*. [5] who reinterpret the 217 nm intensity mainly as $\pi\sigma^*$ (2^1B_1) character and place the center of the $\pi\pi^*$ (1^1B_2) transition at a significantly shorter excitation wavelength of 199 nm. Photoexcitation with 217 nm may thus result in population of the optically dark $\pi\sigma^*$ (2^1B_1) state *via* intensity borrowing from the bright $^1\pi\pi^*$ transitions, contrary to the previous assumption of direct excitation to the $\pi\pi^*$ (1^1B_2).

Similar to other five-membered heterocyclic molecules, the photochemistry of pyrrole is largely determined by dynamics involving the lowest $\pi\sigma^*$ (1^1A_2) state. Calculations by Sobolewski and Domcke [7] predict ultrafast transitions from the $\pi\pi^*$ (1^1B_2) to the $\pi\sigma^*$ (1^1A_2) surface with high probability of populating the latter state and subsequent internal conversion to the ground state (S_0) *via* a $\pi\sigma^*/S_0$ conical intersection (CI). The photodissociation rates and branching ratios along these $\pi\sigma^*$ surfaces are subsequently shown to be sensitive to mode-specific preparation of the initial state. [8, 9] Complementing this work, trajectory calculation by Barbatti *et al*. [10] suggest three deactivation pathways following UV photoexcitation in the wavelength range of 250 - 200 nm, when $\pi\sigma^*$ (1^1A_2) and $\pi\pi^*$ (1^1B_2) states are populated. Most relevant to the present study, potential photodissociation products ascribed to relaxation along these pathways are discussed. Population of the lowest $\pi\sigma^*$ (1^1A_2) state, either direct (at 248 and 243 nm) or indirect via the $\pi\pi^*$ (1^1B_2) state (at 217 nm), results in stretching of the N-H bond, leading to the formation of atomic hydrogen (H) and pyrrolyl co-fragments after crossing the $\pi\sigma^*$ / S_0 CI. H

atoms from direct dissociation along the $\pi\sigma^*$ (1^1A_2) pathway are produced with high kinetic energy (KE) and readily distinguished from low KE H atoms formed through statistical decay of the hot ground state. In the case of photoexcitation to the $\pi\sigma^*$ (1^1A_2) state at 243 nm or the $\pi\pi^*$ (1^1B_2) state at 217 nm, additional deactivation pathways are energetically accessible. These are associated with ring opening and ring puckering coordinates and lead to HCN, HCNH, C_3H_3, and C_3H_4 photofragments after crossing the $\pi\pi^*$ / S_0 CI. Alternatively, aborted dissociation and relaxation to S_0 again produces low KE H atoms from statistical decay. According to dynamics simulations initiated at the ring puckered CI precursors of larger fragments also form on the vibrationally hot ground state within less than 1 ps. [11] Branching ratios and timescales for the competing pathways have been determine from trajectory simulations in two independent studies by Vazdar *et al*. [12] and Barbatti *et al*. [13]. Following excitation to higher excited states, ring deformation pathways account for only 13% of the deactivation dynamics (10% ring puckering and 3% ring opening) compared to 80% for the N-H stretching pathway. [12] An overall time constant of 140 fs for repopulation of the ground state is extracted, and for the N-H stretching path 44 and 80 fs are specified for population and depopulation of the $\pi\sigma^*$ (1^1A_2) state, respectively. The dominance of the NH-stretching pathway has been confirmed by the second study with time constants of 20, 166, and 184 fs for excitation at 248, 212 and 193 nm, respectively, but no contributions from the ring opening pathway have been observed. [13] Competing relaxation paths and potential photofragments are summarized in the schematic (Fig. 6.1).

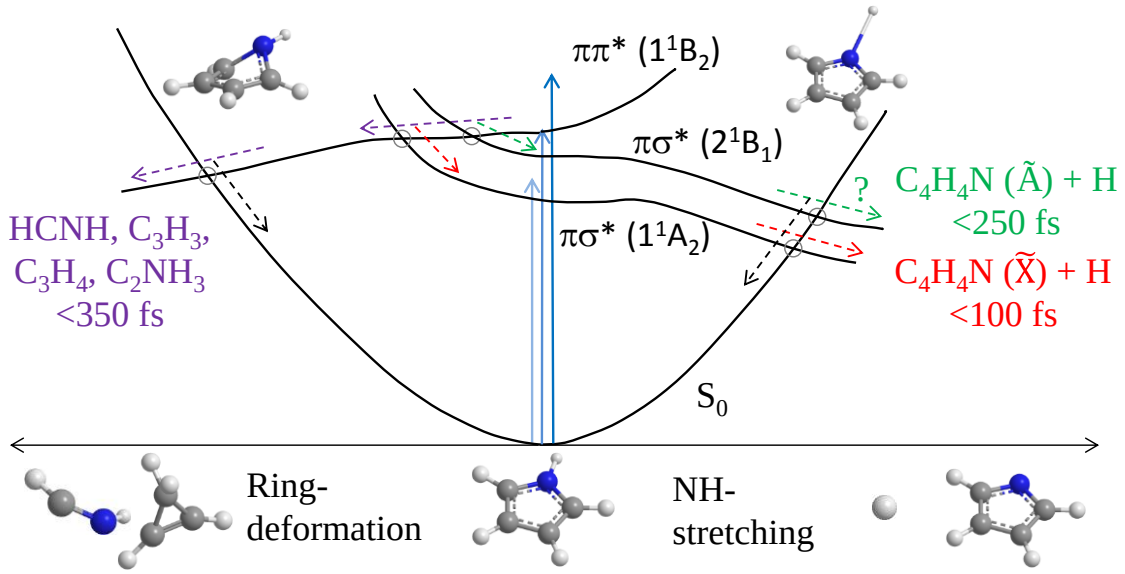

Figure 6.1. Schematic picture of competing dissociation pathways of pyrrole following excitation to the lowest electronic states of πσ* and ππ* character at three different excitation wavelengths. Photoproducts that are formed along the ring-deformation and N-H stretching pathways are indicated.

Numerous frequency- and time-resolved experiments have investigated the NH-stretching pathway(s). One-color Velocity Map Imaging (VMI) experiments of Wei *et al.* [14] at 243.15 nm present an H atom translational kinetic energy distribution, in which a dominant signal of fast (i.e. high KE) H atoms is shown, associated with rapid N-H dissociation along πσ* (1^1A_2). The study was subsequently extended to two-color experiments with 217 nm photoexcitation and to include deuterated pyrrole. [15] Most notably, this confirmed N-H, as opposed to C-H, dissociation as the main source of fast H atoms. In a comprehensive series of wavelength-dependency and deuteration studies, Ashfold and coworkers employ photofragment translation spectroscopy with photolysis in the $193.3 < \lambda_{phot} < 254.0$ nm range. [16, 17] These high resolution Total Kinetic Energy Release (TKER) spectra reveal the specific vibrational

excitations of the ground state pyrrolyl co-fragment following the N-H dissociation process and allow precise determination of the dissociation energy. Apart from fast H atoms, all studies mentioned above also observe slow H atoms associated with statistical unimolecular decay of the vibrationally hot molecule following internal conversion to the ground state.

Two-color Time-Resolved Ion Yield (TR-IY) experiments by Lippert *et al.* [18], with 250 nm excitation and 243.1 nm ionization present one of the first studies of the N-H-dissociation dynamics with femtosecond time resolution. Elimination of fast and slow H atoms was concluded based on appearance times of 0.1 and 1.1 ps, respectively, with the latter explained as internal vibrational cooling in the ground state.

In extension, Roberts *et al*. [19] used time-resolved velocity map imaging (TR-VMI) to determine the timescales of H atom elimination for direct photoexcitation of the $\pi\sigma^*$ (1^1A_2) state at 250 and 238 nm and for population of the $\pi\pi^*$ (1^1B_2) state at 200 nm. Compared to the earlier studies by Lippert *et al.*, [18] this technique provides additional KE analysis of the H atom dissociation products. Appearance times for high KE H atoms were reported as 126, 46 and 52 fs for above wavelengths, respectively, the longer time at 250 nm being associated with the extra time required to tunnel through an exit barrier. Low KE H atoms observed only at 200 nm excitation indicate the energetic onset for statistical unimolecular decay on the hot ground state, and a rise time of 1 ns was extracted.

A limited number of studies have investigated the photofragmentation of pyrrole into larger products. Of particular note are multi-mass experiments by Blank *et al*. [20] who employ

photofragment translational spectroscopy techniques to examine photodissociation products that form upon 248 and 193 nm excitation. Analysis of fragment translational energy profiles provides them with the means to distinguish between processes occurring on the neutral ground and electronically excited states. In summary, their work identifies five dissociation pathways following 193 nm excitation that correspond to excited state N-H dissociation (30%), and statistical decay following internal conversion to the ground state, including N-H dissociation (21%), NH elimination (≈0.2%), and two channels resulting in HCN formation (24% and 25%). For excitation at 248 nm, H atom elimination is the only fragmentation process. Specifically, both N-H (47%) and C-H (11%) fission is observed to occur from the excited state whereas on the ground state dissociation is limited to the N-H bond (42%). Fragmentation of the cationic state has also been investigated. Photoabsorption and time-of-flight mass spectrometry studies [21] revealed main fragments in the photon energy range of 11 – 13 eV as $C_2NH_3^+$, $C_3H_4^+/C_2NH_2^+$, $C_3H_3^+/C_2NH^+$ and CNH_2^+, whose appearance energies were measured to be <11.81, 12.31, 12.61 and 12.31 eV, respectively. Using mass spectrometry in combination with photoelectron imaging, van den Brom *et al.* [22] performed multi-photon ionization and dissociation experiments at 243 and 364.7 nm. Major fragments at m/z = 1, 12, 24, 28, 39 and 67 were observed at both wavelengths and assigned to H^+, C^+, C_2^+, CNH_2^+, $C_3H_3^+$ and $C_4H_5N^+$, respectively. An additional C_3^+ ion peak was only present at 243 nm excitation. The C^+, C_2^+, and C_3^+ ions were proposed to originate from secondary, cationic fragmentation of $C_3H_3^+$ and CNH_2^+ upon absorption of additional photons.

In this work TR-IY and time-resolved total kinetic energy release (TR-TKER) studies of pyrrole at 240, 217.5 and 200 nm excitation are employed to investigate the deactivation dynamics along

competing ring deformation and N-H stretching paths. Mass spectra are analyzed for fragmentation patterns and appearance timescales of photoproducts associated with these pathways are extracted. Excitation wavelengths are chosen to access three distinct regions of the pyrrole absorption spectrum. Excitation at 240 nm leads to the $\pi\sigma^*$ (1^1A_2) state with the N-H stretching pathway as the only route for non-radiative deactivation. Shorter wavelengths of 217.5 and 200 nm access the $\pi\pi^*$ (1^1B_2) state where additional ring deformation pathways become available. In light of the reinterpretation of the absorption spectrum by Worth and co-workers, [10] population of the $\pi\sigma^*$ (2^1B_1) *via* intensity borrowing from nearby $\pi\pi^*$ states is also considered. This latter case is exclusively associated with an N-H stretching channel.

6.3 Experiment

A femtosecond laser system with UV conversion capabilities, continuous-expansion molecular beam source, a magnetic bottle energy spectrometer, and a time-of-flight (TOF) mass spectrometer form the main components of the experimental set up, which has been described in more detail elsewhere. [23 – 28]

The laser pulses are derived from a commercially available oscillator and amplifier (Coherent Inc., MIRA Optima 900 and Legend Elite-HE). The amplifier output (1 kHz, 800 nm, 130 fs, 3.5 mJ/pulse) is split into three beams and subsequently converted to UV pump and probe pulses. The first beam is sent into a Traveling-wave Optical Parametric Amplifier of a White-light Continuum (Light Conversion, TOPAS-C) to create 240, 268 and 299 nm pulses. The 240 nm output pulse (6.8 μJ/pulse) is directly used to photoexcite pyrrole, while the 268 and 299 nm pulses undergo additional sum frequency generation with the 800 nm fundamental (second

beam) to generate 201 and 217.5 nm pulses (1.5 μJ/pulse). Probe pulses at 243.15 nm are produced from the third beam which is sent into an Optical Parametric Amplifier (Coherent Inc., OPerA). For (2+1) resonance enhanced multiphoton ionization of H atoms pulse energies are set to 12.5 μJ/pulse while larger fragments are probed with 6.8 μJ/pulse to accommodate one and two photon ionization processes. A computer controlled motorized optical delay line (Newport ILS150PP with ESP300 controller) is used to time-delay the pump and probe pulses relative to each other. Two different layouts are employed to spatially overlap and focus the pump and probe beams into the interaction region of the spectrometer. For experiments with 240 and 218 nm excitation, the pump and probe beams are combined non-collinearly and individual lenses of f = 50 cm and f = 30 cm, respectively, are used. For 200 nm excitation, the pump and probe beams are overlapped collinearly by means of a dichroic beamsplitter and focused into the interaction region with a single f = 30 cm lens. The one-color signals of the pump and probe pulses are simultaneously recorded with shutters, and subtracted from the two-color signal.

Pyrrole liquid (Sigma-Aldrich, > 98%) is contained by a piece of glass filter paper and placed in a quartz sample holder, which is heated to 30^{o}C, just before a 100 μm nozzle pinhole. The continuous gaseous pyrrole beam is coexpanded with a Helium backing gas inside the molecular beam chamber and carried to the interaction region of the spectrometer *via* an intermediate, differentially pumped stage.

A time-of-flight (TOF) mass spectrometer with Wiley-McLaren configuration [29] is employed for TR-IY experiments. TOF-to-mass conversions are carried out using NH_3 and 1,3-Butadiene

as calibration gases. The timing overlap of the pump and probe pulses and the full width at half maximum (FWHM) are determined *via* pump-probe measurements of the same calibration gases.

TKER experiments which require KE analysis of H atom dissociation products are facilitated by a magnetic-bottle spectrometer based on the design of Kruit and Read [30]. To improve collection efficiency, the photoionized H atoms are repelled with an additional electrostatic potential of +14 V applied between two grids located below and above the ionization region. TOF-to-kinetic energy calibrations are performed by monitoring the change in TOF while varying this repelling potential. For a detailed description of the procedure see Refs. 27, 28. [27, 28]

6.4 Results and Discussions

For all three excitation wavelengths discussed below, TR-IY and TR-TKER were recorded and analyzed as follows to prepare the plots presented in Figs. 6.2 – 6.7. TR-IY spectra were background subtracted to remove one-color contributions and subsequently integrated over 50 fs wide time intervals centered at Δt = -500 fs, 0 fs, and 200000 fs in order to generate mass spectra before, at, and after pump-probe timing overlap, respectively. To enlarge the fragment peaks of interest in this study all mass spectra are limited to the range of 0 to 66 amu, i.e. the dominant pyrrole parent peak has been omitted. For selected fragment peaks, time traces are extracted from the TR-IY spectra by integrating over 0.5 amu wide mass gates. TR-TKER spectra of H and pyrrolyl dissociation products are also background subtracted and further analyzed to extract steady state KE distribution by integrating a pump-probe region spanning 1 ps < Δt < 1.5 ps. Time-traces for high KE H atoms are obtained by integrating a gate placed over the feature

between 5000 – 10000 cm^{-1}, and time-traces for low KE H atoms are integrated over 300 – 3000 cm^{-1}.

6.4.1 Photoexcitation at 240 nm.

At 240 nm excitation, the $\pi\sigma^*$ (1^1A_2) state of pyrrole is directly populated with enough excess energy to surpass the exit barrier to N-H dissociation. Two-color mass spectra for time delays $\Delta t < 0$, $\Delta t = 0$, and $\Delta t > 0$ are presented in Figs. 6.2 a) - c), respectively. Inspection of the fragment pattern in Fig. 6.2 c), which corresponds to pump-induced fragmentation, reveals a dominant H mass peak at 1 amu in accord with dissociation along the neutral, excited $\pi\sigma^*$ (1^1A_2) pathway. Notably, non-zero, but much less intense H mass peaks are also observed in Fig. 6.2 a) and b) which require explanation. At probe-pump delays ($\Delta t < 0$, Fig. 6.2 a)), one photon of the 243.15 nm probe pulse excites pyrrole to the same $\pi\sigma^*$ (1^1A_2) which dissociates on timescales shorter than the pulse duration and generates neutral H atoms. Two more photons from the same probe pulse resonantly excite the neutral H fragments to the 2s level, which are subsequently ionized by one photon from the (time-delayed) pump pulse. Similar two-color, multi-photon processes were suggested by Refs. 18 and 19. [18, 19] During the cross-correlation of the pump and probe pulses ($\Delta t = 0$, Fig. 6.2 b)), both, pump-probe and probe-pump, processes contribute to the observed H signal. A peak at m/z = 66, which is present in all three mass spectra, corresponds to the pyrrolyl co-fragment associated with the same N-H dissociation process. At $\Delta t = 0$ (Fig. 6.2 b)), relatively strong signals for fragments of intermediate masses are observed due to dissociative ionization. During the cross-correlation multiphoton processes with up to two pump and three probe photons are feasible and may, in principle, yield cationic dissociation products that have appearance energies (AE) of less than ~26 eV (our maximum total photon energy).

These include, with AEs according to Rennie *et al*. [21], positively charged $C_2H_3^+$ (m/z = 27, AE = 14.63 eV), CNH_2^+ (m/z = 28, AE = 12.31 eV), C_3H^+ (m/z = 37, AE = 20.56 eV), $C_3H_2^+$ (m/z = 38, AE = 16.25 eV), $C_3H_3^+$ or C_2NH^+ (m/z = 39, AE = 12.61 eV), $C_3H_4^+$ or $C_2NH_2^+$ (m/z = 40, AE = 12.31 eV) and $C_2H_3N^+$ (m/z = 41, AE < 11.81 eV). In fact, the mass spectrum in Fig. 6.2 b) directly resembles the one by Rennie *et al*. [21] recorded with one-photon, 27.55 eV ionization. An almost identical fragment pattern is observed in the mass spectrum at $\Delta t < 0$ (Fig. 6.2 a)) and may be explained as two-photon excitation by the probe to a long-lived cationic state of pyrrole (e.g. vibrationally excited cationic ground state, but below the exit barriers to fragmentation) which is subsequently dissociated with one or two photons from the time-delayed pump. However it should be noted, that in the $\Delta t > 0$ mass spectrum (Fig. 6.2 c)) all fragments of intermediate masses are absent or negligible, indicating that the only major deactivation pathway following $\pi\sigma^*$ (1^1A_2) population proceeds along the N-H coordinate leading to either dissociation or ground state repopulation. This observation confirms dynamics simulations by Barbatti *et al*. [13] that identify the NH stretching pathway as the dominant deactivation mechanism and place the energetic onset of the minor ring deformation channel between 248 and 211 nm, or, according to Ref. 10 [10] around 243 nm.

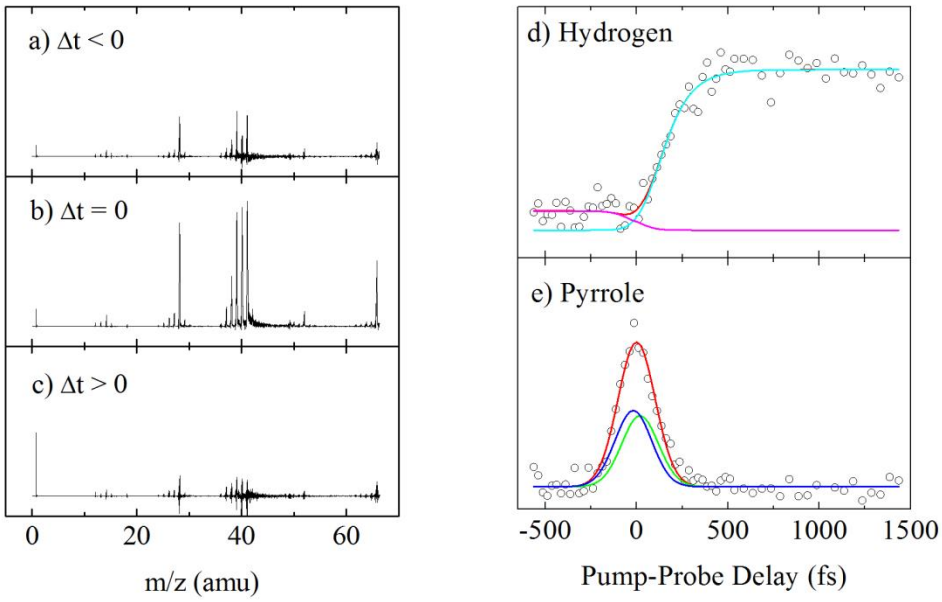

Figure 6.2 Mass spectra and transients extracted from 2d TR-IY spectra (not shown) of pyrrole following 240 nm photoexcitation are presented. Mass spectra for three integration regions corresponding to before a), at b) and after c) pump-probe timing are plotted with identical intensity scales for all three cases. Transients of atomic hydrogen d) and the pyrrole parent (e) are represented by open circles. The total fit is shown as a solid red line with individual components in different colors.

To examine the timescales of N-H dissociation, transients of H and the pyrrole parent are presented in Figs. 6.2 d) and e). The lifetime of the pyrrole parent is known from recent literature with values of 19 fs, [31] and can be used here for the purpose of timing calibration of our

measurement. By fitting forward and reverse decays convoluted with a Gaussian to the pyrrole parent signal in Fig. 6.2 e) we extract our Gaussian IRF as 214 fs. This calibration procedure is advantageous since calibration and data are extracted from the same TR-IY measurement, nevertheless, additional independent calibrations have been performed as described in Section 2 for further confirmation. The H atom transient in Fig. 6.2 d) shows signal along both directions of $\Delta t = 0$ and is therefore fit with forward and reverse rise functions that are convoluted with the Gaussian IRF. Each rise function incorporates a delay ("coherent shift") with respect to $\Delta t = 0$ as an additional parameter in accord with the fitting strategies introduced by Zewail *et al*. [32] and Leone *et al*. [33]. This coherent shift can be interpreted as the appearance time of the fully formed photoproduct in its mass channel and is the equivalent of the parent dissociation time. Such delayed rapid rise functions provide a good description of the photoproduct transients observed in the present study. An appearance time of 57 fs is extracted for the pump-induced dynamics ($\Delta t > 0$), indicating that pyrrole dissociates into H and pyrrolyl *via* the $\pi\sigma^*$ (1^1A_2) state on this timescale. As expected, this value lies between the 0.11 ps time constant reported by Lippert *et al*. [18] and 126 fs by Roberts *et al*. [19], when pyrrole is excited below the exit barrier at 250 nm, and the 46 fs lifetime reported by Roberts *et al* for 238 nm, above barrier excitation. [19] A time constant of < 30 fs is extracted for the probe-induced dynamics in support of the probe-pump mechanism described above. The pyrrolyl co-fragment (not shown) is well-described with a superposition of the parent fit accounting for the pump and probe induced dissociative ionization in the cross-correlation region and the H-transient forward and reverse rises for H atom production on the $\pi\sigma^*$ (1^1A_2) surface.

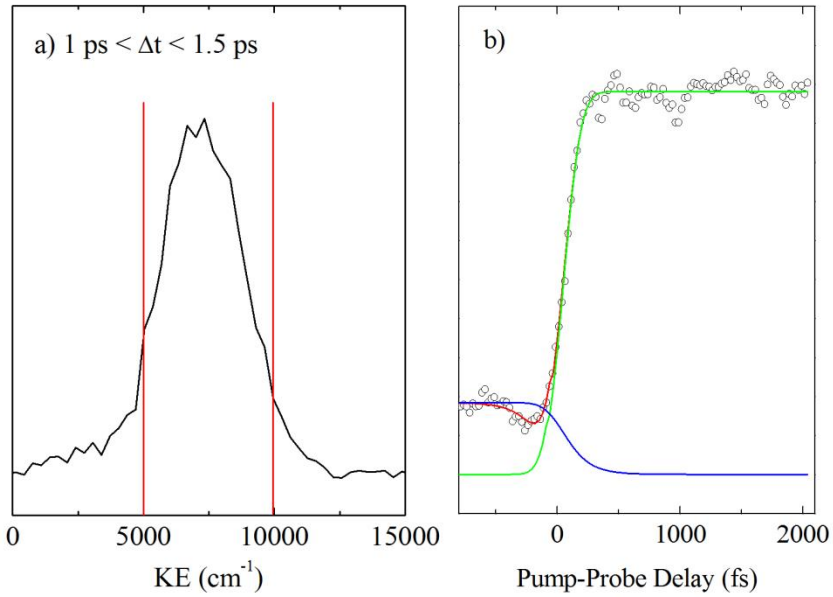

Figure 6.3 The TKER spectrum of H and pyrrolyl photoproducts extracted from a TR-TKER measurement with 240 nm excitation of pyrrole is shown on the left a). Integration over the kinetic energy range defined by the red cursors yields the H-atom transient plotted as open circles on the right b). The total fit to the transient is shown as a solid red line with its individual components in green and blue for forward and reverse dynamics, respectively.

In order to verify the origin of the detected H atoms, a TKER spectrum is recorded separately and presented in Fig. 3.a). Only one broad KE band centered around 7000 cm^{-1} is detected and associated with fast H atoms emitted from N-H dissociation along the $\pi\sigma^*$ (1^1A_2) surface, in agreement with previous experiments. [16, 19] Integration over this high KE feature yields the

time trace presented in Fig 6.3 b). Time constants of 36 and 34 fs, are extracted for the forward and reverse dynamics, respectively, in good agreement with our TR-IY scan.

Table 6.1 H atom appearance times following photodissociation at 240 nm. Each time constant is reported with a ±25% error. An "f" in the parentheses indicates a time constant that was fixed in the fit.

Technique	TR-IY		TR-TKER
Mass (amu)	1	67	1
Product	H	C_4NH_5	High KE H
$\Delta t_{forward}$ (fs)	57	19 (f)	36
$\Delta t_{reverse}$ (fs)	20	19 (f)	34

6.4.2 Photoexcitation at 217.5 nm.

Photoexcitation at 217.5 nm falls within a region of the first electronic absorption band where assignments of the underlying transitions are still under current debate. [1 – 5] The onset of the most intense $\pi\pi^*$ (1^1B_2) transition of pyrrole has been placed at around 217 nm by most publications [2, 3, 6], whereas the onset of an additional, weaker $\pi\pi^*$ (2^1A_1) transition, with lower oscillator strength, [15] is also located at around 223 nm [3]. The most recent reinterpretation, attributes $\pi\sigma^*$ (2^1B_1) state population *via* intensity borrowing from bright $^1\pi\pi^*$ states [5] as the main contribution to the absorption band at 217 nm and places the $\pi\pi^*$ (1^1B_2) maximum around 199 nm. The 217.5 nm excitation data presented below is assessed and discussed in the context of these proposals.

The mass spectra at 217.5 nm pump and 243.15 nm probe (Fig. 6.4 a) – c)) differ significantly from those at 240 nm excitation. Mass spectra now clearly display several larger photofragments for $\Delta t > 0$ including m/z = 28, 39, 40, 41 which are assigned to CNH_2^+, $C_3H_3^+$, $C_3H_4^+$ and $C_2NH_3^+$, respectively, compared to only minor fragmentation for $\Delta t < 0$. Two-color, multiphoton dissociative ionization may contribute to the enhanced signals within the cross-correlation region ($\Delta t = 0$, Fig 6.4 b)). In principle cationic dissociation paths can yield identical fragmentation products, [21, 34] however, at the pump pulse energies employed here we can rule out any significant contributions from two-photon, pump-only population of a long-lived cationic state. We therefore associate the fragment peaks at $\Delta t > 0$ (Fig. 6.4 c)) with processes involving neutral excited states. Consequently, the existence of these larger fragments at long pump-probe delays indicates that ring deformation pathways along the $\pi\pi^*$ (1^1B_2) potential energy surface participate in the excited state deactivation of pyrrole. We assume that the $\pi\pi^*$ (1^1B_2) state is photoexcited directly although indirect population from the $\pi\sigma^*$ (2^1B_1) or hot $\pi\sigma^*$ (1^1A_2) is possible, but considered less likely. [10] Once on the $\pi\pi^*$ (1^1B_2) state, dynamics simulations by Barbatti *et al*. [10] have predicted the observed fragments as direct photodissociation products from the ring deformation coordinate while Sellner *et al*. [11] have proposed an indirect photochemical mechanism. In the latter case, following internal conversion through the $\pi\pi^*$ / S_0 CI at a ring-puckered geometry, the hot ground state pyrrole molecule undergoes ring opening followed by ring closure of the biradical chain, forming a cyclopropenyl ring, NH=CH-C_3H_3. HCNH and C_3H_3 fragments are explained as secondary photoproducts of this trend. H atoms (Fig. 6.4 d) and their pyrrolyl co-fragments at $\Delta t > 0$ originate from the N-H dissociation pathways discussed in section 6.3.1, possibly due to a two-step relaxation process, starting from diabatic change from the initially excited $\pi\pi^*$ (1^1B_2) state or $\pi\sigma^*$ (2^1B_1) suggested by Vazdar *et*

al. [12] and Neville *et al*. [5], respectively, onto the dissociative πσ* (1^1A_2) state. Trajectory calculations predict that ~80% of the photoexcited pyrrole molecules follow this pathway. [12] Alternatively, the πσ* (2^1B_1) state may dissociate directly. [5, 31] It is noteworthy that the branching ratio of the competing N-H dissociation and ring deformation pathways is not reflected in the signal intensities of our mass spectra. H atom photoproducts require three photon ionization due to their high IP as opposed to one (or possibly two) photons for larger fragments, although this is somewhat compensated for by resonant enhancement and the overall higher H atom yield.

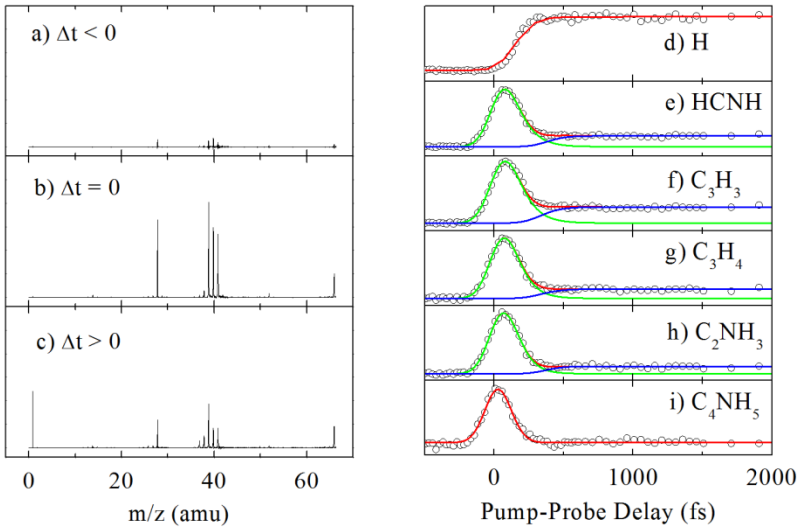

Figure 6.4 Mass spectra and transients extracted from 2d TR-IY spectra (not shown) of pyrrole following 217.5 nm photoexcitation are presented. Mass spectra for three integration regions

corresponding to before a), at b) and after c) pump-probe timing overlap are plotted with identical intensity scales for all three cases. Transients of hydrogen d), larger fragments e)-h), and the pyrrole parent i) are represented by open circles. The total fit is shown as a solid red line with individual components for dissociative ionization (green) and excited state dissociation (blue).

Transients of major photofragments are displayed in Figs. 6.4 d) - h). The zero time delay and Gaussian IRF are determined by the parent transient (Fig. 6.4 i), which is described by a single exponential decay with τ_{dec} = 29 fs. [31] The H atom time trace (Fig. 6.4 d) is fit with a delayed rapid rise with time delay of 98 fs. In contrast to 240 nm photoexcitation, signal levels along the $\Delta t < 0$ direction are negligible alleviating the necessity of a reverse rise function. The N-H dissociation dynamics will be discussed in the context of the TR-TKER measurement which discriminates statistical H atom decay products on a KE basis. Larger photofragments (Fig. 6.4 e) - h)) are fit with a decay function and a delayed rise convoluted with the Gaussian IRF, and respective time constants are listed in Table 6.2. As the photoexcited pyrrole parent molecule relaxes on the $\pi\pi^*$ (1^1B_2) along the ring-deformation coordinate, it is subjected to multiphoton dissociative ionization by the probe pulse until it reaches the $\pi\pi^*/S_0$ CI. The decay dynamics measured in the fragment mass channels, 75 – 97 fs, are slightly longer than those obtained for the parent mass (Fig. 6.4 i)). It is plausible that the fragment channels selectively probe the ring deformation pathway due to favorable overlap with the corresponding cationic paths. The parent mass channel, in contrast, measures an average time constant for relaxation along all competing pathways including the dominant and shorter NH dissociation constant. To account for a steady state product signal observed in the fragment mass channels at long $\Delta t > 0$, an additional time-

delayed rise is included in the fitting function. The extracted time delays are associated with dissociation dynamics along the ring deformation coordinate to the ring-puckered $\pi\pi^*$ (1^1B_2) / S_0 CI up to the full formation of the fragment. While our observed photofragmentation pattern discussed above supports the hot S_0 ground state mechanism by Sellner *et al*. [11 - Sellner] involving ring opening, closing and dissociation, the 275 to 331 fs time constants are much shorter than their proposed >1000 fs timescale (outside their simulation window) for final product formation. The ultrafast fragmentation observed here is more in line with a direct dissociation process as identified by Barbatti *et al*. (10 – Barbatti). The time trace of pyrrolyl (not shown), the co-fragment of H, displays dissociative ionization and a delayed rise similar to the other larger fragments but the dynamics are distinctly different. In particular, the delayed rise component is best described with a significantly shorter delay constant equivalent to the H atom trace.

TR-TKER measurements are essential for the characterization of the H atom elimination dynamics at 217.5 nm excitation. In contrast to the longer excitation wavelength, the TKER spectrum (Fig. 6.5 a)) now displays a bi-modal distribution with a discrete low KE peak near 1000 cm^{-1} aside from the previously observed high KE feature near 7000 cm^{-1}. Somewhat surprising, but in agreement with previous wavelength dependency studies, [16, 19] the latter remains within the same KE region despite the additional ~4300 cm^{-1} in excitation energy available at 217.5 compared to 240 nm. Hence, it can be concluded that the initial vibrational excitation is conserved within the molecule rather than redistributed into H atom translational KE. Hence, the signal is correlated with the formation of a vibrationally excited pyrollyl cofragment in its electronic ground state either *via* $\pi\sigma^*$ (2^1B_1) $\rightarrow$ $\pi\sigma^*$ (1^1A_2) or $\pi\pi^*$ (1^1B_2) $\rightarrow$

$\pi\sigma^*$ (1^1A_2). The low KE H atom products are assigned to either statistical unimolecular decay or undesired multiphoton dissociative ionization process in accordance with high-resolution measurements by Cronin *et al.* [16] In light of the reinterpretation of the absorption spectrum by Ref 5 [5], photoexcitation and direct dissociation of the $\pi\sigma^*$ (2^1B_1) is another possibility, in particular since the high energy tail of the low KE H atom feature can be envisaged to coincide with the maximum KE cutoff [19] of 9177 cm^{-1} for this channel.

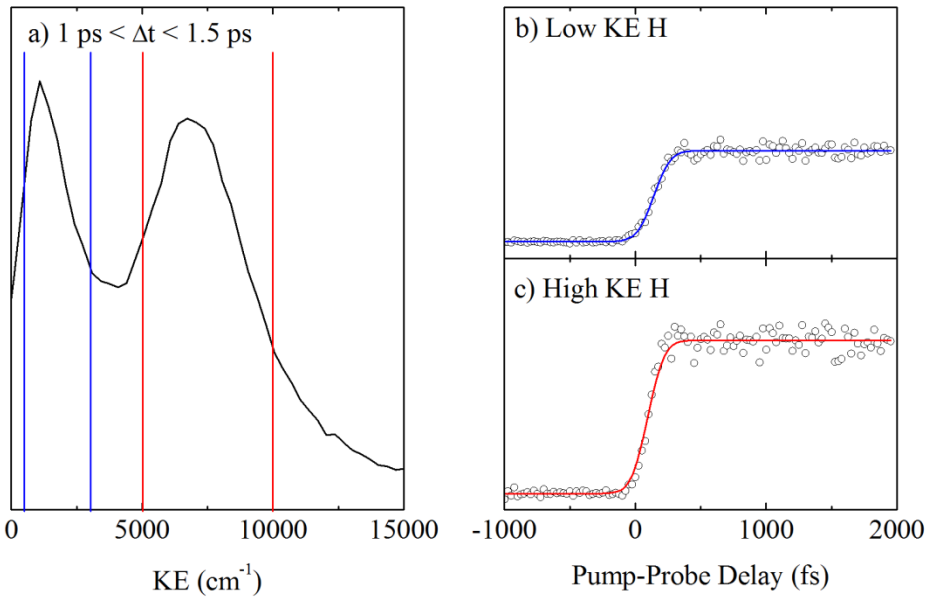

Figure 6.5 The TKER spectrum of H and pyrrolyl photoproducts extracted from a TR-TKER measurement with 217.5 nm excitation of pyrrole is shown on the left a). Integration over the low (blue cursors) and high (red cursors) KE energy regions yields the H atom transients plotted in b) and c) on the right, respectively. Open circles represent the signal while the fit is shown as a

colored solid line.

Two integration regions corresponding to low and high KE H atoms are selected to generate their respective time traces (Fig. 6.5 b) – c)), which are fit with a time-delayed rapid rise similar to the TR-IY H atom data. The high KE H atoms (Fig. 6.5 b)) associated with the $\pi\sigma^*$ dynamics start rising after a delay of Δt = 79 fs, which is somewhat longer than the time constant for 240 nm excitation. This increase may be explained by the extra time it takes to proceed through an additional internal conversion step. At 217.5 nm, photoexcitation populates the $\pi\pi^*$ (1^1B_2) and/or $\pi\sigma^*$ (2^1B_1) which feed the lower $\pi\sigma^*$ (1^1A_2) and subsequent N-H dissociation process. Theoretical dynamics calculations estimate the coupling times for the $\pi\pi^*$ (1^1B_2) $\rightarrow$ $\pi\sigma^*$ (1^1A_2) $\rightarrow$ S_0 as 44 fs and 80 fs (12 – Vazdar) and $\pi\sigma^*$ (2^1B_1) $\rightarrow$ $\pi\sigma^*$ (1^1A_2) $\rightarrow$ S_0 as 19 and 61 fs [31], all of which agree well with our extracted 79 fs H atom appearance time. The low KE H atom time trace (Fig. 6.5 c)) is described with a longer delay time constant of 125 fs. Low KE H atoms are typically associated with slow statistical unimolecular decay of the hot ground state molecule [12, 13] although signals with ultrashort appearance times have been attributed to multiphoton dissociative ionization. [19] This may also be the case for pyrrole. Meanwhile, direct dissociation of the photoexcited $\pi\sigma^*$ (2^1B_1) state [31] is expected to occur on ultrafast timescales but a definitive assignment would require further investigation. The Δt = 98 fs extracted from the H atom TR-IY in Fig. 6.4 d) lies in between the time constants of high and low KE H atoms, as both contribute to the rapid rise of the H^+ signal.

Table 6.2 Appearance times of photofragments following 217.5 nm excitation. Each time constant is reported with a ±25% error. An "f" in the parentheses indicates a time constant that

was fixed in the fit.

Technique	TR-IY						TR-TKER	
Mass (amu)	1	28	39	40	41	67	1	1
Product	H	HCNH	C_3H_3	C_3H_4	C_2NH_3	C_4NH_5	Low KE H	High KE H
Δt (fs)	98	331	275	275	331		125	79
τ_{dec} (fs)		96	97	84	75	29(f)		

6.4.3 Photoexcitation at 200 nm

While for 217.5 nm photoexcitation the underlying transitions are still under debate there is general agreement that the bright $\pi\pi^*$ (1^1B_2) state of pyrrole is populated at 200 nm. In fact, Neville *et al*. (5 – Neville 2014) calculate the vertical excitation energy of the $\pi\pi^*$ (1^1B_2) state as 6.2 eV (200 nm). TR-IY and TR-TKER spectra are discussed below in comparison with the longer excitation wavelength.

The similarity between the mass spectra at 200 (Fig. 6.6 a) – c)) and 217.5 nm (Fig. 6.4 a) – c)) is immediately apparent. At $\Delta t = 0$ (Fig. 6.6 b)) and $\Delta t > 0$ (Fig. 6.6 c)), the dominant peaks again correspond to HCN^+ (m/z = 27), CNH_2^+ (m/z = 28), $C_3H_3^+$, (m/z = 39), $C_3H_4^+$ (m/z = 40), and $C_2NH_3^+$ (m/z = 41) and H^+ (m/z =1) and pyrrolyl$^+$ (m/z=66) cofragments. For larger fragments, the signal enhancement at $\Delta t = 0$ is due to dissociative ionization and signal levels at $\Delta t < 0$ are overall negligible. We therefore conclude that ring deformation and NH-stretching pathways are both accessible from the initially excited $\pi\pi^*$ (1^1B_2), the latter *via* a $\pi\pi^*$ (1^1B_2) / $\pi\sigma^*$ (1^1A_2) CI.

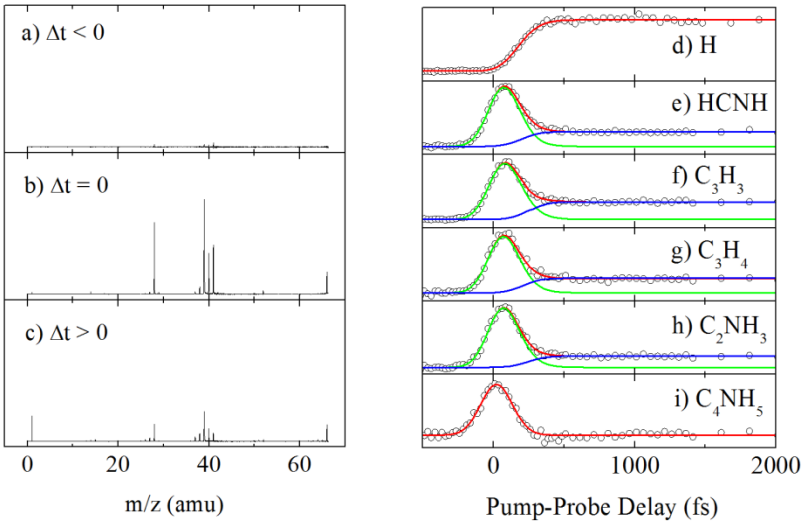

Figure 6.6 Mass spectra and transients extracted from 2d TR-IY spectra (not shown) of pyrrole following 200 nm photoexcitation are presented. Mass spectra for three integration regions corresponding to before a), at b) and after c) pump-probe timing overlap are plotted with identical signal intensity scales for all three cases. Transients of atomic hydrogen d), larger fragments, e)-h), and the pyrrole parent i) are represented by open circles. The total fit is shown as a solid red line with individual components for dissociative ionization (green) and excited state dissociation (blue).

Transients of the different photofragments (Fig. 6.6 d) – h)) are all analyzed using identical fitting functions as for the 217.5 nm data and extracted time-constants are summarized in Table

6.3. The zero time-delay and Gaussian IRF are determined by the parent transient (Fig. 6.6 i), which is fit with a single exponential decay of 29 fs. [31] The H atom transient (Fig. 6.6 d) displays a delayed rapid rise with a Δt = 119 fs coherent shift which is associated with NH dissociation. The pyrrolyl co-fragment (not shown) experiences the same rise characteristics and a superimposed exponential decay of 64 fs associated with multiphoton dissociative ionization. All other photofragments generated *via* a ring-deformation process (Fig. 6.6 e) – h)) are described with an exponential decay signal of τ_{dec} = 60 - 71 fs and a rapid rise starting at Δt = 199 – 246 fs. These ultrafast appearance times indicate a direct fragmentation process and are in good agreement with the calculated timeframe of < 200 fs for reaching the ring puckered CI/seam [12] as well as with previous 200 nm photofragmentation measurements on pyrazole [25] and imidazole [26]. In comparison to 217.5 nm photoexcitation, the shorter fragment appearance times at 200 nm are due to the additional excess energy available for ring puckering motion to access the CI/seam and subsequent flow into the bond dissociations. A similar dependence of the deactivation timescales on the initial photoexcitation energy has been observed in related heterocyclic molecules. [23, 35, 36]

The TKER spectrum (Fig. 6.7 a)) has the same bi-modal KE distribution as for 217.5 nm photoexcitation (Fig. 6.5 a)), but with a smaller fast-to-slow H atom ratio. This reproduces a similar trend observed in the high-resolution work by Cronin *et al*., [16] who attribute the low KE peak to statistical unimolecular decay. Such increase in signal is certainly plausible considering the additional energy deposited into the molecule upon 200 nm photoexcitation that internally converts into ground state vibrational excitation. However, when evaluating the rise dynamics other sources of low KE H atom have to be taken into account, which is discussed

below. The high KE H atoms are unambiguously assigned to the NH-stretching pathway with H and ground state pyrrolyl photoproducts formed *via* $\pi\pi^*$ (1^1B_2) $\rightarrow$ $\pi\sigma^*$ (1^1A_2) internal conversion in line with Refs. 16 and 19 [16, 19].

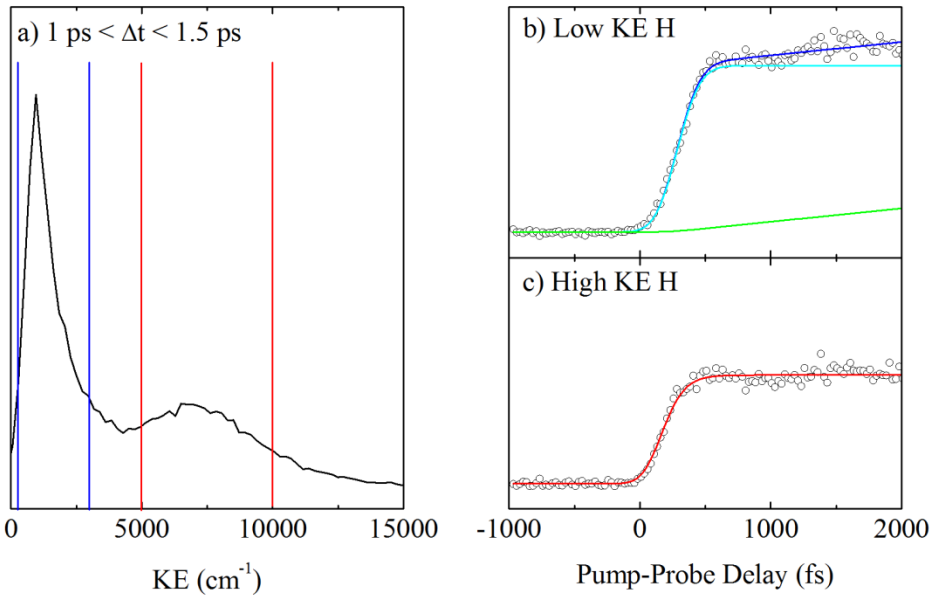

Figure 6.7 The TKER spectrum of H and pyrrolyl photoproducts extracted from a TR-TKER measurement with 200 nm excitation of pyrrole is shown on the left a). Integration over the low (blue cursors) and high (red cursors) KE energy regions yields the H atom transients plotted in b) and c) on the right, respectively. Open circles represent the signal while the fit is shown as colored solid lines.

Integration of the two features in the TKER spectrum yields the transients of low and high KE H atoms presented in Fig. 6.7 b) and c), respectively. Internal conversion along the $\pi\pi^*$ (1^1B_2) $\rightarrow$ $\pi\sigma^*$ (1^1A_2) $\rightarrow$ dissociation pathway is considered the source of high KE H atom photoproduct (Fig. 6.7 c)) and, analogous to 217.5nm excitation, a 96 fs coherent shift is extracted for the delayed rapid rise and compares to an appearance time of 52 fs measured by Roberts *et al*. [19] It also agrees well with Vazdar *et al*. (12 – Vazdar 2009), who calculated 44 fs for population of the $\pi\sigma^*$ (1^1A_2) state and 80 fs for relaxation to S_0; the same trajectory simulations observe the start of H elimination at around 54 fs. Barbatti *et al*., [13] in contrast, predict 184 fs for deactivation along the NH-stretching pathway of which ~100 fs are attributed to relaxation from higher excited $\pi\pi^*$ states onto $\pi\sigma^*$ (1^1A_2). Compared to 217.5 nm excitation (Fig. 6.5 c)), the measured time constant is longer which is consistent with the latter simulation and interpretation. On the other hand, this increase may also hint a change in deactivation pathway, for example, $\pi\sigma^*$ (2^1B_1) $\rightarrow$ $\pi\sigma^*$ (1^1A_2) at 217.5 nm according to Worth *et al*. [5] *versus* $\pi\pi^*$ (1^1B_2) $\rightarrow$ $\pi\sigma^*$ (1^1A_2) at 200 nm.

The 200 nm low KE H transient (Fig. 6.7 b)) is significantly different from 217.5 nm excitation. Starting around ~1000 fs a second step is superimposed onto the plateau of the initial H atom rise and the transient is therefore fit with a Gaussian convoluted delayed double step function. A time constant of 236 fs is extracted for the coherent shift of the rapid rise while the slow rise is set fixed to 660 ps (as determined from a longer range scan). This continuously increasing signal at long pump-probe delays is characteristic for statistical unimolecular decay of the hot ground state molecule following internal conversion. The same behavior has been observed by Roberts *et al*. [19] who extract time constants of 108 fs and 1 ns from their fit. Various sources may contribute to the rapidly rising low KE H atom signal, unwanted multiphoton dissociative

ionization processes being one of the mostly cited. [19, 25, 26] However, direct dissociation into H + pyrrolyl (Ã) photoproducts *via* the πσ* (2^1B_1) would also be feasible in analogy to the discussion above for 217.5 nm excitation.

Table 6.3 Appearance times of photofragmentation products following 200 nm excitation. Each time constant is reported with a ±25% error. An "f" in the parentheses indicates a time constant that was fixed in the fit.

Technique	TR-IY						TR-TKER	
Mass (amu)	1	28	39	40	41	67	1	1
Product	H	HCNH	C_3H_3	C_3H_4	C_2NH_3	C_4NH_5	Low KE H	High KE H
Δt (fs)	119	199	246	211	231		236	96
τ_{dec} (fs)		60	71	64	64	29(f)		

6.5 Conclusion

The photodissociation dynamics of pyrrole following UV excitation to the lowest electronically excited states of ππ* and πσ* character are investigated through TR-IY and TR-TKER experiments with the goal to assess theoretically predicted ring-deformation and NH-stretching pathways. Mass spectra are analyzed for the appearance of larger photofragments to characterize deactivation *via* a ring-puckered CI whereas the high KE H atoms observed in TKER spectra are associated with direct dissociation dynamics of the N-H bond.

Photoexcitation at 240 nm directly populates the $\pi\sigma^*$ (1^1A_2) which dissociates in < 50 fs into high KE H and ground state pyrrolyl products. Neither statistical decay (low KE H) nor fragmentation into larger products is observed.

The dominant transition underlying 217.5 nm absorption is currently still under debate but considered as either $\pi\pi^*$ (1^1B_2) or $\pi\sigma^*$ (2^1B_1). Either state is predicted to feed the lower-lying $\pi\sigma^*$ (1^1A_2) which then yields high KE H atoms with a somewhat longer appearance time of 79 fs. Meanwhile the rapid formation (125 fs) of low KE H atoms is discussed in the context of unwanted multiphoton dissociative ionization or direct dissociation along the $\pi\sigma^*$ (2^1B_1) into H and pyrrolyl coproducts but the latter now in its first electronically excited state. The ring-deformation pathway is energetically open and considered the source of large photoproducts which form within 275 to 331 fs *via* a $\pi\pi^*$ (1^1B_2) / S_0 CI.

Excitation with 200 nm reaches the $\pi\pi^*$ (1^1B_2) from which both competing relaxation pathway are energetically accessible. Coupling onto the $\pi\sigma^*$ (1^1A_2) state generates H atom with high KE and ground state pyrrolyl photoproducts in 96 fs. Rapidly forming (236 fs) low KE H atoms are again attributed to dissociative ionization or direct dissociation of $\pi\sigma^*$ (2^1B_1). Statistical decay of pyrrole in the hot ground state following internal conversion is also found to contribute low KE H atoms but occurs on a much longer timescale (660 ps). The observation of larger fragments with appearance times of 199 to 246 fs confirms that ring-deformation pathways participate in the deactivation process.

6.6 References

[1] L. Serrano-Andres, M. Merchan, I. Nebot-Gil, B. O. Roos, and M. Fulscher, *J. Am. Chem. Soc.*, 1993, 115, 6184-6197.

[2] O. Christiansen, J. Gauss, J. F. Santon, and P. Jorgensen, *J. Chem. Phys*., 1999, 111, 525.

[3] B. O. Roos, P-A Malmqvist, V. Molina, L. Serrano-Andres, and M. Merchan, *J. Chem. Phys.*, 2002, 116, 7526.

[4] M. H. Palmer and P. L. Wilson, *Mol. Phys.*, 2003, 101, 2391-2408.

[5] S. P. Neville, and G. A. Worth, *J. Chem. Phys.*, 2014, 140, 034317.

[6] M. H. Palmer, I. C. Walker, M. F. Guest, *Chem. Phys.*, 1998, 238, 179.

[7] A. L. Sobolewski and W. Domcke, *Chem. Phys.*, 2000, 259, 181.

[8] V. Vallet, Z. Lan, S. Mahapatra, A. L. Sobolewski, and W. Domcke, *J. Chem. Phys.*, 2005, 123, 144307.

[9] L. Lan, A. Dupays, V. Vallet, S. Mahapatra and W. Domcke, *J. Photochem. Photobio. A Chem.*, 2007, 190, 177-189.

[10] M. Barbatti, M. Vazdar, A. J. Aquino, M. Eckert-Maksic, and H. Lischka, *J. Chem. Phys.*, 2006, 125, 164323.

[11] B. Sellner, M. Barbatti, and H. Lischka, *J. Chem. Phys.*, 2009, 131, 024312.

[12] M. Vazdar, M. Eckert-Maksic, M. Barbatti, and H. Lischka, *Mol. Phys.*, 2009, 107, 845.

[13] M. Barbatti, J. Pittner, M. Pederzoli, U. Werner, R. Mitric, V. Bonacic-Koutecky, and H. Lischka, *Chem. Phys.*, 2010, 375, 26.

[14] J. Wei, A. Kuczmann, J. Riedel, F. Renth, and F. Temps, *Phys. Chem. Chem. Phys.*, 2003, 5, 315-320.

[15] J. Wei, J. Riedel, A. Kuczmann, F. Renth, and F. Temps, *Faraday Discuss.*, 2004, 127, 267.

[16] B. Cronin, M. G. D. Nix, R. H. Qadiri, and M. N. R. Ashfold, *Phys. Chem. Chem. Phys.*, 2004, 6, 5031.

[17] B. Cronin, A. L. Devine, M. G. D. Nix, and M. N. R. Ashfold, *Phys. Chem. Chem. Phys.*, 2006, 8, 3440.

[18] H. Lippert, H. –H. Ritze, L. V. Hertel, and W. Radloff, *ChemPhysChem.*, 2004, 5, 1423.

[19] G. M. Roberts, C. A. Williams, H. Yu, A. S. Chatterley, J. D. Young, S. Ullrich, and V. G. Stavros, *Faraday Discuss.*, 2013, 163, 95-116.

[20] D. A. Blank, S. W. North, and Y. T. Lee, *Chem. Phys.*, 1994, 187, 35.

[21] E. E. Rennie, C. A. F. Johnson, J. E. Parker, R. Ferguson, D. M. P. Holland, and D. A. Shaw, *Chem. Phys.*, 1999, 250, 217.

[22] A. J. van den Brom, M. Kapelios, T. N. Kitsopoulos, N. H. Nahler, B. Cronin, and M. N. R. Ashfold, *Phys. Chem. Chem. Phys.*, 2005, 7, 892.

[23] N. L. Evans, and S. Ullrich, *J. Phys. Chem. A*, 2010, 114, 11225.

[24] R. Crespo-Otero, M. Barbatti, H. Yu, N. L. Evans, and S. Ullrich, *Chem. Phys. Chem.*, 2011, 17, 3365.

[25] C. A. Williams, G. M. Roberts, H. Yu, N. L. Evans, S. Ullrich, and V. G. Stavros, *J. Phys. Chem. A*, 2012, 116, 2600.

[26] H. Yu, N. L. Evans, V. G. Stavros, and S. Ullrich, *Phys. Chem. Chem. Phys.*, 2012, 14, 6266.

[27] N. L. Evans, H. Yu, G. M. Roberts, V. G. Stavros, and S. Ullrich, *Phys. Chem. Chem. Phys.*, 2012, 14, 10401.

[28] H. Yu, N. L. Evans, A. S. Chatterley, G. M. Roberts, V. G. Stavros, and S. Ullrich, *J. Phys. Chem. A*, 2014, 118, 9438.

[29] W. C. Wiley and I. H. McLaren, *Rev. Sci. Instruments*, 1955, 26, 1150.

[30] P. Kruit, and F. H. Read, *J. Phys. E.*, 1983, 16, 313.

[31] G. Wu, S. P. Neiville, O. Schalk, T. Sekikawa, M. N. R. Ashfold, G. A. Worth, and A. Stolow, *J. Chem. Phys.*, 2015, 142, 074302.

[32] D. Zhong, P. Y. Cheng, and A. Zewail, *J. Chem. Phys. A*, 1998, 102, 4031-4058.

[33] M. E. Vaida and S. R. Leone, *Chem. Phys.*, 2014, 442, 41-47.

[34] G. D. Willett, T. Baer, *J. Am. Chem. Soc.*, 1980, 102, 6774.

[35] K. Kosma, C. Schroter, E. Samoylova, I. V. Hertel, and T. Schultz, *J. Am. Chem. Soc.*, 2009, 131, 16939-16943.

[36] J-W. Ho, H-C. Yen, W-K. Chou, C-N. Weng, L-H. Cheng, H-Q. Shi, S-H. Lai, and P-Y. Cheng, *J. Phys. Chem. A*, 2011, 115, 8406-8418.

CHAPTER 7

RELAXATION DYNAMICS OF UV EXCITED URACIL AND THYMINE STUDIED BY FEMTOSECOND TIME-RESOLVED PHOTOELECTRON SPECTROSCOPY

7.1 Motivation and Introduction

Isolated nucleo bases are considered photostable under ultraviolet (UV) radiation, due to their ultrafast excited state deactivation mechanisms — an inherent property that may have contributed to their selection as building blocks of life under the harsh radiation environment of the early earth. [1 – 3]

Among the DNA bases, uracil and thymine (see Fig. 7.1) are both pyrimidine derivatives with oxygen substituents at positions 2 and 4 of the six-membered heterocylic ring. Uracil, also known as 2-oxy-4-oxy pyrimidine, differs structurally from thymine, which possesses an additional CH_3 group located at position 5.

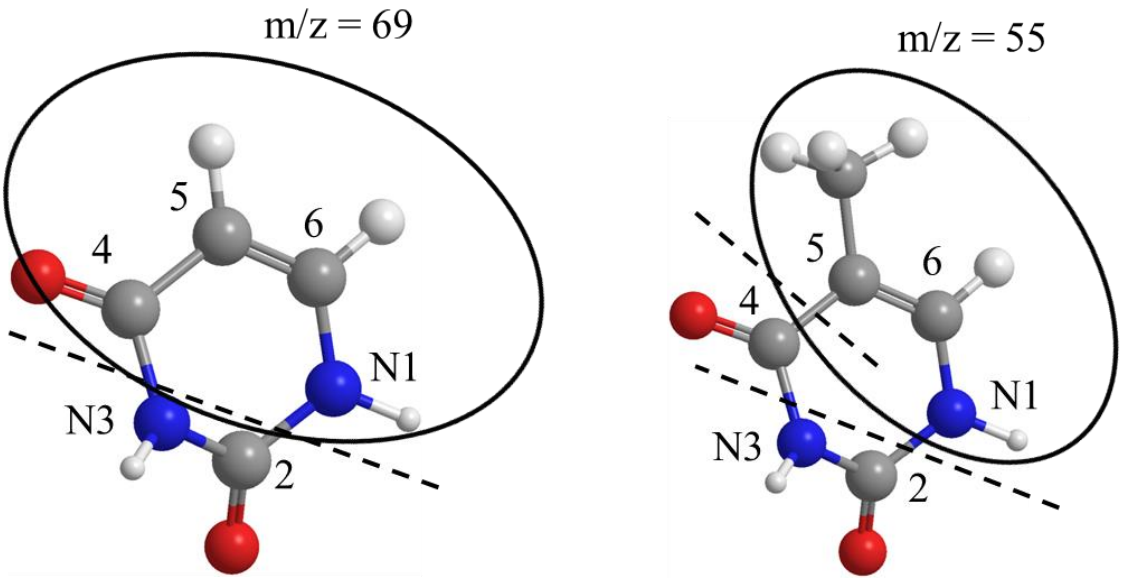

Figure 7.1 Molecular structure of uracil (left) and thymine (right). Dashed lines indicate the bond breakage for formation of the respective fragment during dissociative ionization. [4]

7.2 Review of Literature

7.2.1 Absorption spectrum, He(I) photoelectron spectrum, ionization correlations

As structurally similar molecules, the UV absorption spectra of uracil and thymine bear close resemblance. Both spectra are characterized by a first absorption band spanning the 300-220 nm (4.1-5.6 eV) region which evolves into a second broad feature around 220-180 nm (or 220 – 163) (5.6-5.9 eV or 5.6 – 7.6 eV). [5, 6] Ab initio simulations of the absorption spectra by Barbatti *et al*. [6] attribute most intensity to optically bright ππ* transitions as direct excitation of the close-lying nπ* states is essentially forbidden [7]. Numerous theoretical calculations have analyzed the lowest electronically excited states. For uracil and thymine, respectively, the first excited states are of nπ* character and their energy minimums are located at 3.06 eV (405 nm) and 4.37 eV (284 nm), while their ππ* states are higher in energy at 3.68 eV (337 nm) and 4.77 eV (260 nm).

[8, 9] Vertical excitation energies have been determined as 4.83 (257 nm) eV for nπ* and 5.2 eV (238 nm) for ππ* state of uracil and, similarly, 4.88 eV (254 nm) for nπ* and 5.17 eV (240 nm) for ππ* state of thymine. [10] Electronically excited states of πσ* character are above 7.3 eV (< 169 nm) [10 – Huddock] and are energetically inaccessible in the present study. Steady-state He(I) photoelectron spectra provide insight into the cationic states of relevance to photoionization experiments. For the present work, most important are the two lowest ionization potentials (IP) which correspond to a π^{-1} and n^{-1} band with experimentally determined vertical energies of 9.3 – 9.6 eV and 10.31 eV for uracil and 9.0 – 9.2 eV and 10.05 eV for thymine. [11 – 20] For photoionization experiments via intermediate excited state resonances Koopmans-like ionization correlations have been determined as follows. The lowest electronically excited state S_1 of nπ* character is expected to preferentially ionize into D_1 (n^{-1}) whereas the S_2 ππ* state has been associated primarily with ionization into D_0 (π^{-1}). [10, 21] This simple steady-state picture provides some guidance for the interpretation of resonant enhanced multiphoton photoelectron spectra although limited to the vertical excitation-ionization region. As discussed in detail below, interpretation of time-resolved photoionization studies requires knowledge of the ionization potentials and correlations along excited state relaxation pathways.

7.2.2. Theoretical pathways and theoretical dynamics

Ab initio calculations reveal similar excited state pathways in uracil and thymine which have been reviewed thoroughly in Refs. 22 – 24 [22 – 24] and can be summarized as follows: (1) A direct path from S_2 ππ* to an "ethylenic twisting" ππ*/S_0 CI (involving an intermediate ππ*/nπ* CI); (2) Internal conversion from the S_2 ππ* to S_1 nπ* state via the ππ*/nπ* CI with further deactivation via either a "CO stretching" nπ*/S_0 CI or barrier crossing to the ππ* state and

$\pi\pi^*/S_0$ CI. Intersystem crossing from the S_1 $n\pi^*$ to a $^3\pi\pi^*$ triplet state has also been proposed following the initial $S_2 - S_1$ internal conversion. [6, 25, 26]

In extension, dynamics simulations provide further insight into the actual deactivation mechanisms and also illuminate unique behavior in uracil and thymine. Trajectory simulations by Barbatti *et al*. [27] starting from the FC region show relaxation to the shallow S_2 minimum– in agreement with earlier ab initio multiple spawning dynamics [10]. On a picosecond timescale they internally convert to the S_1 $n\pi^*$ via the $\pi\pi^*/n\pi^*$ CI intersection, a process that involves motion of the C5-CH_3/H group and consequently takes longer in thymine than in uracil (2.3 versus 1.5 ps, respectively). [27] The fate of the $n\pi^*$ state population remains uncertain due to limitations in the simulation time window although for energetic reasons deactivation via the $\pi\pi^*/S_0$ CI is considered the most likely. This mechanism, involving subsequent steps of $\pi\pi^*_{min}$ $\rightarrow$ $\pi\pi^*/n\pi^*$ CI $\rightarrow$ $n\pi^*_{min}$ $\rightarrow$ $\pi\pi^*/S_0$ CI $\rightarrow$ S_0, dominates the uracil and thymine photophysics. In uracil two additional pathways are active to a lesser extent with the first corresponding to direct deactivation along the $\pi\pi^*$ state via the $\pi\pi^*/S_0$ CI and the second of ring-opening nature. Both proceed on timescales of several hundred femtoseconds. [27] For the case of uracil, it has also been shown that consideration of triplet states in the dynamics calculations, i.e. inclusion of both non-adiabatic and spin orbit coupling, alters this picture. [25, 26] Specifically, these calculations show ultrafast (30 fs) $\pi\pi^* \rightarrow n\pi^*$ internal conversion followed by depopulation of the $n\pi^*$ state within 2.4 ps through intersystem crossRichtering to the triplet $^3\pi\pi^*$ state with only minor fractions returning to S_0. [26]

7.2.3. Experimental dynamics studies

Several gas-phase studies based on femtosecond pump-probe photoionization techniques have been employed over the years to investigate the photophysics of gas-phase nucleobases, many of them supplemented by their own ab initio calculations and dynamics simulations.

Time-resolved ionization yield (TR-IY) measurements first performed by Kang *et al* at 267 nm excitation [28]. In additional to a Gaussian component, the uracil and thymine transients are described by a single exponential decay of 2.4 ps and a bi-exponential decay of 6.4 and >100 ps, respectively, together with a femtosecond dynamic that is attributed to the Gaussian full width at half maximum (FWHM) of the laser pulse. The authors propose excitation to mixed $\pi\pi^*/n\pi^*$ states followed by picosecond internal conversion through a CI on the $n\pi^*$ section of the potential energy surface as a likely deactivation mechanism — in analogy with their adenine study. The longer time constant unique to thymine is associated with intersystem crossing to a triplet state. Time-resolved photoelectron spectroscopy (TR-PES) has the advantage of providing additional spectral information that aids in the identification of electronically excited states. TR-PES spectra of all nucleobases were measured at 250 nm excitation by Ullrich *et al*. [29] The uracil data was described by one Gaussian component of <50 fs and two decays of 530 fs and 2.4 ps, whereas thymine was fit with <50 fs, 490 fs and 6.4 ps. Due to the TRPES scan range being limited to 2.3 ps, in both cases the picosecond time constant was fixed to values reported by Kang et al. [28]. The femtosecond time constants and all associated photoelectron spectra were extracted through global analysis of the two-dimensional TR-PES data but the authors initially refrain from interpretation of the spectroscopic data. The uracil and thymine TR-PES spectra are revisited and further analyzed with the help of the *ab initio* multiple spawning simulations mentioned above. [10] Through comparison of measured and calculated photoelectron yields and taking energetics and propensities of the ionization process along the relaxation path into account

a photophysical model to describe the TR-PES results is proposed. The two lowest lying ionic states, D_0 and D_1, of uracil and thymine are of $n^2\pi$ (π^{-1} hole) and $n\pi^2$ (n^{-1} hole) characters. Hence the excited $\pi\pi^*$ state preferentially ionizes into D_0 but states with $n\pi^*$ character ionize into D_1. Furthermore, the D_0 ionization potential increases significantly in going from the Franck-Condon region to the S_2 minimum and D_0 and D_1 become degenerate at this point. The TR-PES spectra are characterized by a ~1.2 eV energetic shift of the photoelectron band within the first few hundred femtoseconds. At early times signals are purely from D_0 (π^{-1}) ionization and the initial rapid decay and shift are in line with the predicted increase in the D_0 ionization potential. The measured picosecond time constant is attributed to subsequent barrier crossing and internal conversion to the $n\pi^*$ state. This process however falls outside the simulation window and the interpretation is tentative, but supported by an elongation of the thymine time constant due to motion of the heavier CH_3 group as opposed to H in uracil. The shifted photoelectron band in the TR-PES spectrum at later times is the result of increasing contribution of D_1 (n^{-1}) photoelectron yield and generally higher ionization potentials.

Mass-selected TR-IY experiments by Canuel *et al*. [30] yield decay constants of 130 and 1050 fs for uracil and 105 and 5120 fs for thymine at an excitation wavelength of 267 nm. This bi-exponential relaxation process is associated with motion out of the Franck-Condon region and ground state repopulation through internal conversion via a CI of mixed $\pi\pi^*/n\pi^*$ character on a picosecond timescale.

For thymine additional TR-IY measurements are available from Schultz and co-workers. [31 – 34], it should however be noted that these experiments were performed under clustering molecular beam conditions. Time constants of ~0.1 and ~7 ps were extracted through a bi-exponential fit. The fs decay was explained as the ultrafast internal conversion from the initially

excited bright ππ* state to the dark nπ* state which subsequently decays within a few picosecond. A third nanosecond time constant is only observed under certain ionization and molecular beam conditions and attributed to a long-lived state but without further specification.

More recently, uracil was investigated in a collaborative approach by the groups of Weihnacht and Matsika using TR-IY combined with strong field dissociative ionization and calculations. [21, 35] At 260 nm excitation, 70 fs and 2.4 ps decay constants for the parent and 90 fs and 2.6 ps for the dominant fragment (69 amu) were extracted from bi-exponential fits. The signal in both mass channels however differs at long delays, i.e., while the parent trace decays back to zero baseline the fragment signal is observed at times >10 ps. The authors use ionization and fragmentation preferences of the S_1 and S_2 states to distinguish their participation in the relaxation process. Specifically, they conclude that fragmentation of the uracil parent into 69 amu is less likely for ionization from the S_2 minimum compared to the S_1 minimum for the following reasons. Relaxation from the Frank-Condon region to the S_2 minimum results in minimal gain of vibrational energy and is accompanied by an increase in the D_0 ionization potential. Preferential ionization into D_0 from the S_2 minimum combined with low vibrational excitation makes fragmentation less likely. In contrast, during internal conversion and relaxation to the S_1 minimum considerable vibrational energy is gained and ionization correlations switch from D_0 to primarily D_1. Both effects combined place this ionization process easily above the appearance energy of the 69 amu fragment. The authors consequently assign the long lived signal in the 69 amu fragment to ionization of S_1 and the shorter femtosecond and picosecond timeconstants to processes on S_2. Their photophysical model can be summarized as trapping of one portion of the wavepacket near the S_2 minimum (few ps), while another portion moves fast

through the ππ*/nπ* CI. The latter further branches into a rapid decay to the ground state through a ππ*/S_0 CI (< 100 fs) or trapping near S_1 minimum (> 10 ps).

7.2.1.4. Inconsistencies and open questions

Here we present a combination of wavelengths-dependent TR-PES and TR-IY spectra for the purpose of evaluating the contributing steps in the uracil and thymine deactivation process, specifically: (1) Trapping in the S_2 mininum and barrier crossing versus direct paths towards the ππ*/nπ* CI. (2) Ground state repopulation via ππ*/S_0 CI versus deactivation to and trapping on the S_1 nπ* surface. (3) The fate of the S_1 nπ* state population which has been proposed to deactivate to the S_0 (via ππ*/S_0 CI or less likely nπ*/S_0) or triplet states.

The availability of TR-PES and TR-IY spectra in the present study give us unique and complementary capabilities to identify excited state processes. For example, TRPES provides spectroscopic information that, in conjunction with known ionization potentials and correlations, can be used to identify the orbital configuration of the excited states. TR-PES is also unaffected by dissociative ionization processes that form the basis of strong field ionization experiments as discussed above. [21, 31 – 35] As such, the comparison of TR-PES and TR-IY allows us to distinguish fragmentation in the neutral and cationic states and provides further means to correlate fragmentation preferences (mass spectra) and spectroscopic information (photoelectron spectra) at characteristic points during the relaxation process. The long scan time and relative few photons involved in ionization are also advantages of the present study.

7.3 Experimental Setup

The experimental setup used for the present TR-PES and TR-IY measurements include a gaseous molecular beam source, a magnetic bottle photoelectron spectrometer, a linear time-of-flight mass spectrometer, and a femtosecond laser system with UV conversion capabilities that have been described previously. [36 – 40]

Pyrimidine bases uracil and thymine (Sigma Aldrich, ≥98%) were placed in a quartz sample holder located inside a nozzle which is located just before the pinhole and heated to 220°C and 175°C, respectively. A continuous molecular beam of pyrimidine base vapor was carried into the source vacuum chamber by a helium backing gas and doubly skimmed to accommodate differential pumping towards the ultrahigh vacuum chamber, that houses the photoelectron energy analyzer and mass spectrometer. The molecular beam is intersected by a UV fs pump pulse and a time-delayed probe pulse that are spatially overlapped at a small angle and focused by a 50 cm lenses.

Pump pulses centered at 250 nm, 260 nm and 273 nm were generated from a Traveling-wave Optical Parametric Amplifier (TOPAS-C) and kept at 2 μJ / pulse to avoid two-photon excitation. Probe pulses were produced in a second OPA (Coherent OPERA) and set to 295 nm, just below the onset of the absorption spectrum, to avoid unwanted probe-pump signals. This wavelength choice imposes the requirement of a two-photon process for ionization and hence higher probe pulse energies of 12 μJ / pulse were employed. For TR-PES and TR-IY and at all excitation wavelengths, short range scans were recorded between -1 ps < Δt < 6 ps with a 25 fs step size and long range scans were taken between -1 ps < Δt < 600 ps with unequal step size.

Timing calibrations of all TR-PES and TR-IY data are based on 1,3 butadiene measurements which yield a Gaussian cross-correlation function with typically ~200 fs full width at half

maximum (FWHM) and define the position of zero pump-probe delay. TR-PES spectra are energy calibrated with 1,3 butadiene using known ionic state potentials. [41] TOF to mass conversion in TR-IY is performed by analyzing the TOF's of the butadiene mass spectrum. Variant repelling and retarding voltages were applied in the ionization region to collect photoelectrons of certain kinetic energies as outlined in Ref. [38, 39]

7.4 Results and Discussion

TR-PES and TR-IY of uracil and thymine were recorded at 250 nm, 260 nm and 273 nm pump and probed by two photons of the 295 nm pulse, as shown in Fig. 7.2 – 7.4. The pump wavelengths were chosen to populate the S_2 band of $\pi\pi^*$ character with various degree of vibrational excitation in order to assess the accessibility of CIs and energetic onset of competing relaxation pathways.

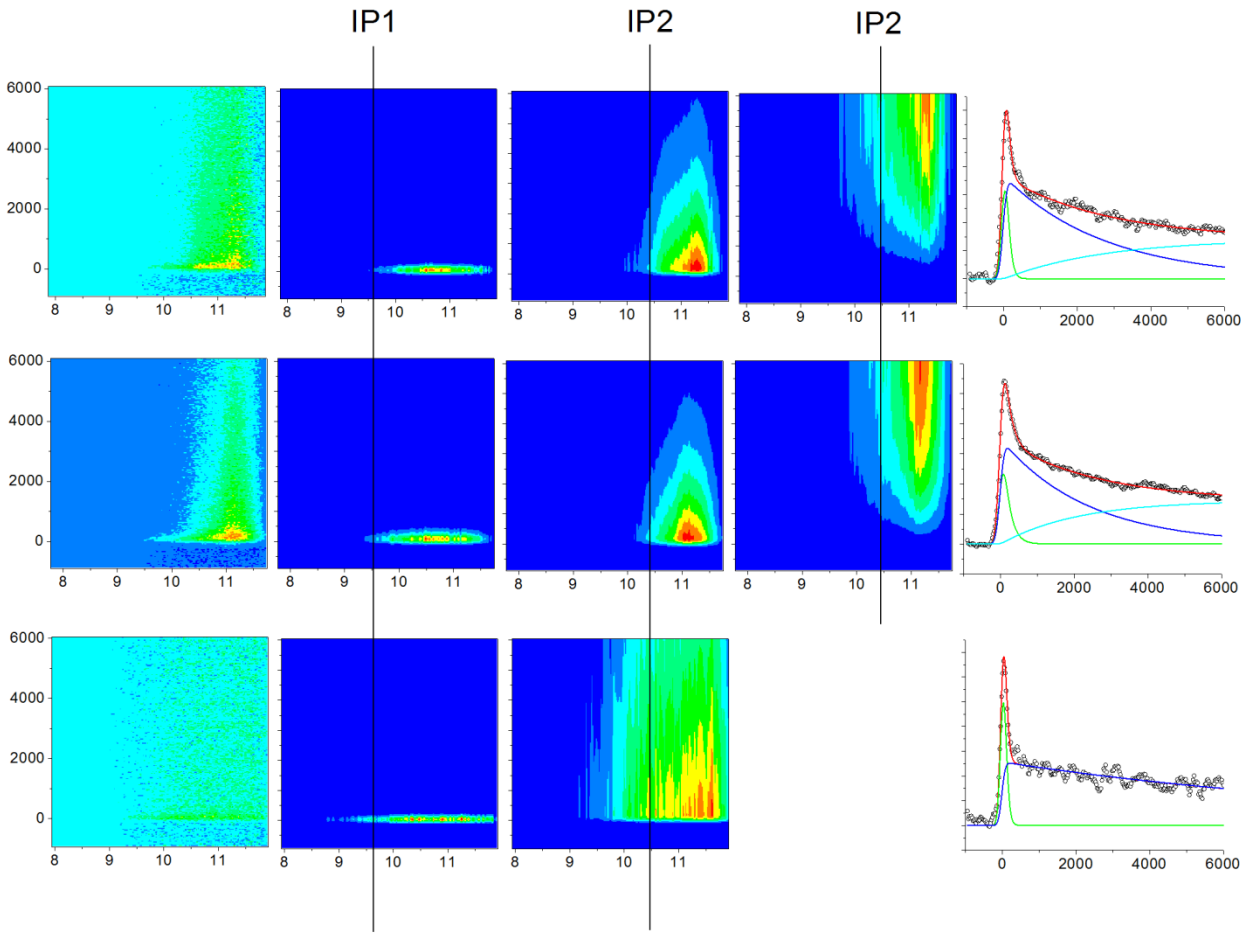

Figure 7.2 TR-PES of uracil recorded at 250, 260 and 273 nm excitation and probed at 295 nm.

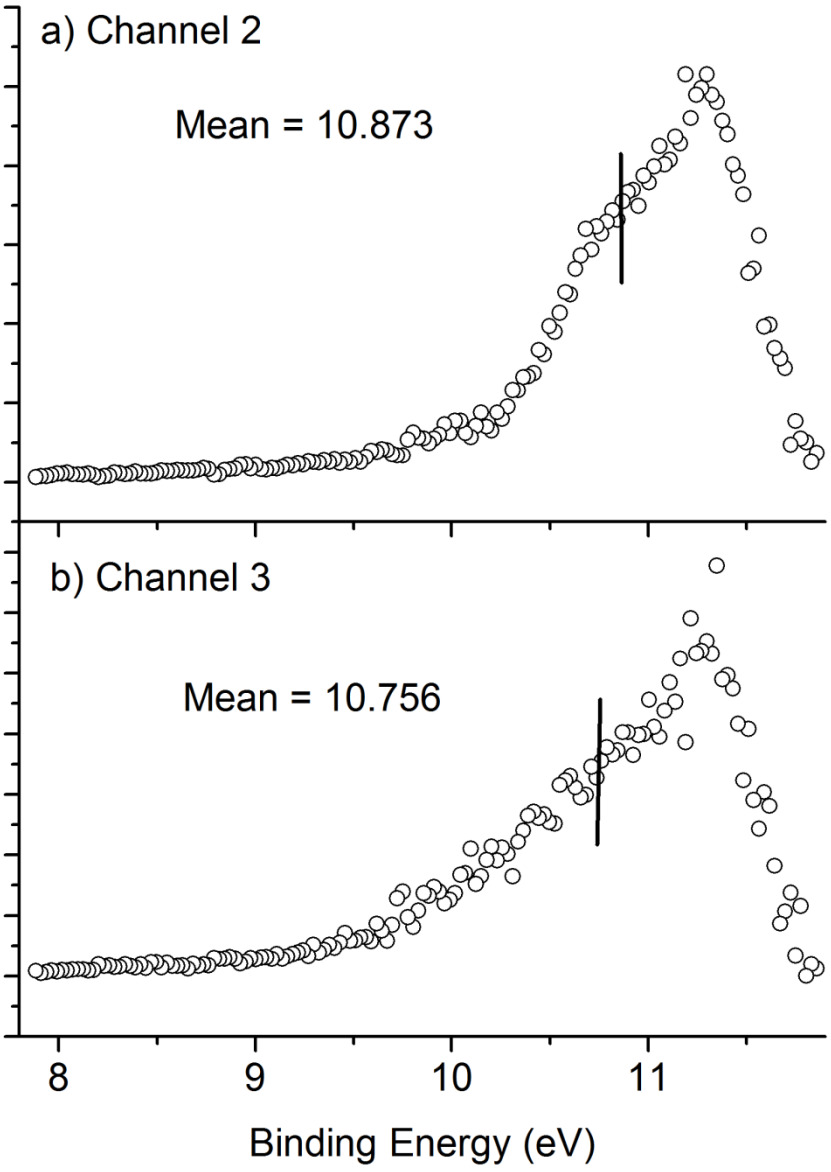

Figure 7.3 Binding energy plots of the ps and ns relaxation channels of uracil from 2D TRPES. Signals were integrated over the entire scan range.

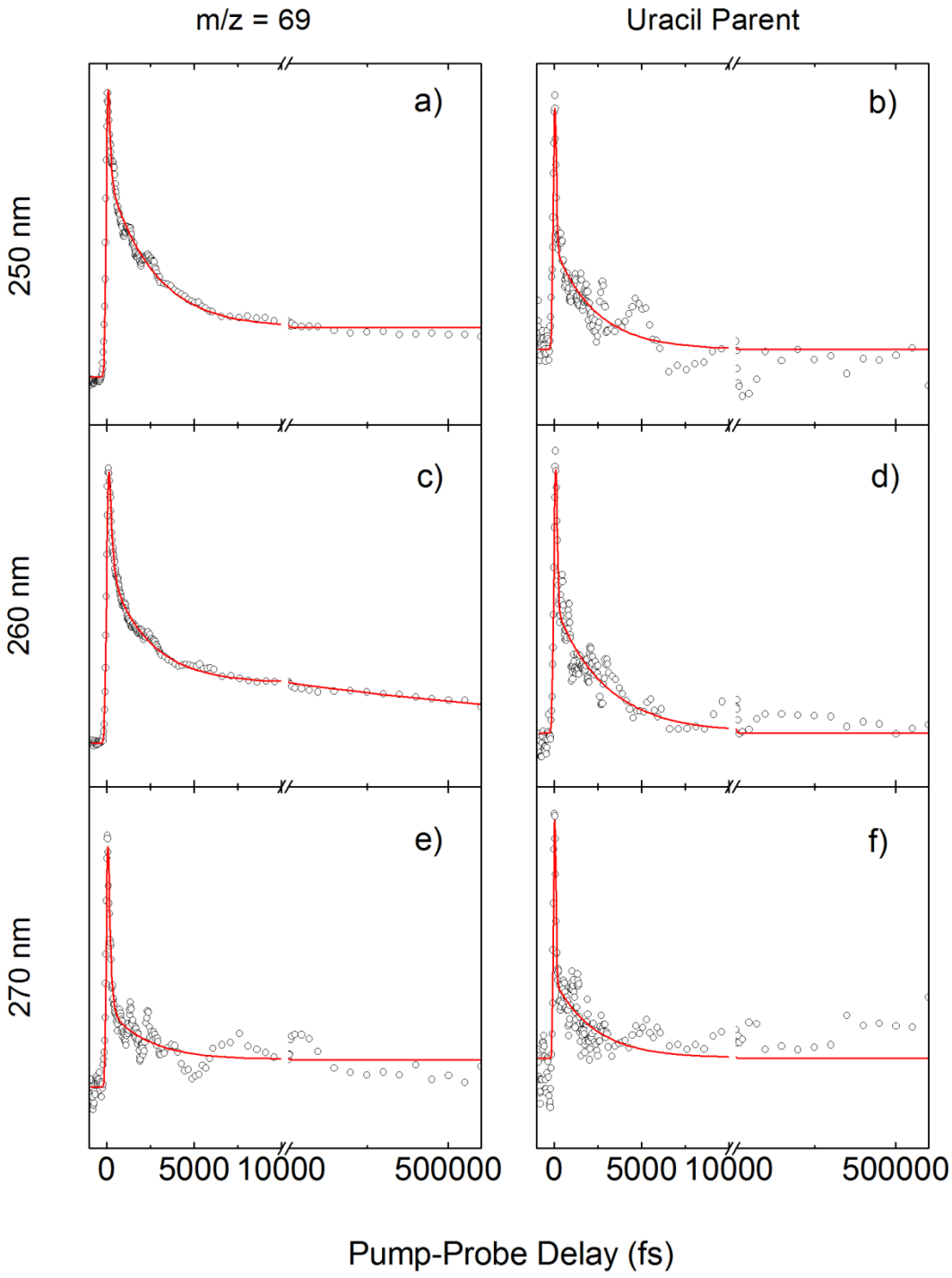

Figure 7.4 TRIY of uracil following excitation at 250, 260 and 273 nm and probed at 295 nm. Transients of the major fragment (m/z = 69) are presented on the left, and parent ion transients are shown on the right.

Fig. 7.2 and Fig 7.6 show the TR-PES spectrum of uracil and thymine, respectively, arranged in the following manner. Column 1 shows the recorded 2d TR-PES signal. Global analysis based on simultaneous fitting of spectra and associated dynamics yields the individual contributions (channels) to the 2d data, which are displayed in Columns 2-4. It should be noted that the spectrum of each channel is assumed to be independent of time, i.e. the signal amplitudes at each specific energy range composing the spectrum follow the same exponential decay. This assumption poses limitations on the data analysis in particular in cases where the cationic ionization potentials vary significantly along the relaxation path. However, full ab initio simulation of the experimental TR-PES spectra is considered beyond the scope of this work. All 2d data is plotted as a function of electron binding energy versus pump-probe delay, with the electron binding energy being readily calculated as the total photon energy minus the measured photoelectron kinetic energy. The corresponding timetraces are shown in Column 5 including the overall signal (integrated Column 1) and individual contributions (integrated Columns 2-4). Fitting functions to extract time constants (see Table 7.1) are based on exponential decays convoluted by the Gaussian instrument response function; the long-lived nanosecond transient is described by an additional rise that equals the intermediate decay.

The photoelectron spectra are analyzed based on ionization correlations between the neutral excited and lowest cationic states and ionization potentials obtained from *ab initio* calculations and high resolution spectroscopy. In addition, conversion of electronic to vibrational energy during the excited state relaxation process is taken into account. For now, we will focus our discussion on uracil due to the recent attention it has received in various experimental and theoretical studies. High resolution resonance enhanced multi-photon ionization spectra of uracil are broad with an onset of 36600 cm^{-1} (4.538 eV) [42]. According to Matsika and co-workers

[21], the excitation energies calculated at the S_0, S_1 and S_2 minimum geometries correspond to: S_1 ($S_{0,\,min}$) = 5.31 eV, S_2 ($S_{0,\,min}$) = 5.75 eV, S_1 ($S_{1,\,min}$) = 4.71 eV, S_2 ($S_{1,\,min}$) = 5.64 eV, S_1 ($S_{2,\,min}$) = 5.00 eV, S_2 ($S_{2,\,min}$) = 5.54 eV. This compares to the values obtained by xxx[Martinez] as follows: S_1 ($S_{0,\,min}$) = 4.83 eV, S_2 ($S_{0,\,min}$) = 5.20 eV, S_1 ($S_{2,\,min}$) = 4.29 eV, S_2 ($S_{2,\,min}$) = 4.56 eV, S_1 (S_2/S_1 CI) = 4.67 eV, S_2 (S_2/S_1 CI) = 4.68 eV, where S_2/S_1 CI corresponds to the geometry at the $\pi\pi^*/n\pi^*$ CI. High-resolution mass analyzed threshold ionization (MATI) locates the adiabatic ionization potential of uracil at 9.3411 eV [43] and conventional He(I) photoelectron spectroscopy places the two lowest vertical ionization potentials at 9.60 (π^{-1}) and 10.13 eV (n^{-1}), [14] which are indicated in the 2d spectra (Fig 7.2, Column 2 – 4) as lines with labels IP1 and IP2. Both techniques employ one-photon excitation and hence transitions originate from the neutral ground state minimum. Ionization potentials calculated by Matsika *et al* [21] are listed here and relevant values are additionally indicated as arrows in Fig. 2 Column 2 – 4 with the following description: IP1 ($S_{0,\,min}$) = 9.41eV, IP1 ($S_{1,\,min}$) = 10.32eV, IP1 ($S_{2,\,min}$) = 10.42eV, and IP2 ($S_{0,\,min}$) = 10.11 eV, IP2 ($S_{1,\,min}$) = 10.48 eV, IP2 ($S_{2,\,min}$) = 10.68 eV. These compare to the values by Martinez and co-workers [10] as estimated from the cationic potential energy curves along the S_2 relaxation path: IP1 ($S_{0,\,min}$) = 9.56 eV, IP1 ($S_{2,\,min}$) = 10.98 eV, IP1 (S_2/S_1 CI) = 10.62 eV, and IP2 ($S_{0,\,min}$) = 10.28 eV, IP2 ($S_{2,\,min}$) = 10.98 eV, IP2 (S_2/S_1 CI) = 11.189 eV. The latter study also provides ionization propensities for these points of interest. Ionization in the Franck-Condon region, from the S_2 minimum and the S_2/S_1 CI occurs dominantly to D_0, as it does for almost the entire relaxation path on S_2. Only during the approach of the S_2 minimum the propensity briefly switches to D_1. This theoretical information provides the bases for the interpretation of our photoelectron spectra, which is somewhat qualitative due to the variation in computed energies with the level of theory. Initial photoexcitation at 250, 260, and 273 nm

populates the S_2 $\pi\pi^*$ state with an estimated excess energy of 0.422, 0.231, 0.004 eV, respectively, assuming an S_2 origin of 4.538 eV [42]. We postpone the discussion of the 273 nm data set which corresponds to excitation close to the origin and requires special consideration. For now our focus is on the 250 and 260 nm spectra. At the Franck Condon region the S_2 $\pi\pi^*$ state preferentially ionizes into IP1. In line with a $\Delta v = 0$ propensity, any vibrational excitation is conserved in the ionization process and the photoelectron signal is expected to shift correspondingly with respect to the IP1. This effect is most clearly observed in our spectra as a ~ 0.2 eV shift towards higher energies as the excitation wavelength is decreased from 260 to 250 nm. It should also be noted that minor contributions from ionization into higher cationic states have been predicted by theory [21] explaining the broad nature of this photoelectron band. Assignment of the photoelectron spectra in Fig. 7.2 Colum 2 at zero pump-probe delay to the S_2 $\pi\pi^*$ ($S_{0,\ min}$) is considered unambiguous as the lower S_1 $n\pi^*$ state is optically inaccessible. During evolution from the Franck-Condon region to the S_2 minimum, S_2 ($S_{0,\ min}$) $\rightarrow$ S_2 ($S_{2,\ min}$), geometry relaxation is accompanied by an increase of IP1 by 1 - 1.4 eV. [10, 21] A similar shift (~0.8 eV) is observed when comparing the onset of the photoelectron spectra in column 2 and 3 and we can therefore associate the ultrafast (< 170 fs) time constants (τ_1) in Table 7.1 Row 1 with this motion. Population of the S_2 $\pi\pi^*$ subsequently decays on an intermediate picosecond timescale (Table 7.1, Row 2, τ_2) and to determine its fate we investigate the photoelectron spectra in Figure 7.2, Column 3 and 4. While adequate description of the slow dynamics necessitates a third, long-lived component in the fit, at first sight no obvious spectral differences are observed. A more quantitative analysis of the spectra is shown in Fig. 7.3 for the example of the 250 nm data set. Photoelectron spectra of the intermediate and long-lived contributions are integrated over all pump-probe delays and their respective weighted mean values are extracted.

For both photoelectron spectra their mean is marked by a vertical, solid line, and it can be noticed that no big energy difference exist between the intermediate component and the long-lived component. Similarly, no significant energy difference is indicated at the 260 nm data set. Most theoretical studies predict internal conversion from the S_2 $\pi\pi^*$ minimum to the S_1 $n\pi^*$ state as the next step in the deactivation process. The switch in electronic state character is accompanied with changes in ionization preferences (i.e. S_2 $\pi\pi^* \rightarrow$ IP1 but S_1 $n\pi^* \rightarrow$ IP2) which in principle should be reflected in the experimental photoelectron spectra. However, according to the calculations by Matsika *et al* [21] mentioned above, the ionization potential IP1 at the S_2 minimum geometry (10.42 eV) is almost identical to IP2 at the S_1 minimum geometry (10.48 eV). As uracil decays to the lower lying S_1 $n\pi^*$ electronic energy is converted into vibrational excitation energy. One would anticipate that photoelectron spectra in column 3 and 4 would shift due to this latter process. However, trapping in the S_1 $n\pi^*$ minimum in the long-lived channel would result in vibrational energy loss, and therefore compensate for the vibrational energy gain from the internal conversion process. Qualitatively, our data reflects the theoretically predicted pathway and we assign the photoelectron signal in channel 3 to ionization from the S_1 $n\pi^*$ minimum. At this point, an alternative pathway based on intersystem crossing recently proposed by Etinski *et al* and Richter *et al* [25, 26] requires consideration. According to their proposal the S_2 $\pi\pi^*$ to S_1 $n\pi^*$ internal conversion occurs on ultrafast timescales and the latter longer-lived (picosecond) state provides access to the T_1 $\pi\pi^*$ state. The T_1 $\pi\pi^*$ minimum is located 2-3 eV below the S_2 $\pi\pi^*$ depending on the level of theory and would acquire this amount of energy as vibrational excitation during the entire relaxation process. Assuming ionization into the lowest IP1 and a corresponding vibrational shift the photoelectron band is likely to fall outside our detection range. Our experiments are therefore insensitive to the T_1 $\pi\pi^*$ and we associate our

signals with pathways involving singlet states only. In summary, following 250 or 260 nm excitation we observed ultrafast relaxation to the S_2 ππ* minimum followed by internal conversion to the S_1 nπ* state on a timescale of a few picoseconds. The latter state is long-lived beyond time frame of our experiments.

We now return our discussion to the 273 nm TR-PES data with significantly different characteristics than the shorter excitation wavelengths. Both, from a spectral and dynamical point of view, the data is well described by a two channel fit, i.e. an ultrafast decay and longer-lived picosecond signal, which are displayed in Columns 2 and 3 next to the TR-PES scan in Column 1. At 273 nm, uracil is excited close to the origin with only minor vibrational excess energy and the short time constant is again associated with motion out of the Franck Condon region. Subsequently uracil decays back to the ground state within 11 ps. Due to the lack of a third nanosecond channel and only minimal shifts between the spectra in column 2 and 3 we conclude that the relaxation proceeds on the ππ* surface towards the ππ*/S_0 CI without state switch to and trapping in the nπ* minimum.

For additional confirmation, TR-IY spectra are analyzed for their dissociative ionization pattern and dynamical evolution of major mass peaks [21]. Time-resolved mass spectra are integrated over the parent peak and the dominant fragment (m/z = 69) to extract their respective time traces in Fig 7.4 (b), (d), (f) and (a), (c), (e). All transients are analyzed with Gaussian convoluted multi-exponential fitting functions. For all excitation wavelengths, the parent time-traces are well described with two exponential decays. Transients of the major fragment however require three exponential decays for 250 and 260 nm excitation, whereas the 273 nm can be fit with a double exponential decay — similar to the TR-PES traces (Fig. 7.2 – 7.4 (b)). All extracted decay constants are listed in Table 7.1.

Our data is analyzed further using the strong field dissociative ionization work [21] as guidance. Photon impact mass spectrometry studies by Jochim and co-workers [4] have reported an appearance energy of 10.95 eV for the onset of cationic dissociation into the m/z = 69 fragment. According to the ionization preferences discussed above photoionization from the S_2 $\pi\pi^*$ state correlates with IP_1 (π^{-1}) with minor contributions from higher ionic states. Ab initio calculations place IP1 in the 10.4-11 eV energy range for the S_2 minimum geometry and depending on the photoexcitation wavelength the molecule gains an additional internal energy of up to 0.4 eV. These crude estimates indicate that cationic fragmentation into m/z= 69 will occur to some extent. In comparison, ionization of the S_1 $n\pi^*$ state correlates with IP_2 (n^{-1}). The ionization energy of IP2 at the S_1 minimum geometry is comparable to IP1 at the S_2 minimum geometry, but during the $S_2 \rightarrow S_1$ internal conversion process uracil acquires an additional ~0.8 eV of vibrational energy. In this latter case, the cationic state is accessed at an overall higher energy and an increased yield in fragmentation can be expected. The nanosecond decay observed in the m/z=69 fragment (but not the parent) at 250 and 260 nm excitation is attributed to the S_1 $n\pi^*$ state due to its higher tendency for dissociative ionization. Since no long-lived component is detected in the 273 nm TR-IY data it is assumed that the S_1 $n\pi^*$ state is not accessed for near-origin photoexcitation. The ultrafast and intermediate time constants are associated with dynamics on the $\pi\pi^*$ surface in analogy with the pathways discussed above for the TR-PES experiments.

In comparison to the existing literature, a sub 100 fs decay constant has consistently been observed in all previous experiments. The ps decay times are in good agreement with reported values of 2.4 ps [28], 2.4 ps [29], 1.9 ps [44], 2.15 ps [35] and 2.4 ps [21], but slightly longer than the 1.05 ps by Canuel *et al* [30]. The ns decay reported here confirms recent measurements

by Matsika and co-workers [21] qualitatively who have also observed an additional long-lived contribution.

7.4.2 Thymine

Thymine dynamics were analyzed based on TRPES and TRIY recorded at 250, 260 and 273 nm pump and 295 nm probe, as shown in Fig. 7.5 – 7.7. The pump wavelengths and the scan ranges were selected the same as uracil for comparison of the two molecules. All thymine time constants extracted from TRPES and TRIY are listed in Table 7.1.

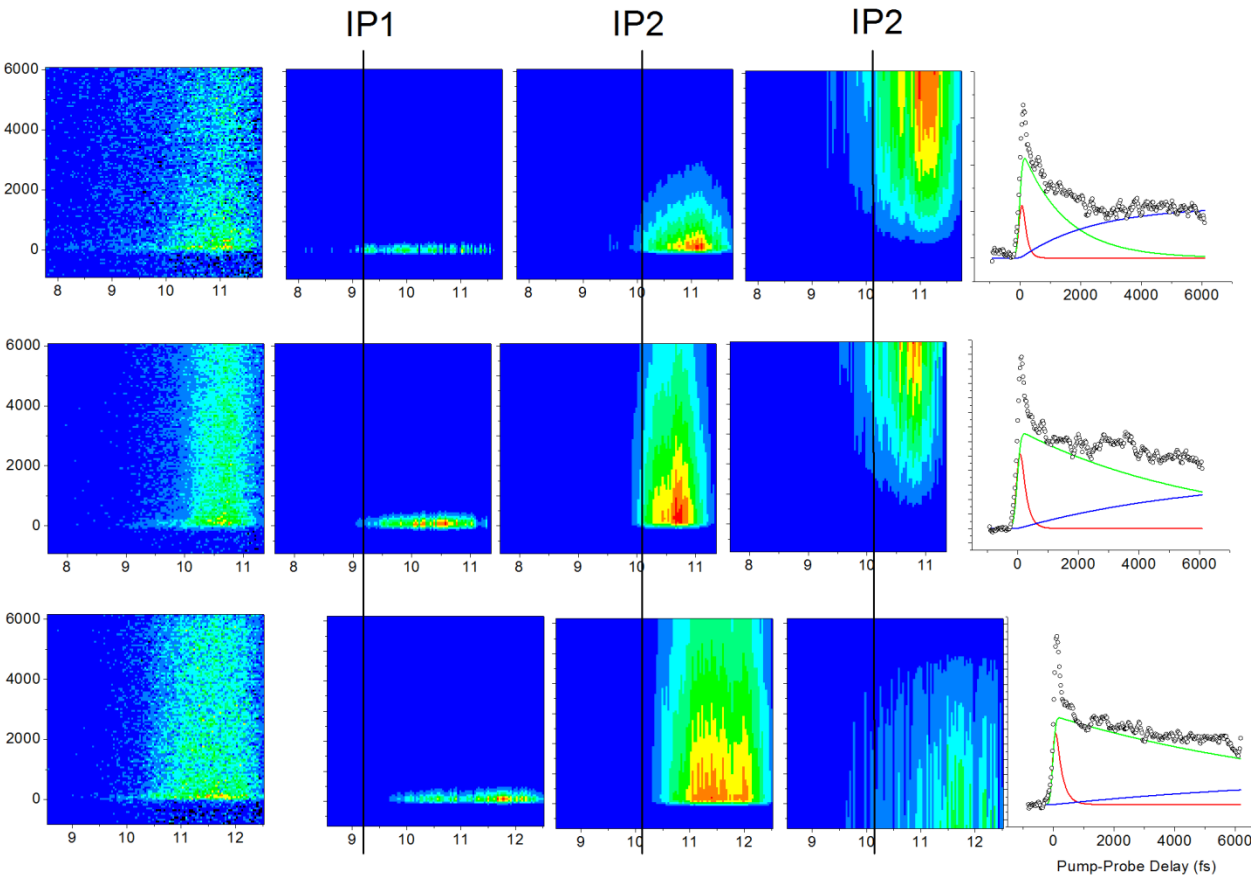

Fig. 7.5 TR-PES of thymine recorded at 250, 260 and 273 nm excitation and probed at 295 nm.

The onset of thymine excitation spectrum is located at 36300 cm^{-1} (4.501 eV) [42]. The excitation energies calculated at the S_0, S_1 and S_2 minimum geometries [10] are very similar to uracil: S_1 ($S_{0,\,min}$) = 4.88 eV, S_2 ($S_{0,\,min}$) = 5.17 eV, S_1 ($S_{2,\,min}$) = 4.24 eV, S_2 ($S_{2,\,min}$) = 4.47 eV, S_1 (S_2/S_1 CI) = 4.68 eV, S_2 (S_2/S_1 CI) = 4.71 eV, where S_2/S_1 CI corresponds to the geometry at the ππ*/nπ* CI. The two lowest vertical ionization potentials are placed at 9.20 (π^{-1}) and 10.05 eV (n^{-1}) by conventional He(I) photoelectron spectroscopy, [14] and are indicated in the 2d spectra (Fig 7.5, column 2 – 4) as lines with labels IP1 and IP2. Ab initio calculations by Martinez and co-workers [10] present potential energy curves of cationic states, and IPs at certain geometries can be estimated: IP1 ($S_{0,\,min}$) = 9.18eV, IP1 ($S_{2,\,min}$) = 10.50 eV, IP1 (S_2/S_1 CI) = 10.25 eV, and IP2 ($S_{0,\,min}$) = 10.53 eV, IP2 ($S_{2,\,min}$) = 10.74 eV, IP2 (S_2/S_1 CI) = 11.0 eV. Ionization correlations of thymine are similar as uracil: [10] Thymine is mainly ionized to D_0 at early times, and ionization propensity switches to D_1 only near S_2 minimum, where the gap between D_0 and D_1 is minimized. After excitation in the Franck-Condon region, S_2 ππ* state is populated. As shown in Fig. 7.5 Column 2, ionization to IP1 occurs after initial excitation. A shift of ~1 eV towards higher BE is observed in the photoelectron spectra (Fig. 7.5 Column 2 – Column 3), which verifies the evolution of IP1 from the Franck-Condon region S_2 ($S_{0,\,min}$) to S_2 ($S_{2,\,min}$), as suggested by Martinez and co-workers [10]. Therefore the fs channel (Table 7.1, τ_1, Row 6) can be attributed to motion out of the Franck-Condon region. After S_2 state depopulation, both a ps channel and a long-lived channel is required to describe the photoelectron spectra. (Fig. 7.5, Column 3 and Column 4) Similar to uracil, no significant energy difference is observed between the two channels. To further investigate the dynamics after S_2 minimum, 1D photoelectron spectra of the two channels integrated over all pump-probe delays are plotted in Fig. 7.6. The weighted averages of the two channels only very by less than 0.1 eV. Although internal

conversion from S_2 $\pi\pi^*$ to S_1 $n\pi^*$ should acquire vibrational excitation energy and make the photoelectron spectra shift towards higher BE, the switch in ionization preferences (S_2 $\pi\pi^* \rightarrow D_0$ but S_1 $n\pi^* \rightarrow D_1$), the difference in IPs [10], and vibrational energy loss in the S_1 minimum trap well compensate for this effect. Thus the dynamics of the photoelectron spectra in Fig. 5, Column 3 and 4 reflect theoretical predicted pathways: Internal conversion from S_2 $\pi\pi^*$ minimum to S_1 $n\pi^*$ state in ps, followed by trapping in S_1 minimum [24, 45] or ISC to triplet states. [25, 26]

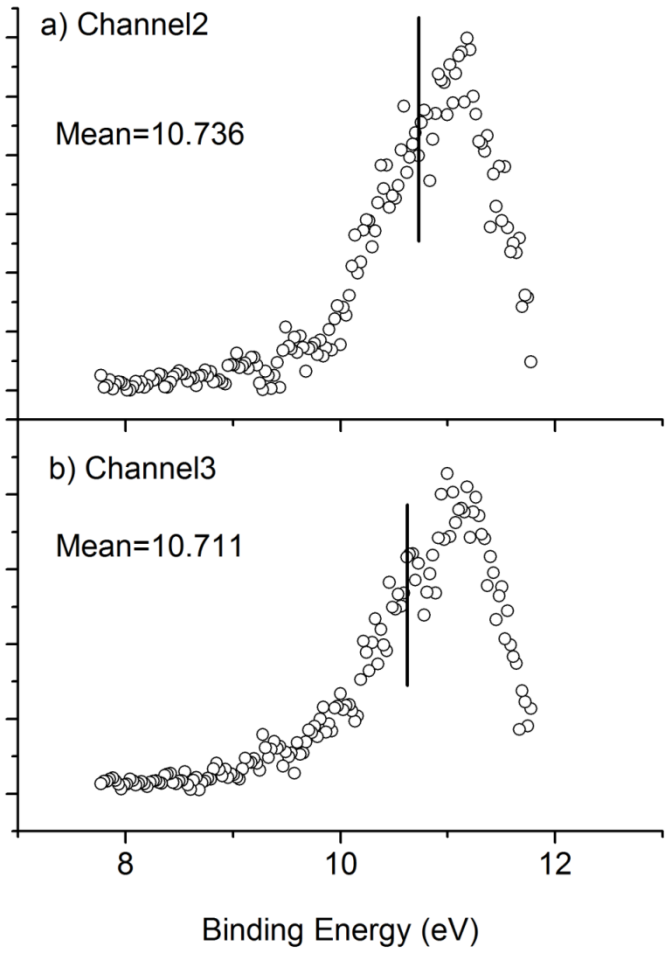

Fig. 7.6 Binding energy plots of the ps and ns relaxation channels of thymine from 2D TRPES. Signals were integrated over the entire scan range.

Thymine dynamics started after different excitation wavelengths are also compared. Assuming 4.501 eV as S_2 origin, [42] excessive energies of 0.458, 0.268 and 0.041 are estimated after photoexcitation at 250, 260 and 273 nm, respectively. From 250 nm to 260 nm spectra, the onset shift towards lower BE slightly, resembling the difference in excessive energies. A noticeable difference in time constants is observed between the two datasets. (Table 7.1) At 250 nm

excitation the photon energy is high enough for thymine to avoid trapping in the S_2 state minimum and quench to S_2/S_1 MECI quickly, which is located at 4.71 eV (~259 nm) [10], while 260 nm and 273 nm excitation are below barrier and dynamics need to start with relaxation to S_2 minimum. From 260 nm to 273 nm data, however, a more significant shift towards higher BE is observed, as a result of higher percentage of molecules are trapped in S_2 minimum and lose vibrational energy. As the 273 nm data obviously need three relaxation channels to describe, and extracted time constants are within the same scale as the 260 nm data, (Table 7.1) the authors conclude that the same relaxation pathways are available for thymine for 260 nm and 273 nm excitation, although trapping in S_2 minimum plays a bigger role at 273 nm excitation.

TR-IY spectra of thymine at all three excitation wavelengths were recorded for further information. (Fig. 7.7) The parent time traces (Figs. 7.7 (b), (d), (f)) are described with two exponential decay channels, and transients of the major fragment m/z = 55 (Figs. 7.7 (a), (c), (e)) are fit with three decay channels, similar to the TRPES traces. Extracted time constants are also included in Table 7.1. The ns decay channel in TRPES is only available in the major fragment m/z = 55 ion yield, which further confirms that this long-lived channel is associated with S_1 $n\pi^*$ dynamics, due to ionization correlations: S_1 $n\pi^* \rightarrow D_1$ and S_2 $\pi\pi^* \rightarrow D_0$ [10] and the fact that 11.7 eV is needed for dissociative ionization to m/z = 55, [4] which requires population of D_1.

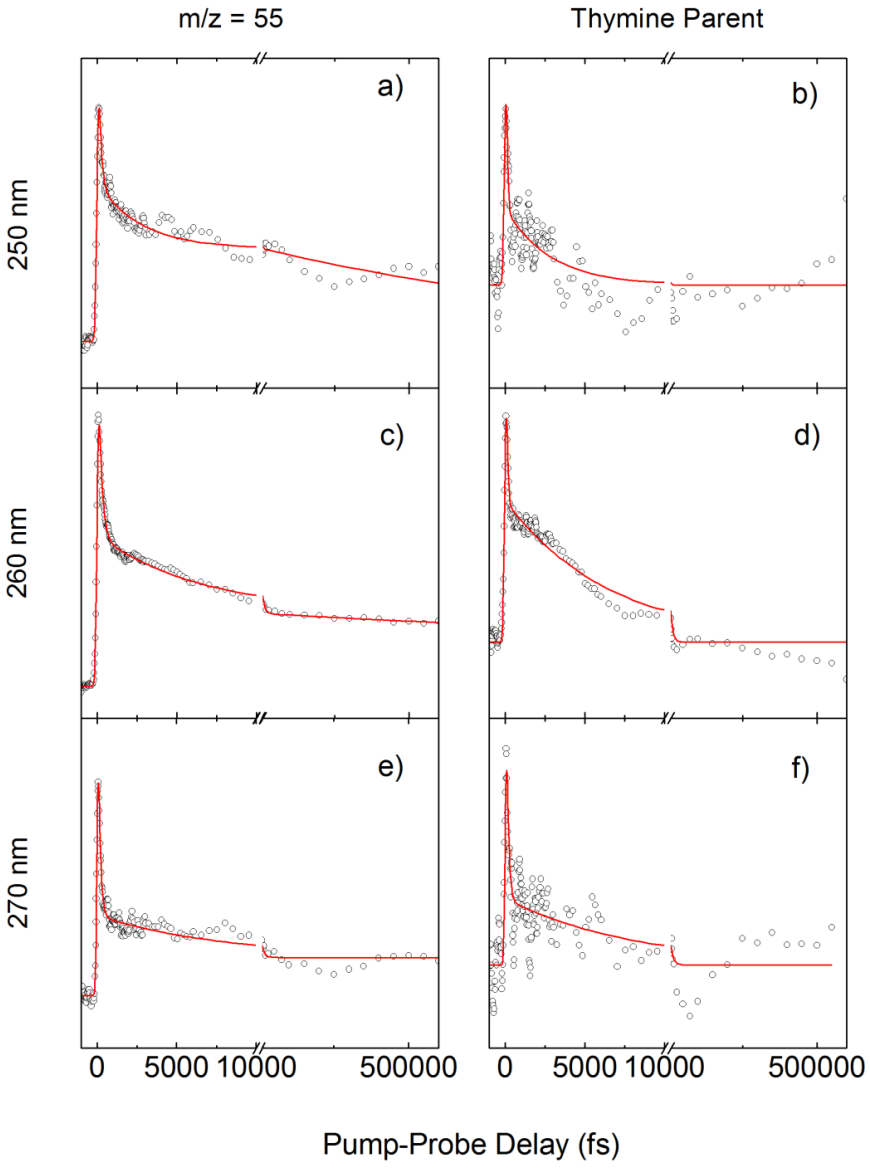

Fig. 7.7 TRIY of thymine following excitation at 250, 260 and 273 nm and probed at 295 nm. Transients of the major fragment (m/z = 55) are presented on the left, and parent ion transients are shown on the right.

Table 7.1 Time constants τ_1, τ_2 and τ_3 of uracil and thymine extracted from TRPES, parent ion yield and the major mass (m/z = 69 in uracil and m/z = 55 in thymine) ion yield at three excitation wavelengths.

	250 nm			260 nm			273 nm		
	TRPES	U^+	69^+	TRPES	U^+	69^+	TRPES	U^+	69^+
τ_1	76 fs	37 fs	97 fs	170 fs	35 fs	150 fs	50 fs	112 fs	133 fs
τ_2	2.58 ps	2.33 ps	2.60 ps	2.35 ps	2.89 ps	2.30 ps	11.1 ps	11.1 ps	10.0 ps
τ_3	>1 ns		>1 ns	>1 ns		>1 ns			
	250 nm			260 nm			273 nm		
	TRPES	T^+	55^+	TRPES	T^+	55^+	TRPES	T^+	55^+
τ_1	125 fs	46 fs	142 fs	175 fs	52 fs	198 fs	202 fs	117 fs	126 fs
τ_2	1.42 ps	2.83 ps	2.72 ps	6.13 ps	6.62 ps	6.70 ps	9.33 ps	8.09 ps	8.09 ps
τ_3	>1 ns		>1 ns	>1 ns		>1 ns			>1 ns

In comparison with existing literature, the <200 fs decay channels are qualitatively identical to all previous experiments. The ps decay channels at 260 nm and 273 nm excitation are in good agreement with the 6.4 ps [28], 5.12 ps [29], 6.5 ps [31], 7 ps [32 – 34], and 6.3 ps [46]. The ns decay also agrees with Schultz and co-workers [31 – 34] and Kim *et al* [46].

7.4.3 Comparison of uracil and thymine dynamics

The substitution of a CH_3 derivative on C_5 in thymine makes several differences to its dynamical properties with uracil. In terms of fs decay channel, τ_1 in uracil is sub 100 fs, much shorter than $\tau 1$ in thymine. This agrees with the AIMS simulation results [10] that the population decrease on S_2 in thymine is less significantly than in uracil in the first 500 fs after initial excitation as a fact of lower lying S_2 minimum in thymine. The binding energy changes linearly with the pump photon energy change in uracil, but almost remains the same at all three excitation wavelengths in thymine.

The τ_2 reported in uracil is not much different among different excitation wavelengths, but significantly gets longer when excitation wavelength is increased from 250 nm to 260 nm in thymine. This explains the calculation result that the estimated barrier height along the pathway connecting the S_2 minimum with the S_2/S_1 minimal energy conical intersection is lower in uracil (0.16 eV) than in thymine (0.28 eV), and that it will take longer for thymine to escape the barrier, when excitation wavelength is longer than 260 nm. [10]

Another significant difference between uracil and thymine is lack of the third channel in uracil at 273 nm excitation. Resembling the simulation result [27], direct pathway of ground state repopulation via $\pi\pi^*/S_0$ CI is open in uracil, while in thymine relaxation through S_2/S_1 CI is the only possible pathway.

7.5 Conclusions

Excited state dynamics of DNA bases that belong to pyrimidine derivatives are investigated with TRPES and TRIY. Pump wavelengths of 250 nm, 260 nm and 270 nm are applied to excite uracil and thymine. After single photon excitation from the UV pump pulse, S_2 state of $\pi\pi^*$

character is populated in both molecules, and three relaxation channels are employed to analyze the excited state dynamics. Corresponding time constants from the tri-exponential decay fits are listed in Table 7.1.

In summary, the fs decay channel is associated with ultrafast motion out of the Franck-Condon region. The initially populated S_2 $\pi\pi^*$ state quickly relax to S_2 minimum at this time scale. The ps decay channel is correlated to internal conversion to S_1 $n\pi^*$ state. A higher barrier along the pathway connecting the S_2 minimum with the S_2/S_1 CI in thymine leads to longer τ_2's at 260 and 273 nm excitation. The $\tau_3 > 1$ ns from the longest decay channel, which is present in TRPES and the major fragments ion yield but is absent in the parents ion yield, reveals S_1 $n\pi^*$ state depopulation. Trapping in S_1 energy minimum is the more likely explanation, but ISC to triplet states cannot be ruled out based on limitations in existing literature and our experimental conditions.

7.6 References

[1] C. E. Crespo-Hernandez, B. Cohen, P. M. Hare, and B. Kohler, *chem. Rev.* 2004, 104, 1997-2019.

[2] C. Z. Bisgaard, H. Satzger, S. Ullrich, and A. Stolow, *ChemPhysChem*, 2009, 10, 101-110.

[3] N. L. Evans, and S. Ullrich, *J. Phys. Chem. A*, 2010, 114, 11225.

[4] H.-W. Jochims, M. Schwell, H. Baumgartel, and S. Leach, *Chem. Phys.*, 2005, 314, 263–282.

[5] L. B. Clark, G. G. Peschel, and I. Tinoco, Jr., *J. Phys. Chem.*, 1965, 69, 3615.

[6] M. Barbatti, A. J. A. Aquino, and H. Lischka, *Phys. Chem. Chem. Phys.*, 2010, 12, 4959-4967.

[7] M. Merchan, R. Gonzalez-Luque, T. Climent, L. Serrano-Andres,E. Rodriguez, M. Reguero, and D. Pelaez, *J. Phys. Chem. B*, 2006, 110, 26471-26476.

[8] V. B. Delchev, A. L. Sobolewski and W. Domcke, *Phys. Chem. Chem. Phys.*, 2010, 12, 5007-5015.

[9] D. Asturiol, B. Lasorne, M. A. Robb, and L. Blancafort, *J. Phys. Chem. A* 2009, 113, 10211.

[10] H. R. Hudock, B. G. Levine, A. L. Thompson, H. Satzger, D. Townsend, N. Gador, S. Ullrich, A. Stolow, and T. J. Martinez, *J. Phys. Chem. A*, 2007, 111, 8500-8508.

[11] N. S. Hush and A. S. Cheung, *Chem. Phys. Lett.*, 1975, 34, 11.

[12] V. M. Orlov, A. N. Smirnov, and Y. M. Varshavsky, *Tetrahedron Lett.*, 1976, 48, 4377.

[13] S. Urano, X. Yang, and P. R. LeBreton, *J. Mol. Struct.*, 1989, 214, 315.

[14] D. Dougherty, K. Wittel, J. Meeks, and S. P. McGlynn, *Am. Chem. Soc.*, 1976, 98, 3815.

[15] G. Lauer, W. Schafer, and A. Schweig, *Tetrahedron Lett.*, 1975, 45, 3939.

[16] B. I. Verkin, L. F. Sukodub, and I. K. Yanson, *Dokl. Akad. Nauk SSSR*, 1976, 228, 1452.

[17] A. Padva, T. J. O'Donnell, and P. R. LeBreton, UV photoelectron studies of biological pyrimidines – electronic-structure of uracil, *Chem. Phys. Lett.*, 1976, 41, 278.

[18] K. W. Choi, J. H. Lee, and S. K. Kim, *Chem. Commun.*, 2006, 78-79.

[19] D. M. Close, *J. Phys. Chem. A*, 2004, 108, 10376.

[20] D. Roca-Sanjuan, M. Rubio, M. Merchan, and L. Serrano-Andres, *J. Chem. Phys.*, 2006, 125, 084302.

[21] S. Matsika, M. Spanner, M. Kotur, and T. C. Weinacht, *J. Phys. Chem. A*, 2013, 117, 12796-12801.

[22] K. Kleinermanns, D. Nachtigallova, and M. S. de Vries, *Int. Rev. Phys. Chem.*, 2013, 32, 308-342.

[23] A. Giussani, J. Segarra-Marti, D. Roca-Sanjuan, and M. Merchan, *Top. Curr. Chem.*, Springer-Verlag Berlin Heidelberg, 2013.

[24] M. Barbatti, A. C. Borin, and S. Ullrich, *Top. Curr. Chem.*, Springer International Publishing Switzerland, 2014.

[25] M. Etinski, T. Fleig, and C. M. Marian, *J. Phys. Chem. A*, 2009, 113, 11809-11816.

[26] M. Richter, S. Mai, P. Marquetand, and L. Gonzalez, *Phys. Chem. Chem. Phys.*, 2014, 16, 24423-24436.

[27] M. Barbatti, A. J. A. Aquino, J. J. Szymczak, D. Nachtigallova, P. Hobza, and H. Lischka, *PNAS*, 2010, 107, 21453-21458.

[28] H. Kang, K. T. Lee, B. Jung, Y. J. Ko, and S. K. Kim, *J. Am. Chem. Soc.*, 2002, 124, 12958-12959.

[29] S. Ullrich, T. Schultz, M. Z. Zgierski, and A. Stolow, *Phys. Chem. Chem. Phys.*, 2004, 6, 2796-2801.

[30] C. Canuel, M. Mons, F. Piuzzi, B. Tardivel, I. Dimicoli, and M. Elhanine, *J. Chem. Phys.*, 2005, 122, 074316.

[31] E. Samoylova, H. Lippert, S. Ullrich, I. V. Hertel, W. Radloff, and T. Schultz, *J. Am. Chem. Soc.*, 2005, 127, 1782-1786.

[32] N. Gador, E. Samoylova, V. R. Smith, A. Stolow, D. M. Rayner, W. Radloff, I. V. Hertel, and T. Schultz, *J. Phys. Chem. A*, 2007, 111, 11743-11749.

[33] E. Samoylova, T. Schultz, I. V. Hertel, and W. Radloff, *Chem. Phys.*, 347, 2008, 376-382.

[34] J. Gonzalez-Vazquez, L. Gonzalez, E. Samoylova, and T. Schultz, *Phys. Chem. Chem. Phys.*, 2009, 11, 3927-3934.

[35] M. Kotur, T. C. Weinacht, C. Zhou, and S. Matsika, following ultrafast radiationless relaxation dynamics with strong field dissociative ionization: a comparison between adenine, uracil, and cytosine, *IEEE journal of selected topis in quantum electronics*, vol. 18, no. 1, jan/feb 2012.

[36] N. L. Evans, and S. Ullrich, *J. Phys. Chem. A*, 2010, 114, 11225.

[37] H. Yu, N. L. Evans, V. G. Stavros, and S. Ullrich, *Phys. Chem. Chem. Phys.*, 2012, 14, 6266.

[38] N. L. Evans, H. Yu, G. M. Roberts, V. G. Stavros, and S. Ullrich, *Phys. Chem. Chem. Phys.*, 2012, 14, 10401.

[39] H. Yu, N. L. Evans, A. S. Chatterley, G. M. Roberts, V. G. Stavros, and S. Ullrich, *J. Phys. Chem. A*, 2014, 118, 9438.

[40] T. J. Godfrey, H. Yu, and S. Ullrich, *J. Chem. Phys.*, 2014, 141, 044314.

[41] J. D. H. Eland, *Int. J. Mass Spectrom. Ion Phys.* 1969, 2, 471-484.

[42] B. B. Brady, L. A. Peteanu, and D. H. Levy, *Chem. Phys. Lett.*, 1988, 147, 538-543.

[43] K-W. Choi, J-H. Lee, and S. K. Kim, *Chem. Commun.*, 2006, 1, 78-79.

[44] P. M. Hare, C. E. Crespo-Hernandez, and B. Kohler, *PNAS*, 104, 435-440.

[45] J. J. Szymczak, M. Barbatti, J. T. S. Hoo, J. A. Adkins, T. L. Windus, D. Nachtigallova, and H. Lischka, *J. Phys. Chem. A*, 2009, 113, 12686-12693.

[46] N. J. Kim, J. Chang, H. M. Kim, H. Kang, T. K. Ahn, J. Heo, and S. K. Kim, *ChemPhysChem.*, 2011, 12, 1935-1939.

CHAPTER 8

CONCLUSION

8.1 Summary of Thesis

The electronic excited state dynamics of five-membered heterocyclic ring molecules – imidazole, pyrazole and pyrrole, have been investigated by time-resolved photoelectron spectroscopy techniques, including TRPES, TRIY and TR-TKER. In a separate but related project, two nucleo bases – uracil and thymine, both of which are six-membered heterocyclic pyrimidine derivatives, are also studied with TRPES and TRIY techniques.

The introduction of this thesis provides a background to the photoexcitation and excited state relaxation processes. Motivation of the works comes from the photo-protection mechanism of biological species under UV radiation. To understand the photostability of the relevant biomolecules, bottom-up approaches are applied, and simple carbon-nitrogen ring molecules are investigated. Non-radiative electronic transitions are discussed, and N-H dissociation and ring deformation are considered major relaxation pathways following UV excitation. The three spectroscopic techniques used in this thesis, TRPES, TRIY and TR-TKER, are also introduced in this chapter.

Chapter 2 presents a brief introduction to the experimental apparatus and user designs, including the femtosecond pulsed laser system which provides the pump and probe laser pulses, and high-vacuum system which provides gaseous molecular beam. TOF of photoelectrons, photoions and

hydrogen atoms to the detectors are recorded, and calibrations of measured spectra are performed by calibration gases.

TRIY and TR-TKER are performed to investigate multiple relaxation pathways of imidazole following 200 nm excitation in Chapter 3. After excitation to $^1\pi\pi^*$ state, $^1\pi\sigma^*$ pathway associated with the N-H stretching coordinate is suggested as the dominant channel due to the strong hydrogen photoproduct signals. Timescales of this channel is extracted at 82-94 fs by measuring the appearance time of hydrogen transients. The ring puckering and C-N stretching pathway, which proceeds along the $\pi\pi^*$ PES, plays a minor role in the pp* depopulation. Corresponding photofragments, including $C_2H_3N^+$, $C_2H_2N^+$, CH_2N^+, and CH_2^+, are observed in the TRIY spectra, and rise times of 107-162 fs are extracted.

The ultrafast relaxation dynamics of imidazole following UV excitation is also studied by TRPES. (Chapter 4) Deactivation through the N-H dissociation CI is the only open channel at 239.6 nm excitation, and is observed on the sub-50 fs timescale. Competing relaxation channels of N-H dissociation and ring-deformation are both available after 200.8 nm excitation. The branching ratio of the two channels are predicted to be 21:4, and relaxation time of the ring-deformation channel is suggested as much longer.

TRIY spectra of pyrazole are recorded after 200 nm excitation to investigate the role of ring deformation relaxation pathways in Chapter 5. Although having received little attention theoretically, pyrazole excited state dynamics is studied for comparison with its structural isomer imidazole. The TRIY results are modeled using $^1\pi\pi^*$ - ring deformation –photofragmentation mechanism, and time constants of < 160 fs are extracted from transients to all photofragments. Comparison with velocity map imaging results indicate that $^1\pi\sigma^*$ state driven N-H dissociation

channel is dominant, re-enforcing the important role of $^1\pi\sigma^*$ state relaxation in biological chromophores and related heterocycles.

Pyrrole, another five-membered carbon-nitrogen heterocyclic ring molecule, is a subunit in biomolecules such as tryptophan, porphyrin, and chlorophyll. Three excitation wavelengths – 240, 217.5 and 200 nm are applied to investigate pyrrole relaxation channels along several potential energy surfaces in Chapter 6. NH-dissociation on the $\pi\sigma^*$ (1^1A_2) state yields high KE H atoms and ground state pyrrolyl photoproducts on timescales of <100 fs. Pyrrolyl in its first excited state is formed *via* the higher lying $\pi\sigma^*$ (2^1B_1) state, which is indicated by the observation of low KE H atoms at 217.5 and 200 nm. Ring deformation pathways, associated with the $\pi\pi^*$ (1^1B_2) state, compete with the NH-stretching mechanism at these shorter wavelengths and yield photofragments of intermediate masses within < 400 fs.

The relaxation dynamics of nucleo bases is also studied in this thesis. Pyrimidine derivatives – uracil and thymine, which have been investigated less extensively than adenine but also play important roles in understanding UV photoprotection, are excited at 250 nm, 260 nm and 273 nm. TRPES are recorded and three relaxation channels are employed to describe the transients, with time scales of fs, ps and ns, respectively, and are associated with corresponding IC or ISC processes. TRIY spectra of these molecules are measured at the same excitation and ionization wavelengths, and time constants of both the parent mass transient and the major fragments are extracted similar to time constants from the TRPES.

8.2 Outlook

The main application of the investigation on imidazole, pyrazole and pyrrole is to help understand photochemical properties of larger nitrogen containing hetero-aromatic biomolecules,

while the study of uracil and thymine provides an addition to the earlier studies of DNA base adenine, and extends the understanding of the role of UV photoresistance and photostability in evolution of nature. The possibility of laser treatment of diseases is also brought up by the presented ultrafast photo-relaxation properties of the heterocyclic molecules.